Universidad de Chile
Facultad de Ciencias Físicas y Matemáticas
Departamento de Astronomía

The structure of MgII absorption systems from spectra of gravitationally lensed quasars

by

María José Maureira Pinochet

Thesis submitted in partial fulfillment of the requirements
for the degree of Master in Astronomy at the Faculty of Physical and Mathematical Sciences, Universidad de Chile

Advisor Professor	:	Sebastián López
Examiner Comitee	:	Andrés Escala
		Paulina Lira
		Alain Smette

August, 2011.
Santiago - Chile.

Acknowledgements

I acknowledge the financial support from the Chilean Government, trough CONICYT (Comisión Nacional de Investigación Científica y Tecnológica), by means of the scholarship Beca de Magíster.

I would like to specially thanks Dr. Sebastián López, for his insightful opinions and suggestions. Also for the unconditional support during my career and for teaching me the tools needed for this work.

I thank Dr. Sara Ellison and Dr. Alain Smette for providing me with very useful comments on my thesis.

I would like to thank to all my friends at Cerro Calan: Elise, Isma, Simon, Vicho, Melina, Yanett, Andrés, Celia and Shoyer for the moments shared and the support on all kind of moments lived during these years. I would like to specially thanks to Andrés Guzmán, for all the inspirational discussions at the end yet the hardest moments of my thesis. Thanks to the people at Cerro Calan for the warm atmosphere provided. Thanks to all the professors, specially to Paulina Lira for all her advices. I am very happy and proud I chose to be a student there.

I would like to thank my family and friends for the unconditional support and understanding shown through all these years. Thanks to my mom, dad, sisters, brothers and beautiful niece. Finally thanks to my very dear friend Angeles, for all the revitalizing speeches and help.

Contents

Abstract

In this thesis I present a search for MgII absorption systems in the resolved spectra of 10 high redshifts gravitationally lensed quasars. The goal of the thesis is to study the spatial structure of MgII systems. The quasars were observed at resolutions $R \sim 4\,500$ and $R \sim 40\,000$. The search yielded a sample of 31 MgII absorption systems at $0.4 < z < 1.6$ and probing transverse separations between lines of sight (LOS) in the range 0.29-23 h_{70}^{-1} kpc. Adding systems from the literature increased the number of systems to 95. The range of transverse separation of the full sample is 0.3-100 h_{70}^{-1} kpc.

In this sample, the dispersion in the fractional equivalent width differences, ΔW_r, decreases with equivalent width for strong systems while no high ΔW_r values are found for transverse distances $d < 9\ h_{70}^{-1}$ kpc. This is in agreement with a smooth distribution of gas at these scales. In addition, these systems show a trend of increasing ΔW_r with transverse separation. For weak systems, the dispersion in ΔW_r with respect to W_r is greater than for strong systems. In this case anticoincidences (i.e., absorption in just one LOS) are found homogeneously in the range $0.2-30\ h_{70}^{-1}$ kpc. For coincidences, ΔW_r increases with transverse separation but after $3-4\ h_{70}^{-1}$ kpc the trend reverses. These results indicate that weak systems are more patchy or smaller than strong ones.

To estimate transverse sizes, I have used two likelihood methods. The first one considers the absorption systems as spheres or disks with a uniform distribution of gas. This method yields $R \sim 10$ and $14\ h_{70}^{-1}$ kpc for weak and strong systems, respectively. The second likelihood method uses the individual equivalent widths and assumes the equivalent width varies with impact parameter, i.e. $W_r = W_r(r)$. For $W_r(r)$, I tested a power law and a logarithmic function. The logarithmic function seems to be in better agreement with the data for both strong and weak systems. The second method yields $R \sim 20$ and 40 h_{70}^{-1} kpc for weak and strong systems, respectively. Thus, both methods yield smaller sizes for weak population. These sizes are much smaller than estimates using just the frequency of systems, $\frac{dN}{dz}$. Combining the results of models and observations suggests that size estimation of strong MgII systems is consistent with the assumed distribution of gas, while for weak systems the resulted sizes from the likelihood analysis seem to be overestimated. In conclusion, weak systems are predicted to be smaller ($3-4\ h_{70}^{-1}$ kpc) and more patchy than strong systems.

Finally, the sample of systems associated with the lens galaxies shows that W_r for strong systems decreases with increasing impact parameter. On the other hand, weak systems does not show a clear trend with impact parameter.

These systems, produced in lens galaxies, probe smaller impact parameters than blind follow-ups of absorbing galaxies (Chen et al. 2010).

Chapter 1

Introduction

Thesis goal

Study the spatial structure of metal enriched gas using resolved spectra of gravitationally lensed quasars. The lines of sight are separated by kpc scales and probe intervening gas at high redshift.

1.1 Quasar Absorption Lines

The Quasar Absorption Line technique uses the light of distant background quasars to study in absorption the gas bound to galactic structures or to the intergalactic medium, at different redshifts.

The technique provides a sensitive measure of the gas that is independent of the redshift and brightness of both the background QSO and the absorbing galaxy. Due to the dominant abundance of hydrogen in the universe, this atom produces the majority of absorption lines seen in QSO spectra, but also several heavier elements have been observed in absorption in different ionization states such as: C, Mg, Fe, Ca, N, Si, O, etc. (Figure 1.1). Many properties of these systems such as number density per unit redshift, equivalent width distribution, chemical abundances, velocity spreads, etc. can be inferred from the spectra. These measurements give us clues about the formation and evolution of galaxies across $\sim 95\%$ of the Hubble time.

According to their HI column density systems are classified as: Damped Lyα or DLAs (with $\log N(HI) \geq 10^{20.3}$ cm^{-2}), Sub DLAs (with 10^{19} cm$^{-2} < \log N(HI) < 10^{20.3}$ cm^{-2}), Lyman Limit Systems or LLS (with $10^{17.2}$ cm$^{-2} < \log N(HI) < 10^{19}$ cm^{-2}) and Lyman-α forest systems with $\log N(HI) < 10^{15}$ cm^{-2} (Figure 1.2).

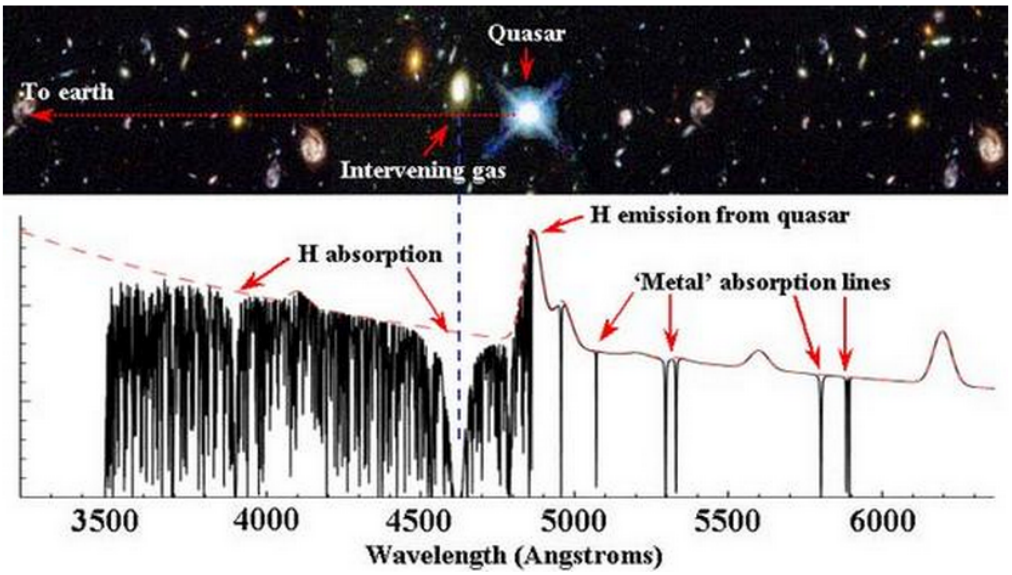

Figure 1.1: The light from distant quasars passes through intervening gas of galaxies or the IGM. Different atoms (HI and metals) absorb light. The observed absorption wavelength depends on the absorption redshift and the transition rest wavelength. Figure by Michael Murphy

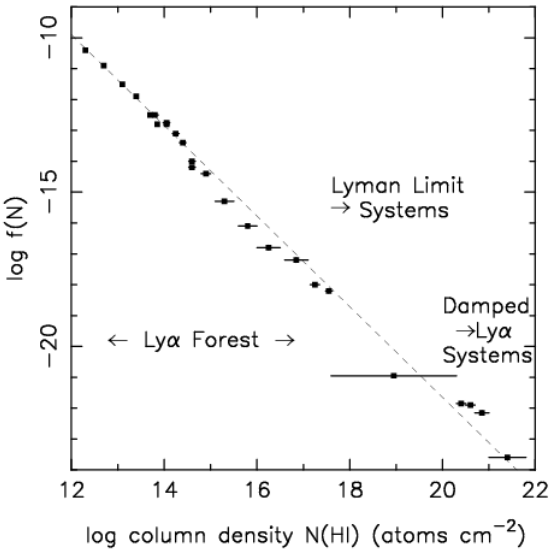

Figure 1.2: Column density distribution of neutral hydrogen for the Lyα forest, Lyman limit systems and Damped Lyα systems. The distribution is fitted by a power law $f(N) \propto N^{-1.46}$. Figure from Storrie-Lombardi & Wolfe (2000).

The highest HI column densities (DLAs, Sub DLAs and LLSs) are believed to be related to galactic environments, which explains the metal absorption systems observed at the same redshift. On the other hand, Lyα forest absorption systems trace the more diffuse intergalactic medium (IGM) structures such as filaments, and so no metals are expected at the redshift of these absorptions. (Although, some metals such as CIV and SiIV have been detected in high-column density Lyα forest systems; Songaila & Cowie (1996)).

This thesis deals with the MgII absorption systems in the line of sight to lensed quasars.

1.2 MgII absorption systems

The MgII doublet ($\lambda 2796, 2803$ Å) is a very good tracer of galaxies for the following reasons:

- It can be observed in optical spectra in the redshift range $0.2 \lesssim z \lesssim 2.2$.
- It is easy to detect due to the doublet ratio (2:1) and the large separation of 7 Å.
- When strong MgII is present, often other ions are also detected (FeII, MnII, etc).
- It arises in structures having a wide range of H I column densities, including sub-Lyman limit systems (Churchill et al. 1999), Lyman limit systems (Steidel & Sargent 1992), and damped Lyman-alpha systems (Rao & Turnshek 1998). The range of galaxies selected by MgII absorption is wide, from very blue colors (spirals/irregulars) to colors typical of elliptical galaxies. The average galaxy absorber has a color of a Sb spiral (Steidel 1995).

Figure 1.3 shows an example of a MgII absorption system.

1.2.1 Equivalent Width definition

The equivalent width of an spectral line is defined as

$$W = \int \frac{F_c - F_\lambda}{F_c}$$

where F_c is the value of the continuum of the source and F_λ is the flux measured in the spectrum. According with this definition, the equivalent width corresponds to the area of an spectral line in a normalized spectrum. Also, it can be understood as the width of a box reaching up to the normalized flux that has the same area as the spectral line (Figure 1.4). The equivalent width is independent of the spectral resolution.

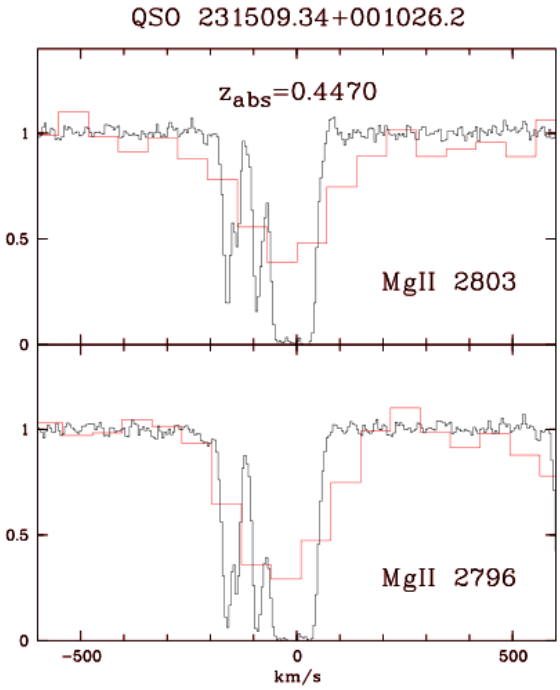

Figure 1.3: MgII absorption system in velocity space. I show the same absorption system at low $R \sim 2\,000$ (red) and high $R \sim 40\,000$ (black) resolution for comparison. $W_r = 1.5$ Å. Figure by Sebastián Lopez.

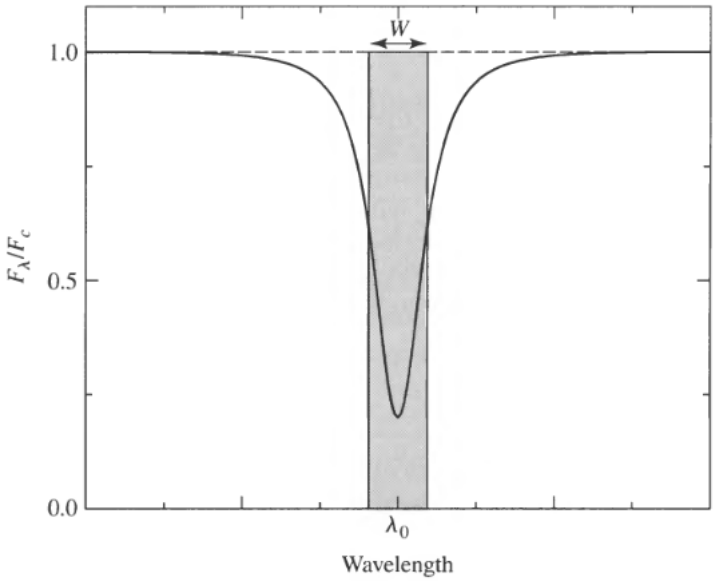

Figure 1.4: Equivalent width of an absorption line. Taken from Introduction to Modern Astrophysics (Carroll & Ostlie).

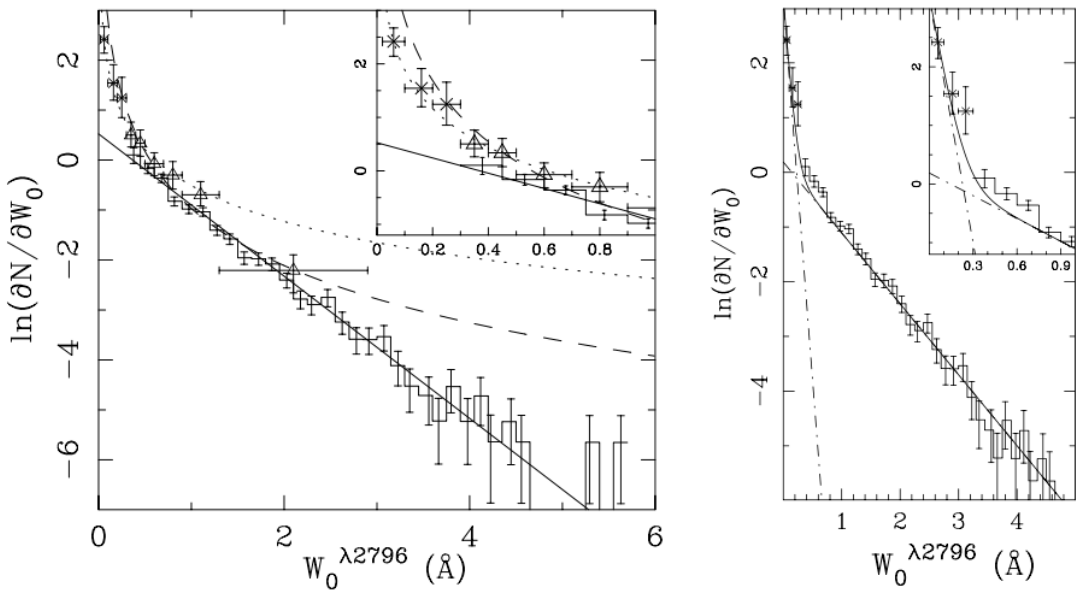

Figure 1.5: Equivalent with distribution of MgII systems (number of systems per unit W_r per unit redshift). Two population of absorbers can be distinguished: Weak and Strong systems, having a transition at ∼0.3 Å. To the left the solid line is the exponential fit to the strong population by Nestor et al. (2005), the dotted and dashed line are power law fits by Churchill et al. (1999) and Steidel & Sargent (1992) respectively. To the right the solid line represent the sum of the two exponential found for the weak and strong population by Nestor et al. (2005). Figure from Nestor et al. (2005).

1.2.2 Equivalent Width distribution

From the rest frame equivalent width ($W_r = W_{obs}/(1+z)$) distribution of MgII systems two populations can be distinguished: weak and strong systems (Nestor et al. 2005). The weak systems are defined to have $W_r(2796) < 0.3$ Å and strong systems present $W_r > 0.3$ Å. According to Nestor et al. (2005), Figure 1.5, both populations can be fitted by an exponential function of the form

$$n(W) \equiv d^2N/dWdz = (N^*/W^*)e^{-(W/W^*)}$$

with different values for W^* and N^* for each population. However, Churchill et al. (1999) and more recently Narayanan et al. (2007) found that the weak population is well fitted by a power law $n(W) = W^{-1.04}$. They also found that for strong systems the rest equivalent width distribution steepens with decreasing redshift between $z = 1.6$ and $z = 0.7$. Narayanan et al. (2007) studied the weak population and found that there is an evolution in the sense that at higher redshift ($1.4 < z < 2.4$) the Wr distribution is close to the exponential function fitted to the strong systems.

1.2.3 Incidence of systems

Integrating in W, $n(W)$ gives the number of MgII absorption systems per unit redshift, dN/dz. Nestor et al. (2005) found $dN/dz \sim 0.8$ for strong systems, and Narayanan et al. (2007) found $dN/dz \sim 1.6$ for weak systems, both at $< z > \sim 1$. For lines with $0.3 < W_r < 2$ there is no significant evolution in dN/dz, but for lines with $W_r > 2$ Å there seems to be an evolution given by a decrease in the number density with decreasing redshift,from $z = 1.6$ to $z = 0.7$. Narayanan et al. (2007) detected evolution for weak systems given by a decrease at high redshift ($z > 1.5$) with a peak at $z = 1.2$. So, taken at face value, the evolution of weak and very strong population systems seems to show opposite trends.

1.2.4 Kinematics

Regarding kinematics, there is a wide range of characteristics that probably represent different structures in the galaxy environment (disk/halo) dominated by a certain kind of gas transport (rotation, infall, outflows). Also, given the large range in velocity of some systems it is likely that they occur in galaxy groups or galaxy/satellite pairs.

Figure 1.3 illustrates that strong systems are often dominated by one (in rare cases by two) strong component, accompanied by weaker lines that spread over a larger Δv of a few hundreds of km/s (Churchill & Vogt 2001). These kinematics are consistent with a model that takes into account a disk in rotation and an infalling halo together (Charlton & Churchill 1998, Churchill & Vogt 2001). However several authors have argued that MgII might also probe galactic-scale outflows (Nestor et al. 2011, Bouché et al. 2007, Rauch et al. 2002).

The profiles of weak systems are mostly composed by one or two clouds (Narayanan et al. 2008). These clouds select optically thin neutral hydrogen, unlike strongest systems (Churchill et al. 1999). Those weak systems composed by a single cloud should trace a large fraction of the $\log N(HI) \sim 16$ cm^{-2} Lyα forest (Rigby et al. 2002). Also, in several cases no $L > 0.05$ L* galaxy is found within $\sim 50\ h^-1$ kpc, as in the case of strong systems (Steidel 1995).

1.3 Sizes

The goal of this thesis work is to constrain MgII sizes. In general, sizes are difficult to estimate using QSO spectra. There are three ways to estimate transverse sizes:

-Based on the incidence of systems.
-Based on the identification of absorbing galaxy.
-Using lensed QSOs.

Early stimates of the size of MgII systems based on the number of absorbers per unit redshift and on the galaxy luminosity function gave sizes in the range $46 - 70\ h_{70}^{-1}$ kpc (Tytler et al. 1987, Lanzetta et al. 1987). This method assumes that $dN/dz = \sigma n$, where σ is the absorber cross section and n the absorbing galaxy density. Further estimates that additionally used information on the impact parameters to identified galaxies gave dimensions of $\sim 27\ h_{70}^{-1}$ kpc (Steidel 1995). All these estimations are for strong systems. Churchill et al. (1999) calculated for weak systems a size of $\sim 46\ h_{70}^{-1}$ kpc assuming that the density of galaxies in which these systems are produced is the same as for strong systems.

1.3.1 Transverse sizes using lensed QSOs

Galaxy identification is expensive in terms of telescope time because it requires deep spectroscopic surveys. A more direct method to estimate sizes is to use gravitationally lensed quasars. These are very well suited for this purpose because their lines of sight probe gas regions on transverse scales of a few kpc (Figure 1.6).

First attempts to study absorption systems in lensed quasars were made by Smette et al. (1992, 1995). Subsequently, lensed QSOs have been used to probe transverse structure of DLA, Lyα forest and metal systems (Dinshaw et al. 1997, Lopez et al. 2005, 2007, Ellison et al. 2004).

Smette et al. (1995) reports lower limit of $22\ h_{50}^{-1}$ kpc for MgII systems with $W_r > 0.3$ Å. More recently, Ellison et al. (2004), using a tripled imaged QSO, give a most probable coherence scale of $2\ h_{70}^{-1}$ kpc for weak systems, and a minimum radius of $\sim 3\ h_{70}^{-1}$ kpc for strong systems. The sample probed transverse dimensions of $30\ h_{70}^{-1}$ pc to $2.7\ h_{70}^{-1}$ kpc. Rauch et al. (2002) studied 3 MgII systems at high resolution in a quadruple lensed quasar with a range of traverse distance from about 200 to 600 h_{50}^{-1} pc. Those authors found that it is difficult to trace individual clouds over distances larger than 200-300 h_{50}^{-1}pc.

Most of these studies have used a handful of lensed QSOs. New studies with larger samples are needed to constrain absorber sizes in a statistical way. This is the motivation for this thesis.

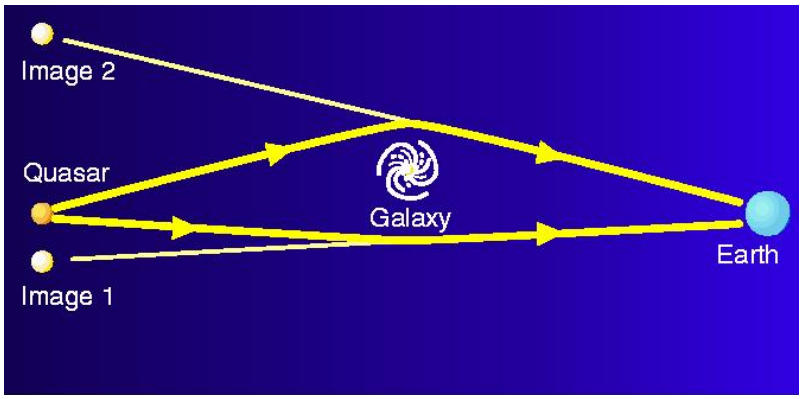

Figure 1.6: Schematic view of two lensed images of a quasar and the different paths of the lines of sight.

1.4 Outline of this work

In this thesis I have used a sample of high-quality spectra of 10 double quasars. The observations were done at the Magellan and VLT telescopes. The spectral resolution ranges from $R \sim 4500$ to $R \sim 40000$. The angular separations of the images are in the range $0.85 < \theta'' < 3.20$. These separations will allow me to compare the absorption systems on transverse scales up to $<\sim 30\ h_{70}^{-1}$ kpc. I have included 7 lensed quasars from the literature, some of them recently published in a MSc thesis (Rogerson 2011). These new lensed quasars expand the range of transverse distances up to $\sim 100\ h_{70}^{-1}$ kpc.

The goal of my thesis is to use the spectra of these gravitationally lensed quasars to probe the transverse structure of the MgII absorption systems in a statistical fashion. To this aim, I will search for MgII $\lambda 2796, 2803$ in every line of sight independently. I will calculate rest frame equivalent widths (W_r) and the transverse separation of the lines of sight at the redshift of the absorptions. Then, I will examine the differences in W_r as a function of W_r and separation.

I will use two methods for the size estimations. One of them consists of a maximum likelihood analysis (McGill 1990, Dinshaw et al. 1997) based on the probability of getting the observed number of coincidences[1] and anti-coincidences[2], given a halo geometry. The other approach also involves a maximum likelihood analysis but it additionally includes the information about W_r differences between lines of sight (Dinshaw et al. 1997). In this latter case, I will assume a certain type of W_r profile as a function of impact paremeter, and find the parameters governing the variations over W_r and distance to the galaxy. Absorbers size is one of these parameters.

[1] An absorption detected in both lines of sight at the same redshift.
[2] An absorption detected in just one of the lines of sight.

Finally, the sample of systems associated with the lensing galaxies is interesting in its own. In the case of the lens galaxy, the impact parameter to the galaxy can be obtained from the literature. Therefore, in those cases gas density variations as a function of impact parameter can be studied and compared with other surveys.

Chapter 2

Data acquisition

The sample is composed of resolved spectra of 10 lensed quasars. Seven of them were observed at medium resolution with the MagE/Magellan spectrograph and 3 at high resolution with the UVES/VLT spectrograph. I participated in the MagE observations at the Magellan telescopes at Las Campanas Observatory. These observations were made in two runs of two nights each in August 2009 and March 2010. On the other hand, details of the UVES observations can be found in Lopez et al. (2005) and Lopez et al. (2007).

In the following I describe the data and its acquisition.

2.1 The spectrographs

The MagE (Magellan Echellette) Spectrograph is a moderate-resolution optical echellette mounted on the Clay 6.5m Magellan telescope in Las Campanas, Chile. The UVES (UV-Visual Echelle Spectrograph) is a two-arm cross-dispersed echelle spectrograph mounted on the second Unit Telescope (Kueyen) of the VLT in Cerro Paranal, Chile.

Echelle spectrographs are designed to obtain high dispersion in a large range of wavelengths. A grating is used to obtain a high dispersion. A second disperser element called cross-disperser is utilized to spatially separate the orders obtained from the grating dispersion. The cross disperser can be another grating of lower dispersion or a prism.

An order represents a usual spectrum, each one with different and consecutive wavelength ranges. For a given order, the difractted angle at which each wavelength falls onto the detector varies with wavelength. The final result is that orders are bent. Figure 3.1 shows the spectra of a standard star in which the curvature can be observed for the case of MagE spectrograph.

The wavelength coverage of MagE is approximately 3100 Å to 1 micron and it has a resolution of $R \sim 4100$ for a slit width of $1''$. All slits are $10''$ long with a plate scale[1] of $0.3''/pixel$. We utilized the fast read-out mode. The values for the gain and read-out-noise in this mode are 0.82 e^-/DN and 2.9 e^- respectively. The binned pixel sample[2] (or dispersion) is about 0.4 Å at 5000 Å.

The MagE optical design incorporates a reflective collimator, a medium[3] order ($6 < n < 20$) reflective diffracting grating in combination with two prisms to provide cross dispertion. The collimated light from the slit is pre-cross-dispersed by the first prism before it reaches the echellette grating. The grating-dispersed light is once again cross-dispersed by a second pass through the first prism and then passes through the second prism before being imaged onto the detector by the camera (Marshall et al. 2008). This design, in which the grating acts as a postdisperser (after the first cross-disperser prism) introduces a wavelength dependent spectral line tilt (Chaffee & Schroeder 1976). Figure 3.5a shows the MagE spectrum of a Th-Ar lamp in which can be observed the tilt.

For UVES the wavelength coverage is 3000 - 5000 Å (Blue arm) and 4200 - 11000 Å (Red arm). The spectral resolution for a $1''$ slit is about 40 000. The pixel scales are $0.22''/pixel$ and $0.16''/pixel$ for the blue and red respectively. The pixel sample is about 0.04 Å at 5000 Å.

For both arms, the light beams that enter the spectrograph are reflected by a mirror to the main collimators, then they are dispersed by the echelle gratings. After that, the dispersed beams fall on the cross-disperser units each one composed by two gratings. The blue gratings scatter the light into 33 and 35 orders, while in the red the gratings produce 37 and 33 orders ($n > 60$). From here the echelle spectra enter the cameras and are recorded on the CCD detectors. In this configuration the tilt is the same for every wavelength and it is corrected by a rotation of the slit by 7 degrees (Dekker et al. 2000).

Also, UVES has an Atmospheric Dispersion Correction (ADC) unit. This unit can be inserted in the pre-slit area to correct for atmospheric dispersion.

Both spectrographs are very efficient in the blue, which is important for my work since I am searching for the MgII $\lambda 2796, 2803$ doublet that fall in the blue for redshifts $1 \gtrsim z \gtrsim 0.1$.

[1] Size of a pixel as projected on the sky.

[2] Size of a pixel in wavelength units.

[3] n is the order number from the echelle equation: $\frac{n\lambda}{d} = \sin\alpha + \sin\beta$, where d is the center to center facet separation, α and β are the incidence and difractted angle with respect to the grating normal respectively.

Table 2.1: Main observational properties of the MagE sample.

QSO	RA	DEC	Run[a]	Image	Exptime [s]	Magnitude	S/N[b]
Q1017-207	10 17 24.13	-20 47 00.4	2	A	12600	V=17.4	116
				B	7200	V=19.4	36
Q1355-2257	13 55 43.38	-22 57 22.9	2	A	13500	g=17.7	46
				B	17100	g=19.6	50
SDSSJ0806+2006	08 06 23.7	20 06 31.9	2	A	4500	V=19.2	18
				B	6300	V=19.8	18
SDSSJ1335+0118	13 35 34.8	01 18 06.0	2	A	12300	g=18.1	63
				B	14100	g=19.4	38
WFI2033-4723	20 33 42.08	-47 23 43.0	1	A	12600	g=16.8	62
				B	12600	g=18.6	37
HE2149-2745	21 52 07.44	-27 31 50.2	1	A	3600	B=17.3	69
				B	7200	B=18.9	44
HE0230-2130	02 32 33.1	-21 17 26	1	A	3600	B=19.3	31
				B	2350	B=20.1	11

The fwhm calculated with 3 pixels is ~ 67.4 km/s for the entire sample.

[a](1) August 2009, (2) March 2010
[b]Median S/N of final reduced spectrum

2.2 MagE sample

The targets were selected carefully for their observability in terms of separation/brightness/redshift. Also some of their low-resolution spectra show damped $Ly\alpha$ systems. Tables 2.1 and 2.2 show the main observational and physical properties of the sample. Figure 2.1 shows the images of the lensed quasars.

2.2.1 Notes on individual objects

- *Q1017-207.* Doubly imaged quasar. The redshift of the lens galaxy ($z_{lens} = 0.78$) was calculated using a fundamental plane method in Kochanek et al. (2000) and the colors are consistent width an early type galaxy (Lehár et al. 2000). Ofek et al. (2006) could not obtain a spectroscopic redshift but it is suggested that the MgII system detected at $z = 1.088$ seen in both lines of sight could also be the lensing galaxy.

- *Q1355-2257.* Two-image quasar. Eigenbrod et al. (2006) found that the lens spectrum suggests an early type galaxy at redshift of $z_{lens} = 0.701$ but the spectrum had a low signal to noise. In Eigenbrod et al. (2007) the lens redshift is confirmed to $z_{lens} = 0.702$ by a MgII absorption only seen in image B.

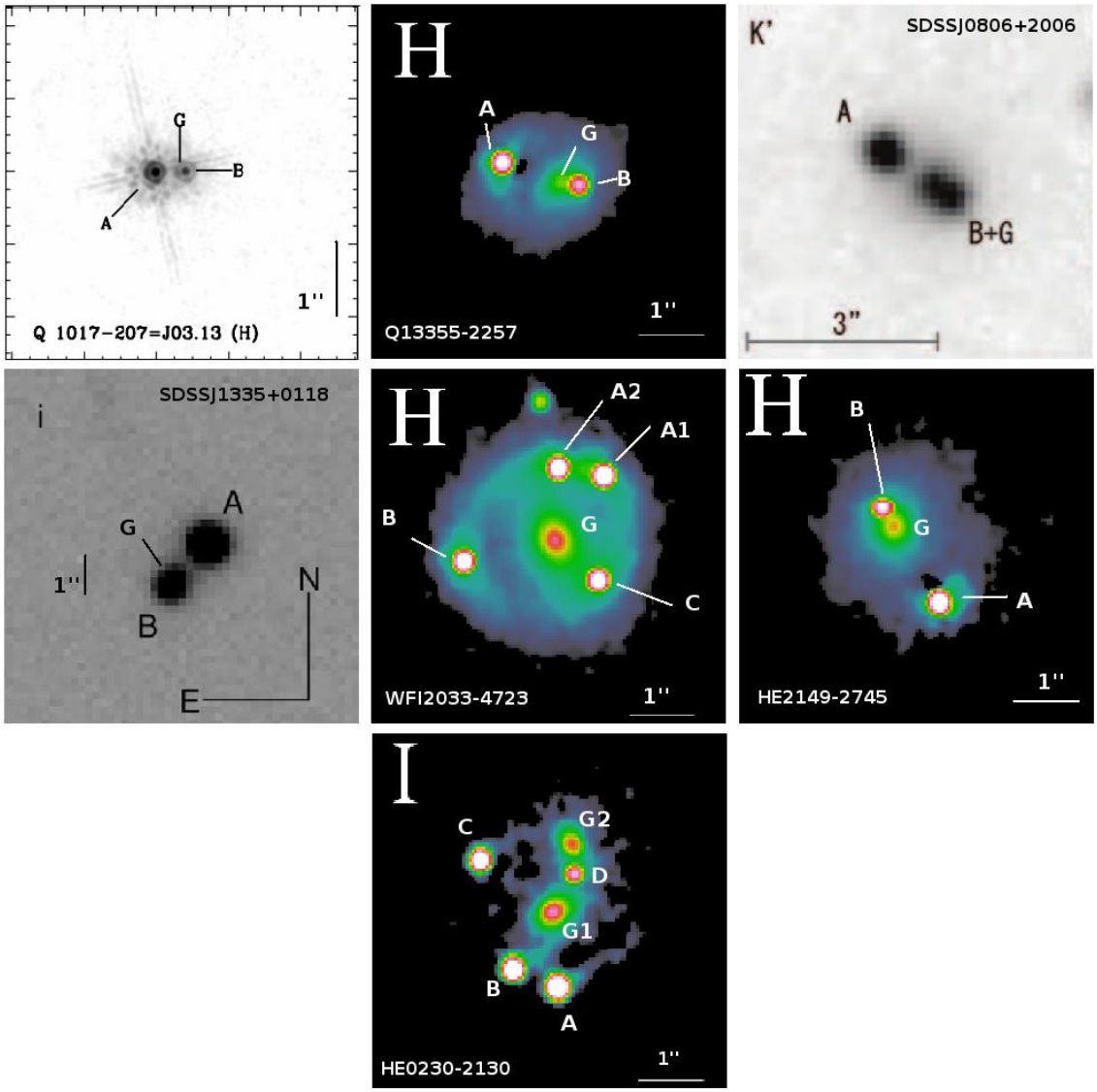

Figure 2.1: Images of lensed quasars of the MagE sample. The band of each image was selected in order to show as best as possible the configuration of the lens. *Q1017-207*: figure from Lehár et al. (2000). *Q1355-2257, WFI2033-4723, HE2149-2745,HE0230-2130*: figures from CASTLES (Kochanek et al. 1999). *SDSSJ0806+2006*: figure from Inada et al. (2006). *SDSSJ1335+0118*: figure from Oguri et al. (2004)

Table 2.2: Physical properties of the MagE sample.

QSO	z_{em}	z_{lens}	θ''	$D_{AB}(z_{lens})^a$ $[h_{70}^{-1}$ kpc]	$z_{min}{}^b$	$z_{max}{}^c$
Q1017-207	2.55	0.78±0.07	0.85	6.32	0.54	2.38
Q1355-2257	1.37	0.702±0.001	1.23	8.79	0.11	1.33
SDSSJ0806+2006	1.54	0.573±0.001	1.40	9.14	0.11	1.50
SDSSJ1335+0118	1.57	0.44±0.001	1.56	8.88	0.12	1.53
WFI2033-4723	1.66	0.661±0.001	2.26	15.77	0.16	1.62
HE2149-2745	1.70	0.603±0.001	1.70	11.37	0.17	1.66
HE0230-2130	2.16	0.523±0.001	1.90	11.88	0.34	2.11

[a]Distance between the A and B images at the redshift of the lens.

[b]Minimum redshift for searching MgII systems. It is defined as the maximum between the MgII redshift at the $Ly\alpha$ wavelength emission and the redshift given by the minimum wavelength of the spectrum.

[c]Maximum redshift for searching MgII systems. It is defined as the minimum between the MgII redshift at 5000 km/s from the MgII 2796 wavelength quasar emission and the redshift given by the maximum wavelength of the spectrum.

- *SDSSJ0806+2006.* Two-image quasar. Eigenbrod et al. (2007) finds a spectroscopic redshift $z_{lens} = 0.573$ for the lens galaxy. Also the spectrum is very similar to an elliptical template. Several absorption lines are found at the lens redshift.

- *SDSSJ1335+0118.* Two-image quasar. Eigenbrod et al. (2006) finds a spectroscopic redshift $z_{lens} = 0.44$ for the lens galaxy with a spectrum consistent with an elliptical galaxy.

- *WFI2033-4723.* Quadruple quasar. Ofek et al. (2006) measured a spectroscopic lens redshift of 0.658. In that work the spectrum matches a Sb and Sc galaxy template. However they also calculated a velocity dispersion consistent with a massive elliptical galaxy or a group and argue that the absorption futures most probably are not from a spiral galaxy. In Eigenbrod et al. (2006) a spectroscopic redshift $z_{lens} = 0.661 \pm 0.001$ was found for the lens and a spectrum consistent with an elliptical or S0 galaxy.

- *HE2149-2745.* Two-image quasar. Eigenbrod et al. (2007) found a spectroscopic redshift of 0.603 for the lens galaxy and a spectrum that matches an elliptical galaxy. This redshift is similar to one of a galaxy group in that field (Momcheva et al. 2006, Williams et al. 2006).

- *HE0230-2130.* Quadruple lensed quasar. This quasar has two lensing galaxies. The main lensing galaxy, G1, is located between the four quasar images. The fainter lens, G2, is located outside the four image area, close to image D (See figure 2.1). Eigenbrod et al. (2006) calculated a spectroscopic lens redshift of 0.523 and a lens

spectrum consistent with an elliptical galaxy for G1. For G2 they found a redshift of 0.526 and a spectrum similar to a Sa spiral galaxy. They conclude that this quasar might be lensed by a group of galaxies.

2.2.2 MagE observations and observing strategy

On August 2009 the weather conditions were not favorable and we could not open the telescope during the first night. In the second night we observed all night with seeing conditions oscillating between $0.9''$ and $1.6''$. A slit length of 1 arcsec was used for all objects. On March 2010 the seeing was excellent during the two nights, it varied between $0.5''$ and $0.7''$. In this case a slit width of 0.7 arcsec was utilized for all objects.

Bias were taken early in the afternoon. Th-Ar lamps for wavelength calibration were taken before and after each science exposure. A standard star was taken at the beginning and end of each night. These frames are used for order definition. For both calibrations, lamps and standard stars, the slit width is the same as for science objects.

The observational strategy was to observe each image separately. In each case, the slit was aligned with the parallactic angle in order to minimize chromatic slit losses, since the MagE spectrograph does not have an Atmospheric Dispersion Corrector. Normally we took two exposures of 2700 s each to the brighter image and two to four exposures of 3600 s each to the fainter QSO image.

In some cases both quasar images appear in the spectrum either because of the close separation, because of poor seeing conditions, or because of the alignment of the quasar images with the parallactic angle.

In the case of WFI2033-4723 the A line of sight corresponds to the sum of A1 and A2 unresolved images. For HE0230-2130, the A line of sight is the sum of the B and A unresolved images. The B line of sight is the one labeled with C. See figure 2.1.

2.3 UVES sample

Tables 2.3 and 2.4 show the main observational and physical sample properties respectively. Figure 2.2 shows the images of the lensed quasars.

Table 2.3: Main Observational conditions of the UVES sample.

QSO	RA	DEC	Date	Exptime [s]	S/N[a]
HE1104-1805	11 06 33.4	-18 21 23	Jan 2002, 2003	59020	72(A)-38(B)
HE0512-3329	05 14 10.9	-33 26 22	Jan 2003	24000	100(A-B)
RXJ0911+0551	09 11 27.6	05 50 54	Dec 2002, Feb 2003	43200	49(A)-9(B)

The fwhm calculated with 3 pixel is ~ 10.5 km/s and ~ 14.6 km/s for HE1104/RXJ0911 and HE0512 respectively. The seeing oscillated between 0.6 and 0.9 arcsec for HE0512 and 0.5-1.0 arcsec for HE1104/RXJ0911.

[a]Median S/N of final reduced spectrum

Table 2.4: Physical properties of the UVES sample.

QSO	z_{em}	z_{lens}	θ''	$D_{AB}(z_{lens})^a$ $[h_{70}^{-1}$ kpc]	$z_{min}{}^b$	$z_{max}{}^c$
HE1104-1805	2.31	0.729±0.001	3.20	23.26	0.44	1.45
HE0512-3329	1.58	0.931±0.001	0.64	5.03	0.65	1.00
RXJ0911+0551	2.80	0.769±0.001	3.06	22.67	0.65	1.40

[a]Distance between A and B at the redshift of the lens.

[b]Minimum redshift for searching MgII systems. It is defined as the maximum between the MgII redshift at the Ly_α wavelength emission and the redshift given by the minimum wavelength of the spectrum.

[c]Maximum redshift for searching MgII systems. It is defined as the minimum between the MgII redshift at 5000 km/s from the MgII 2796 wavelength quasar emission and the redshift given by the maximum wavelength of the spectrum.

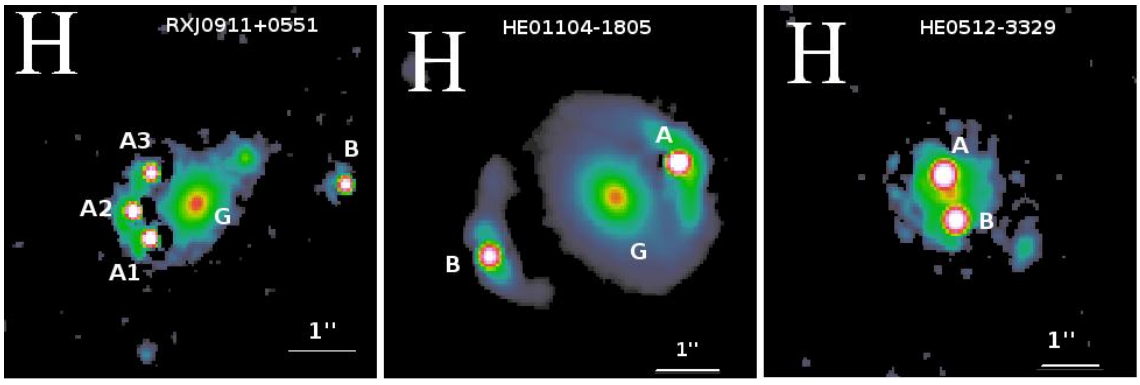

Figure 2.2: Images of lensed quasars of the UVES sample. Figures from CASTLES (Kochanek et al. 1999).

2.3.1 Notes on individual objects

- *HE1104-1905.* Doubly imaged quasar. The redshift of the lens galaxy, $z_{lens} = 0.729$, was calculated by Lidman et al. (2000). The lens galaxy colors are consistent with an early type galaxy (Lehár et al. 2000). This lensed quasar is unusual because the lens is close to the bright image instead of the faint one. Lehár et al. (2000) also claims that the image separation of $3.2''$ is much larger than that of a typical lens, suggesting the presence of a group or cluster. Also Courbin et al. (2000) modeled the system and concluded that the lens is probably composed of a red galaxy (seen between the quasar images) and a more extended component associated with a galaxy cluster with fairly low velocity dispersion.

  This lens system was already studied in Smette et al. (1995) and in Lopez et al. (1999, 2007).

- *HE0512-3329.* Doubly image quasar. The optical spectrum shows strong absorption features of Mg II, Mg I, Fe II, Fe I, and Ca I, all at an identical intervening redshift of z=0.9313, and is thought to be associated with the lens galaxy (Gregg et al. 2000). No spectroscopic redshift has been calculated directly from the lens spectrum.

- *RXJ0911+0551*, Quadruple system. The lens configuration is complex, being composed of one main lensing galaxy at $z_{lens} = 0.769$ and a cluster at redshift $z_{cl} = 0.7689 \pm 0.002$ distant by $38''$ of the system (Kneib et al. 2000). The color of the main lens is similar to the galaxies of the cluster, early type galaxies (Burud et al. 1998).

2.3.2 UVES observations and observing strategy

The UVES observations are described in Lopez et al. (2005) and Lopez et al. (2007). The most notable difference with the MagE observations is that, since UVES has an Atmospheric Dispersion Corrector, the spectra of both quasar images were acquired simultaneously by aligning the slit with the two images. In the case of RXJ0911+0551 the A image corresponds to the integration of A1, A2 and A3 (see Figure 2.2).

Chapter 3

Data Reduction

I reduced the seven MagE QSOs spectra using a software developed by Prof. Sebastián López. This software is composed of FORTRAN routines which interact with MIDAS commands. The UVES data had been reduced before with the same software.

In short, the extraction method is based on fitting a Gaussian function along the spatial direction to each of the QSO profiles simultaneously in the 2-D spectra. The area of the Gaussian and its error correspond to the flux and the flux error respectively, and these are mapped into a 1D spectrum.

In the following sections I detail all steps of the MagE reductions. At the end of the chapter some special cases are discussed.

3.1 Reduction outline

3.1.1 Preprocessing

Before extraction, all images (standard stars, Th-Ar lamps and quasars) must be pre-processed in order to convert DNs[1] to photo e^- and to correct for the bias. First, the raw images are flipped to get the wavelengths increasing to the right. Then, the counts are converted to photo e^- by multiplying by the CCD gain. Finally, a constant bias is subtracted. I calculated the constant value from a combined bias. The bias level does not need to be accurate since the sky is subtracted independently (and locally).

[1] Digital Number

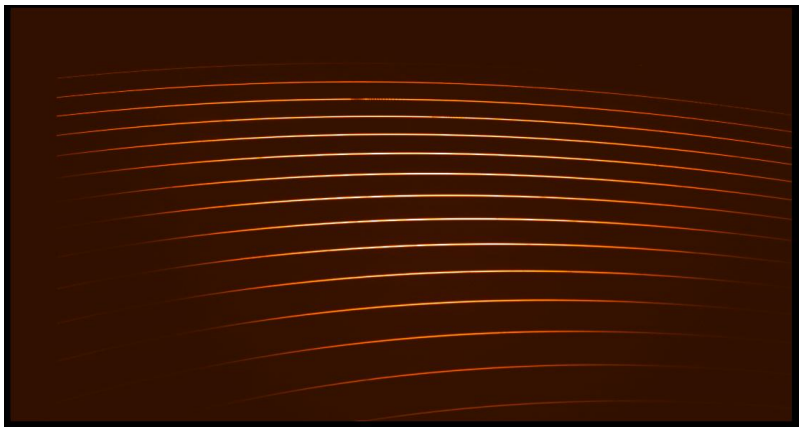

Figure 3.1: Spectrum of the standard star HD4979B after preprocessing.

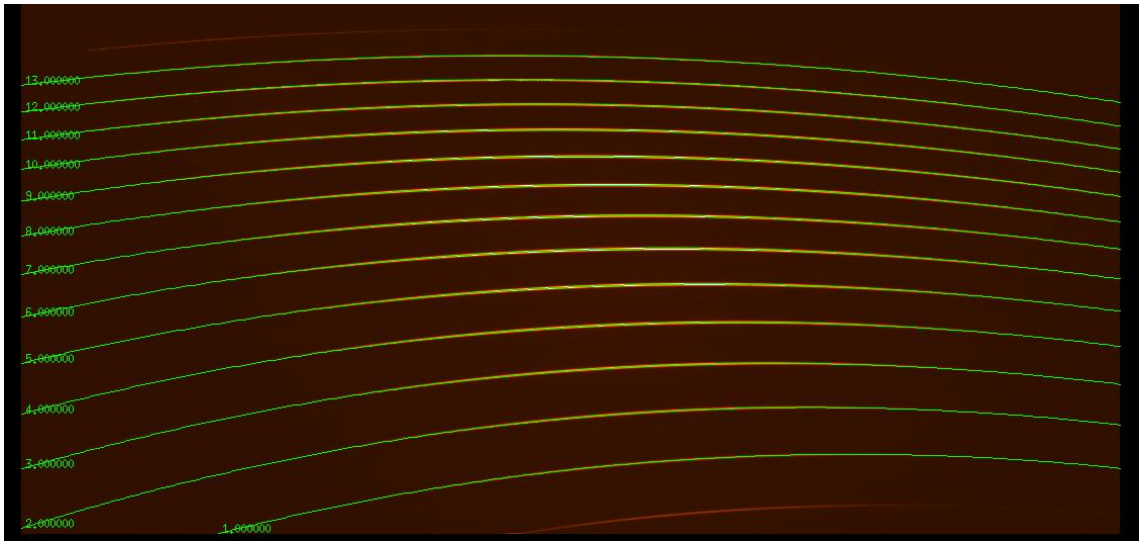

Figure 3.2: Spectrum of standard star HD4979B with orders positions overlaid.

3.1.2 Order definition

Spectra of standard stars are used to trace the orders in the 2D spectra. As explained in 2.1, the orders present a curvature (figure 3.1).

The first order begins at approximately 3000 Å, and therefore hot stars were selected as standards, in order to have enough flux in the lowest orders. The positions were found using the MIDAS task DEFINE/HOUGH restricted to detect 13 orders. Figure 3.2 shows the position of the orders in the standard star of figure 3.1.

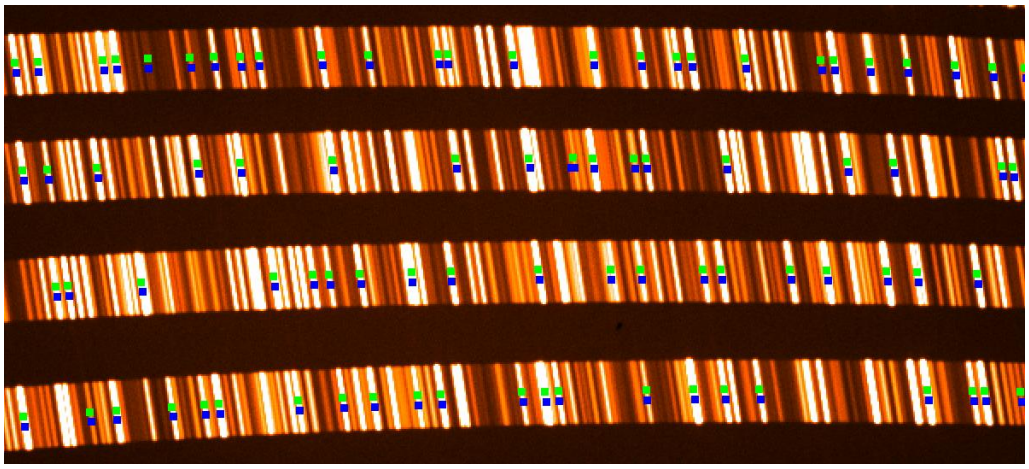

Figure 3.3: A section of the spectrum of a Th-Ar lamp. The slit width and the exposure time are 0.7" and 8 s respectively . The green and blue squares are the common identified lines at position ±3 from the order definition.

3.1.3 Tilt Rectification

As mentioned in 2.1, the MagE spectra present a spectral line tilt (i.e. misalignment with respect to CCD columns). The rectification process corrects the line tilt using the Thorium-Argon (Th-Ar) lamp image.

Using the command EXTRACT/ECHELLE two spectra of the lamp are extracted at an offset of $\pm n$ pixels from the position of the order (that it can be an offset of the central position). The value of n is set by inspecting the different results. I finally used a value of $n = 3$ pixels. In each extracted spectra, lines are searched using the command SEARCH/ECHELLE. This command detects lines using a thresholding algorithm. The center of the lines is estimated by a gaussian fit to the line profile. Once the lines are detected at these two different position, a tilt angle is calculated for each line by calculating the slope of the line crossing the two identification. A polynomial of degree two is fitted to the angle as a function of position across the orders, so an angle can be computed for each position. Figure 3.3 shows some lines detected at the two positions. Figure 3.4 is a plot of the tilt angles calculated for each order and their fit.

Finally, I corrected the 2D spectrum by projecting each pixel, corresponding to the same wavelength, on a vertical line along the spatial direction. Each order in the rectified spectrum is set to have a given slit length. Figures 3.5 and 3.6 show the original and the rectified lamp spectrum.

The spectrum of the standard star used for order definition is also corrected and the order positions are recalculated.

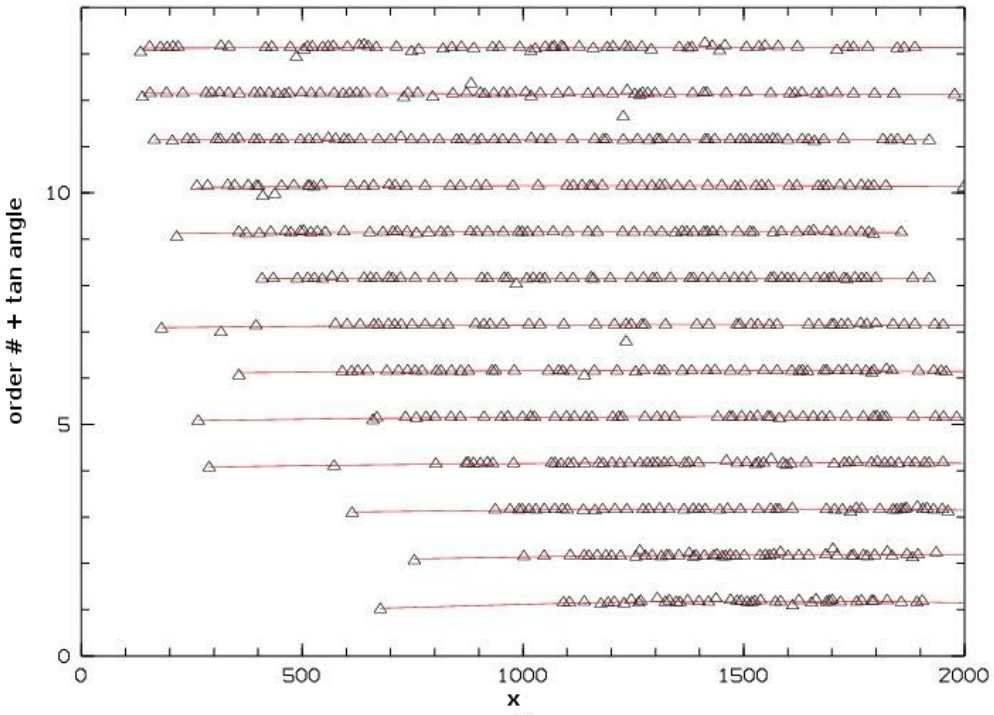

Figure 3.4: The triangles are the value of the tangent of the tilt angle plus the order number. They are plotted vs the position in the dispersion direction. The fit to each order is in red.

I calculated a rectification solution for each run of observations. Each science spectrum is rectified using its corresponding solution.

3.1.4 Wavelength calibration

I used the command IDENTIFY/ECHELLE to perform the wavelength calibration using the rectified 2D Th-Ar lamp spectrum.

The first step is to set the wavelength and pixel position of two lines in the 2D spectrum. The lines selected have to appear in the overlapping region of two orders. Therefore, four positions are placed, along with both wavelengths and the absolute order number[2] of each line. Figure 3.7 shows the lines used.

Using this information the task calculates the coefficients of a four degree polynomial that relates the wavelength in each order with the pixel position. These coefficients are the first approximation of the dispersion relation. After this, an iterative loop improves the first solution by identifying more lines. An estimation of wavelengths from the previous solution and a list of laboratory wavelengths is taken into account for the line identification.

[2]The order number that satisfies the grating equation

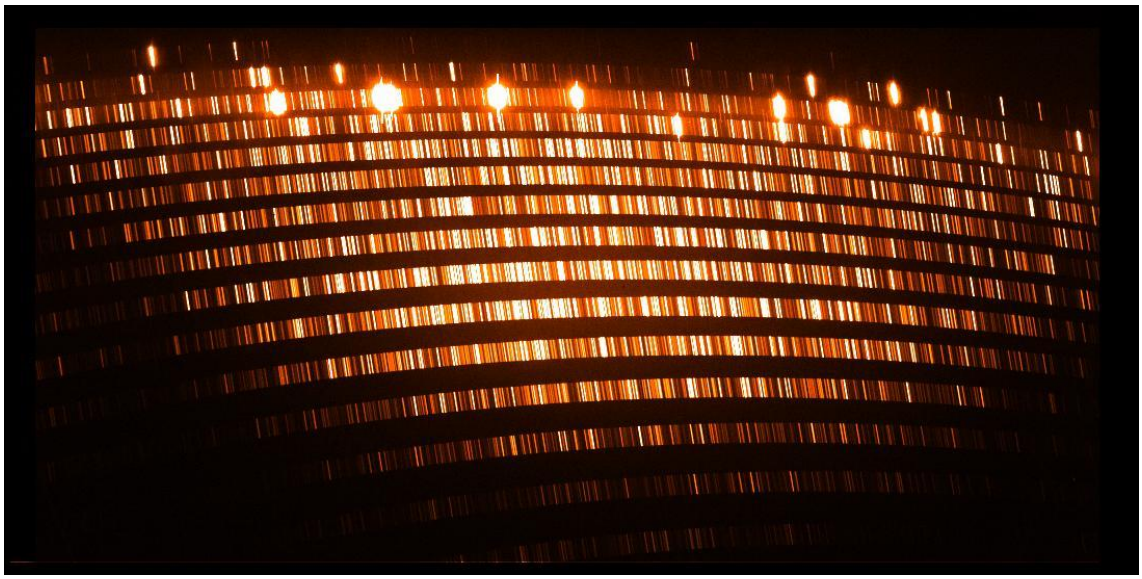

(a) Spectrum of a Th-Ar lamp before rectification

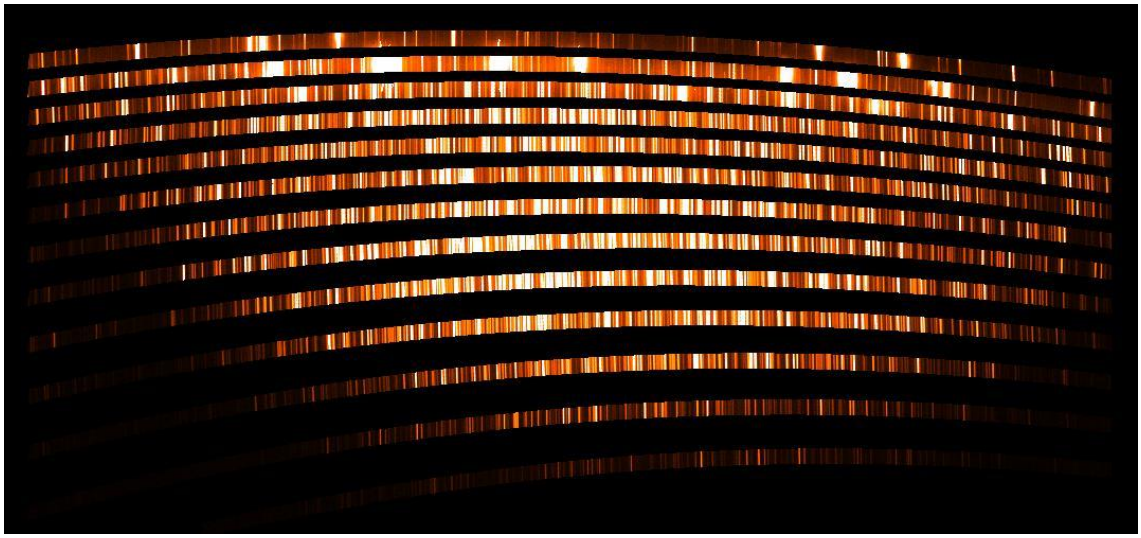

(b) Spectrum of a Th-Ar lamp after rectification

Figure 3.5

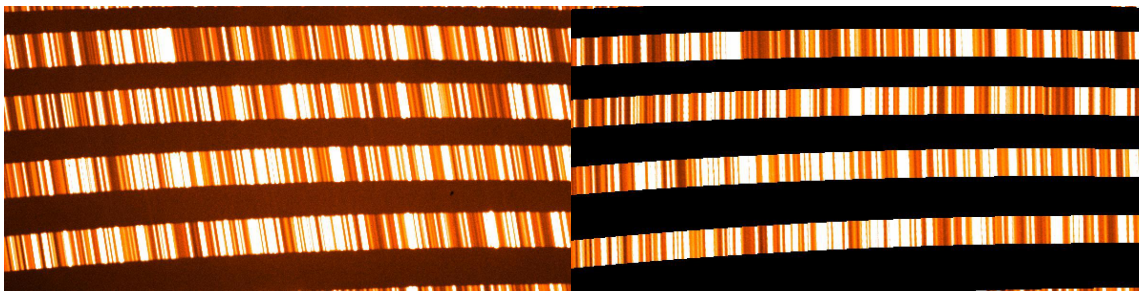

(a) **(b)**

Figure 3.6: Same as figure 3.5 but in the central part of the spectrum.

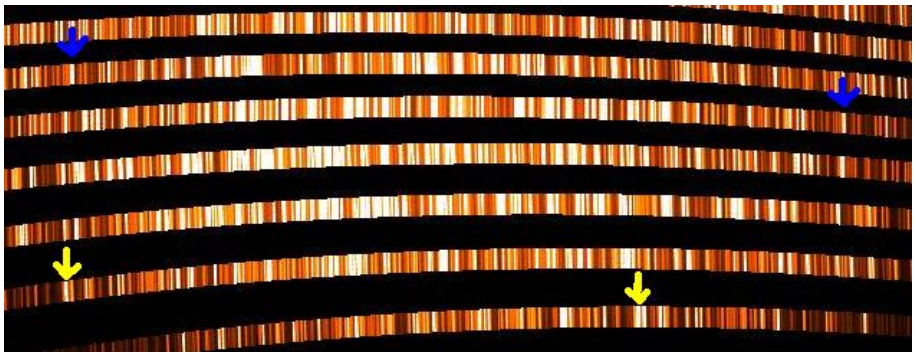

Figure 3.7: Pairs of lines used to start the calibration for both runs of observation. In yellow(blue) the lines wavelength is 3719.434(4965.080) $\mathring{A}$. The lines are in the orders 3-4 and 7-8.

The wavelength list used was originally made for the MIKE spectrograph[3] (R∼30 000 - 80 000). In order to improve the identification, I deleted those lines that were blended at the resolution of MagE . In those cases I only considered the wavelength of the strongest emission. See one example in figure 3.8.

The wavelengths of the two pairs of lines defined at the beginning and the lines atlas of MIKE were in the air and hence, the entire dispersion relation was calculated in terms of air wavelengths.

Table 3.1 contains a summary of the number of identified lines and the wavelength range per order for the calibration made for March observations. Also is given a column with the standard deviation of the solution for each order. The sample[4] value obtained is 0.3747 Å. A slit width of 0.7 arcsec was utilized for this run. For the second run we used a slit of 1 arcsec and the sample value obtained is 0.3744 Å.

The selection of the offset position at which the lines will be searched is critical. In the last orders there are some saturated emissions. The charge accumulated spills over adjoining pixels, even bleeding onto another order. This effect creates a false line (figure 3.9). The calibration on these orders is not accurate if the extraction is made at the position of one of these false lines.

Finally, the calibration can be inspected by verifying that the lines in the overlapping regions of two orders have the same wavelength. Figure 3.10 shows these regions for the calibration of the first observation date.

The resolution reached in each run of observations can be calculated by fitting a Gaussian profile to Th-Ar emission lines. The slope of the linear fit to the plot of wavelength versus fwhm is the resolution ($R = \lambda / fwhm$). I obtained the resolution values ∼4425 and ∼4450

[3]Echelle spectrograph mounted on Clay telescope, at Las Campanas Observatory.
[4]Size of the pixel in wavelength units.

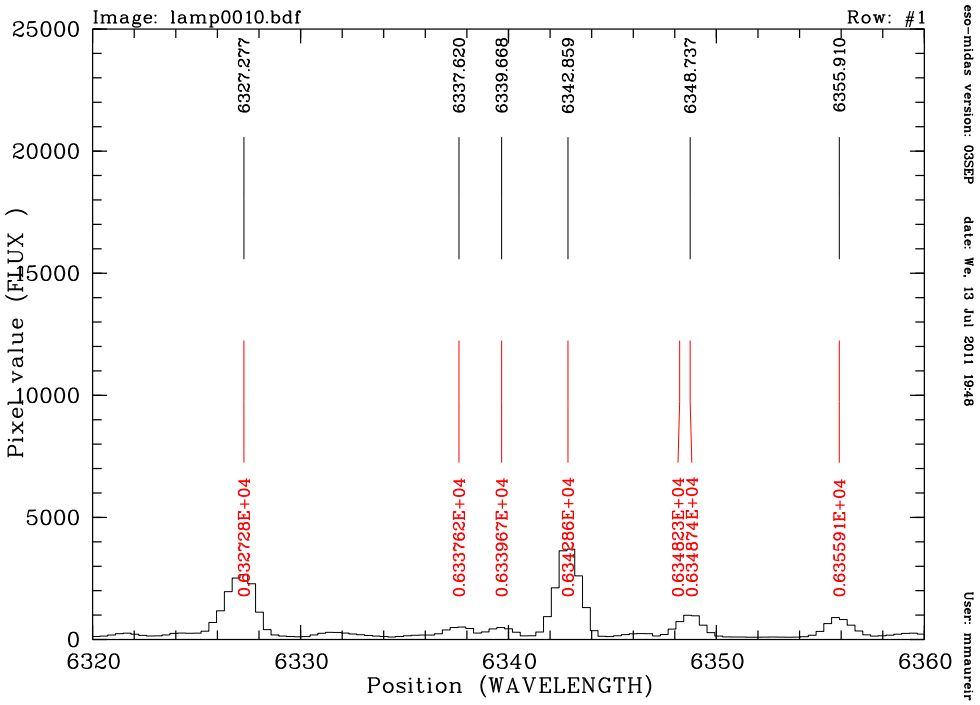

Figure 3.8: Th-Ar lamp, order= 10, $\text{slit}_{width} = 1''$. Example of a pair of lines (6348.2 – 6348.7 Å) not resolved at MagE resolution. In red are the Th-Ar lines for MIKE and in black are the transitions considered to identify lines in MagE spectra.

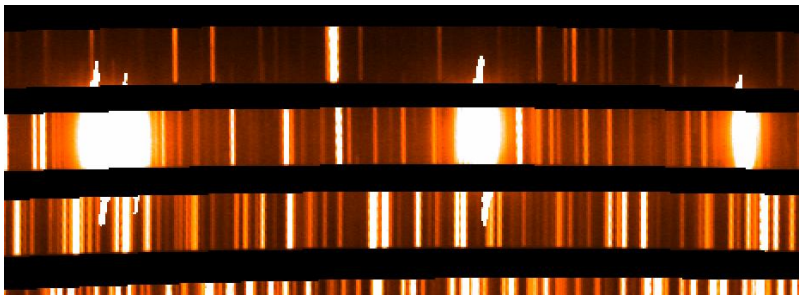

Figure 3.9: Orders 11, 12 and 13 show these saturated pixels that create false lines in adjoining orders.

Table 3.1: Results from the wavelength calibration of the Th-Ar lamp with a slit width of 0.7" and 8 s of exposure. This calibration was used over all objects of the second run.

Abs order number	No identified lines	Wavelength start	Wavelength end	Std. Dev Å
19	26	2825.25	3483.61	0.06626
18	48	3124.17	3679.85	0.05592
17	47	3307.71	3896.87	0.07752
16	55	3512.64	4140.82	0.05690
15	59	3747.53	4417.28	0.08617
14	61	4015.86	4733.26	0.03867
13	64	4325.47	5097.56	0.07342
12	62	4687.10	5522.71	0.08768
11	72	5113.71	6024.96	0.07641
10	76	5625.86	6627.56	0.07955
9	49	6251.64	7364.23	0.07327
8	75	7034.16	8285.05	0.06324
7	50	8039.62	9468.54	0.08288

for the first and second run respectively.

3.1.5 Extraction

The first step in the process is to calculate a variance image (V) . This image corresponds to the weights used later by the method that finds the best gaussian fit to the quasar continuum. The variance for each pixel i, j of V is defined as:

$$\sigma_{i,j}^2 = \left(\sqrt{f_{i,j}^{obj}}\right)^2 + \left(\sqrt{f_{i,j}^{sky}}\right)^2 + ron^2$$

where $f_{i,j}^{obj}$ and $f_{i,j}^{sky}$ are the quasar and sky fluxes in the i, j pixel respectively, and ron is the read out noise[5]. Therefore, V can be calculated by adding ron^2 to every pixel on the quasar 2D spectrum (Q). However, in order to avoid pixels affected by cosmic rays, I create a new 2D quasar spectrum (Q_{new}), in which, cosmics can be identified by their high flux values. To detect those pixels I make a mask image $Q_{mask} = Q/Q_{median}$, where Q_{median} is a median filtered image of Q. Then, the flux of each pixel i, j of Q_{new} is the same as pixel i, j of Q except when the pixel in Q_{mask} had a value over certain threshold. In the later case, a value of 10^8 is set to the pixel. The threshold value has to be low enough to detect weak cosmics, but high enough to not detect absorption lines or continuum. I usually used a value of 2.5. Finally, V is calculated as $Q_{new} + ron^2$. Figure 3.11 shows some examples of the result of this process.

As mentioned before, the goal is to fit a Gauss function to the spatial profile of the quasar for each position in the dispersion direction. All these Gaussian profiles conform a synthetic 2D spectrum of the real spectrum.

Along with replacing the emission of the quasar by a gaussian profile, the sky is recovered by using a constant value for its emission. Therefore, to compute the synthetic image, there are four variables for each pixel in the dispersion direction: the amplitude, standard deviation and the position along the spatial direction of the Gaussian profile, and the constant value for the sky. In the case of having both quasar traces in the spectrum, the position and amplitude of the second Gaussian must be added . In this later case, since the image of both lines of sight are separated by a constant angular distance in the sky, one might expect that the position of one continuum is fixed with respect to the position of the other quasar continuum. Nevertheless, due to the projection made to rectify the spectra, the distance between the continuum can vary along and between the orders. This is the reason to consider the second position also as a free parameter. Later, in the extraction,

[5] 3.1 e^- in this case.

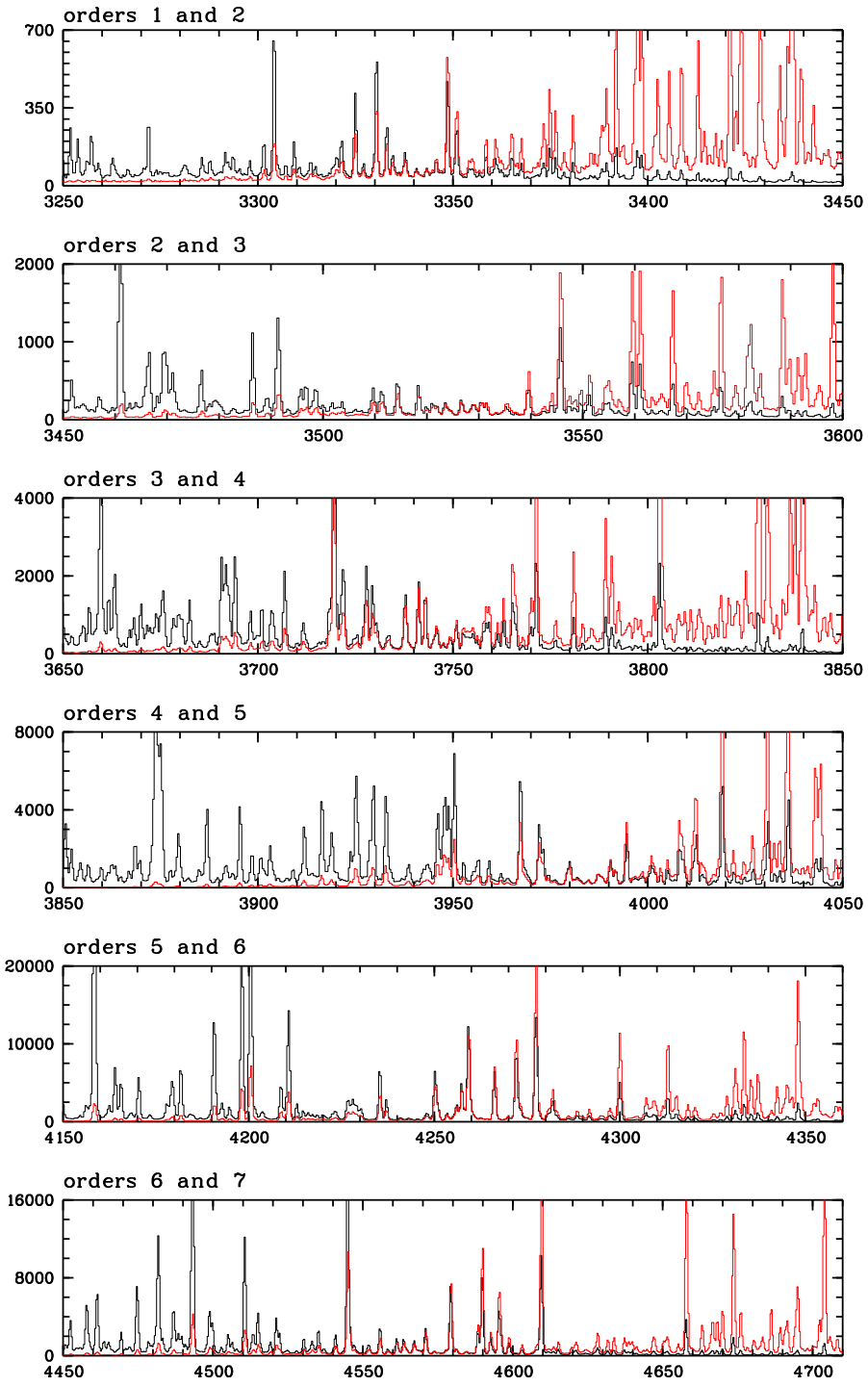

(a)

Figure 3.10: Overlapping regions from order 1 to 7 after wavelength calibration. All lines that appear in two orders have the same wavelength. This calibration was made with the Th-Ar lamp of 8s of exposure time and a slit width of 0.7" for the second run.

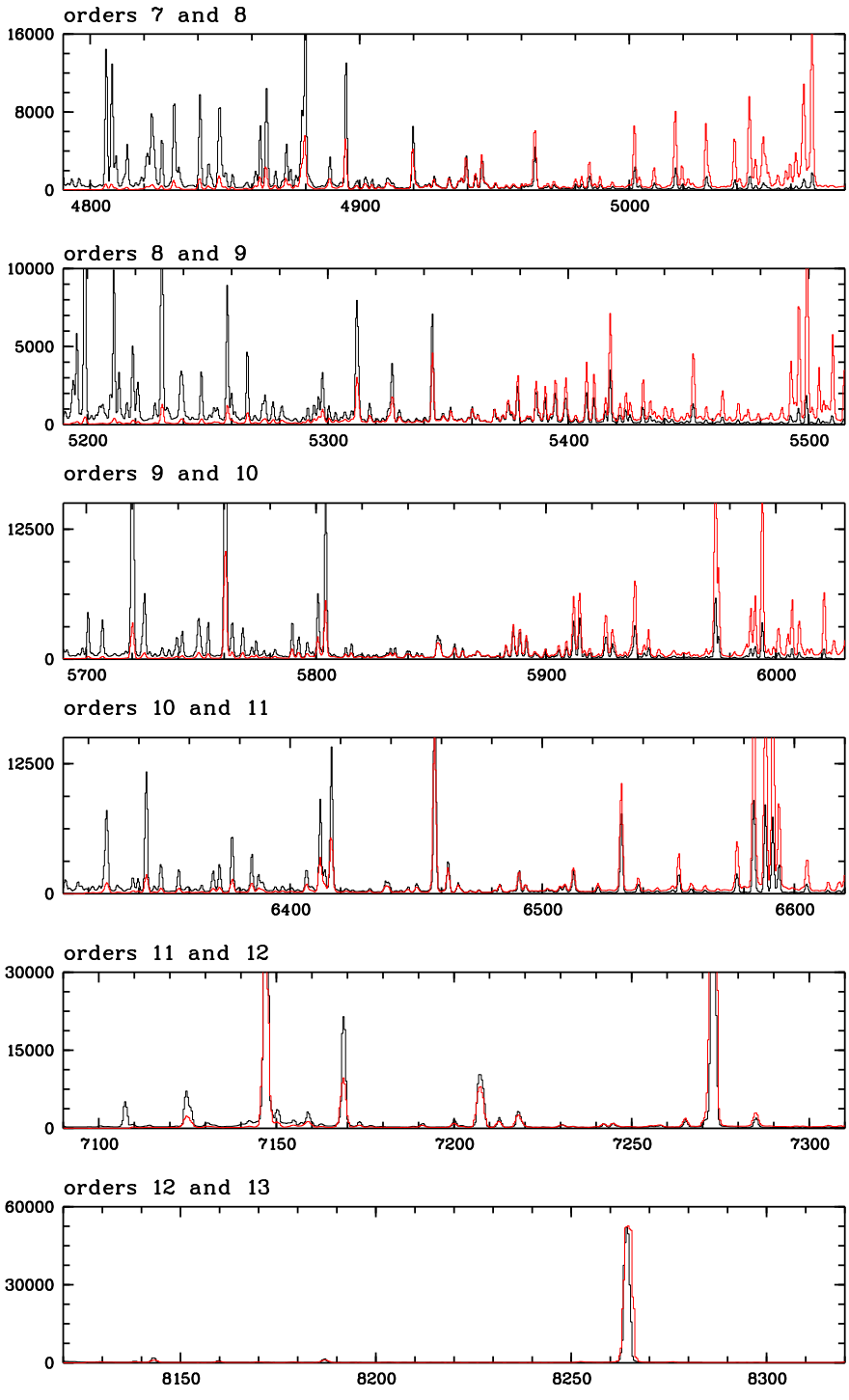

(b)

Figure 3.10: Overlapping regions from order 7 to 13. All lines that appear in two orders have the same wavelength. This calibration was made with the Th-Ar lamp of 8s of exposure time and a slit width of 0.7" for the second run.

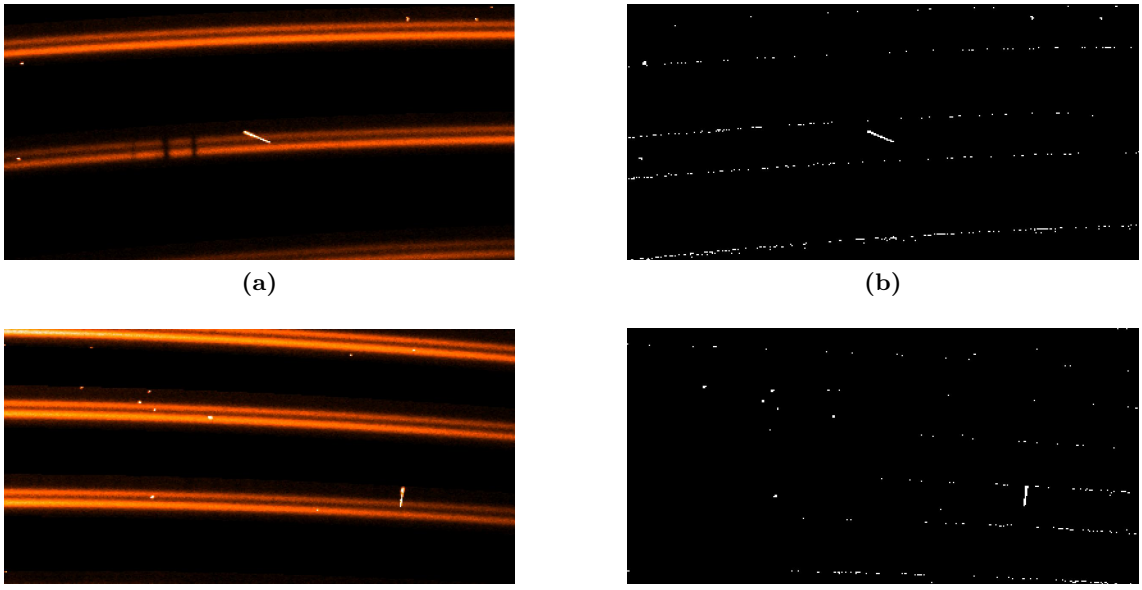

(a) **(b)** **(c)** **(d)**

Figure 3.11: Figures 3.11a and 3.11c are sections of one exposure of quasar WFI2033-4723 in which both sight of lines are observed at the same time. Some cosmics are observed over the traces. Figures 3.11b and 3.11b show the pixels of the variance image that have fluxes values of 10^8 due the process of cosmic identification.

the variation is detected (see figure 3.15). The standard deviation of the Gaussian, that represents the seeing conditions, is the same for both profile.

Figure 3.12 shows different plots of CCD columns. The Gaussian profiles and the sky contribution can be observed. Some absorptions, cosmics and sky lines also are shown.

Consider that both QSOs continuua are observed in the 2D spectrum, the second step of extraction is to set initial conditions for all the variables for each order and position. After I defined a center and length of the slit, I set the positions of one of the quasar continuum pos_1, as offsets from the slit center. The trace can have different positions for different orders. I used the sky position pos_{sky}, as an offset from the slit center that falls onto a sky region. I performed an extraction at each one of the pos_1, pos_2 and pos_{sky} values to obtain initial values for the gaussian amplitudes and the sky emission, int_1, int_2 and sky_0. A δ value is defined as $pos_1 - pos_2$, where pos_2 is the position of the other quasar continuum. In this first guess I calculate δ from the CCD scale[6] ($0.3''/pixel$) and the angular separation of the LOS. The standard deviation in pixels σ, is calculated from the seeing and the CCD scale.

In the third step, I calculate a synthetic 2D spectrum using these initials values and the Levenverg-Marquadt method, which performs a nonlinear least-square minimization. To

[6]Size of the pixel in sky angular units

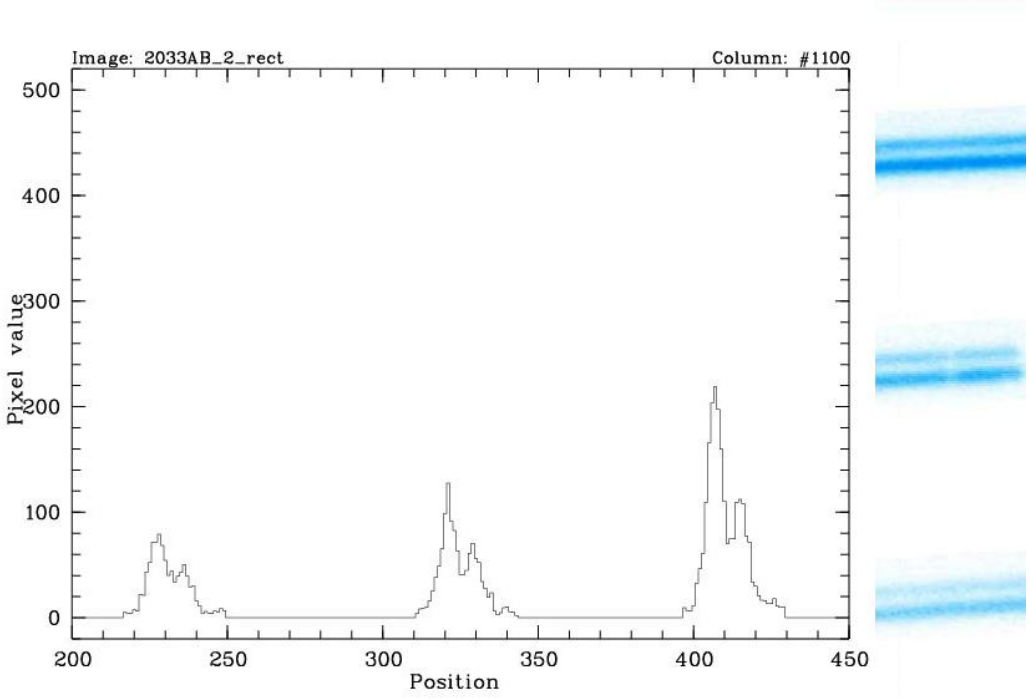

(a) QSO WFI2033-4723. $CCD_{column} = 1100$, $orders = 2, 3, 4$, $slit_{width} = 1''$.

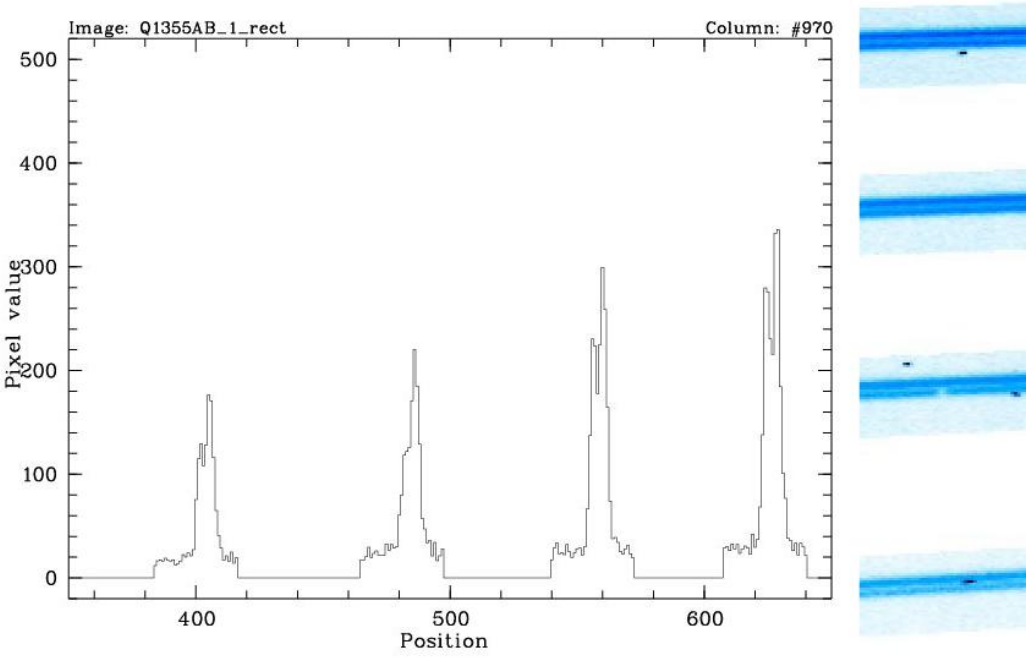

(b) QSO Q1355-2257. $CCD_{column} = 970$, $orders = 4, 5, 6, 7$, $slit_{width} = 0.7''$.

Figure 3.12: Left: Plot of a column of the 2D spectrum. Only some orders are shown. Right: Image of 2D spectrum that shows the orders seen at right. The center of the image is the column plotted. In figure 3.12a is observed both LOS at the same time as well as in 3.12b. In the last, there is an absorption in B LOS, the weaker, and it can be seen how that column only has one component in that order.

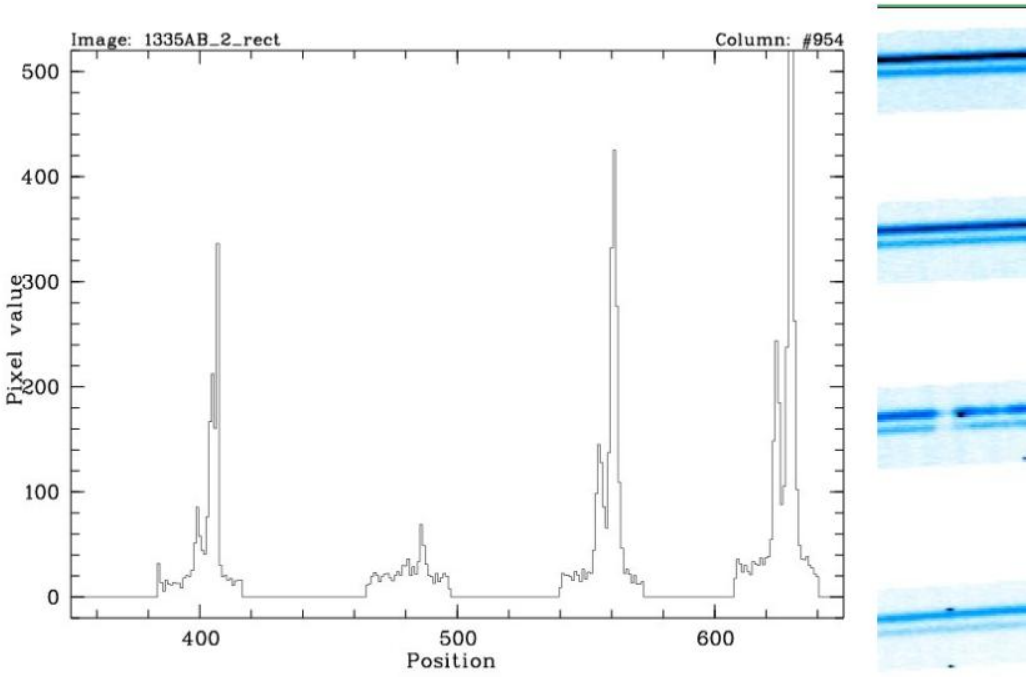

(c) QSO SDSSJ1335+0118. $CCD_{column} = 954$, $orders = 4, 5, 6, 7$, $slit_{width} = 0.7''$.

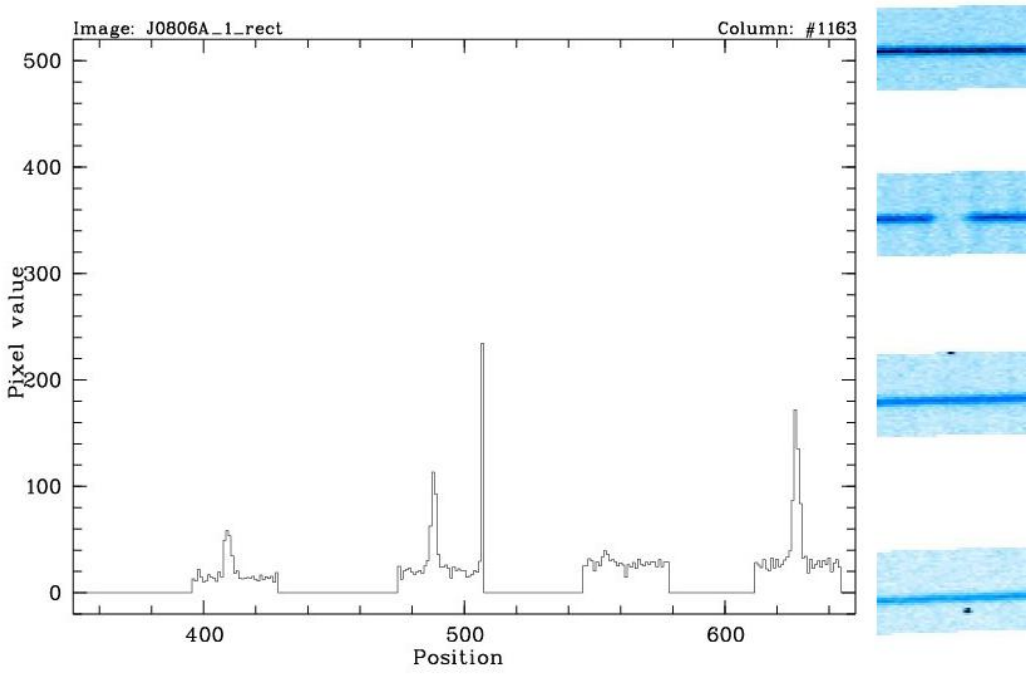

(d) QSO SDSSJ0806+2006. $CCD_{column} = 1163$, $orders = 4, 5, 6, 7$, $slit_{width} = 0.7''$.

Figure 3.12: Same as before. In figure 3.12c is observed both LOS at the same time. In 3.12d is only observed A LOS. Both present absorption in one order. In 3.12c all the continuum was absorbed in B, in A still something remain. In 3.12d the order 6 is completely absorbed.

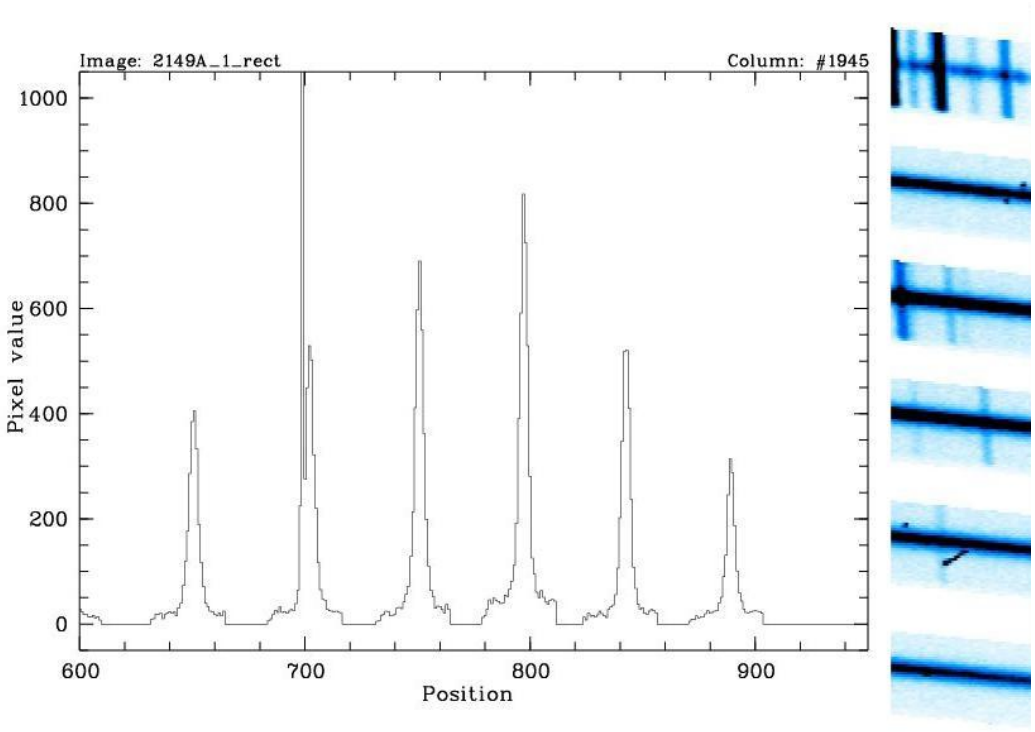

(e) QSO HE2149-2745. $CCD_{column} = 1945$, $orders = 7, 8, 9, 19, 11, 12$, $slit_{width} = 1''$.

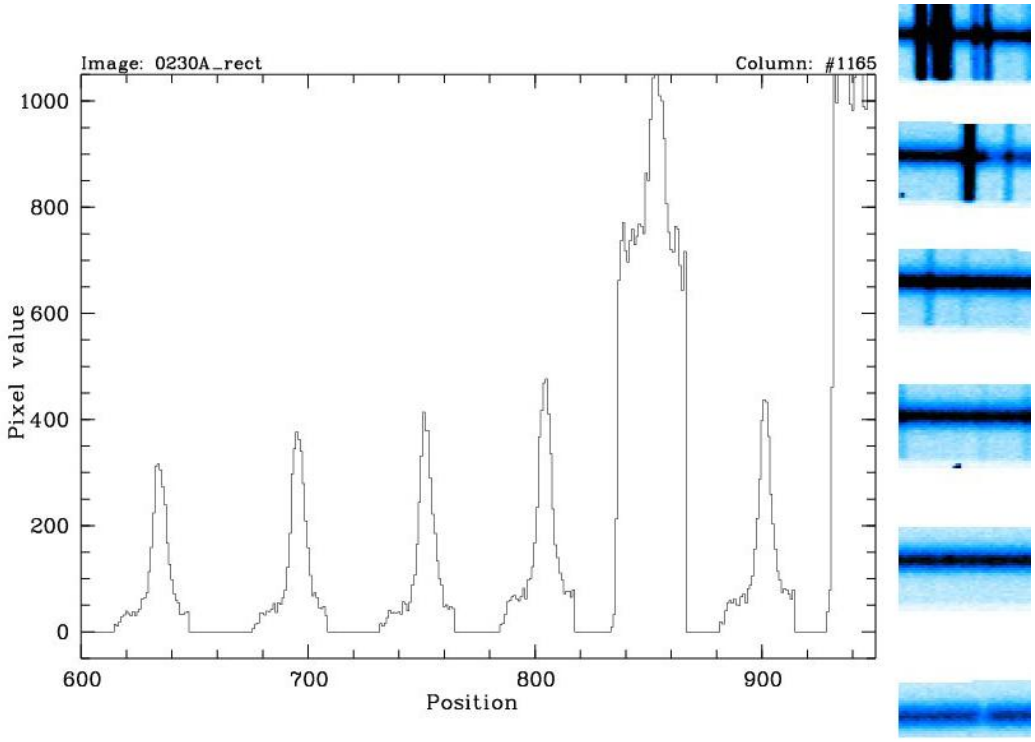

(f) QSO HE0230-2130. $CCD_{column} = 1165$, $orders = 7, 8, 9, 10, 11, 12$, $slit_{width} = 1''$.

Figure 3.12: Same as before. In 3.12e and 3.12f only A LOS is observed. In 3.12e there is a cosmic in order 8. In 3.12e can be observed a sky line in the order 11.

improve this first extraction, I fix three parameters σ, pos_1 and $delta$, at values found by fitting them, and then I repeat the minimization, this time only with three free parameters: sky_0, int_1 and int_2. In the case of pos_1 the fixed values are calculated from a polynomial of 3rd degree. This method was first used in Smette et al. (1992). For σ and δ, the fixed values correspond to the median in every order.

Figures 3.13, 3.14 and 3.15 show the values obtained for pos_1, σ and $delta$ after the first minimization from one exposure of QSO 1355-2257. Also I present the fits to each parameter. In figures 3.16 and 3.17 the real and the synthetic 2D spectrum of the same examples of figure 3.12 are compared. Figure 3.18 shows the same profiles of figure 3.12 in black, and in red the profiles obtained from the synthetic spectra.

I calculated the fluxes and their errors for both quasars from the finals values obtained for int_1, $error(int_1)$, int_2, $error(int_2)$ and σ. The fluxes correspond to the area of the Gaussians.

$$flux_{1,2} = int_{1,2} \cdot \sigma \cdot \sqrt{2\pi}$$

$$\sigma_{1,2}^{flux} = error(int_{1,2}) \cdot \sigma \cdot \sqrt{2\pi}$$

Finally I normalized both, fluxes and its errors, by the exposure time.

In those cases where only one quasar continuum was observed, int_2 is set to 0 for all calculations. In the first try there are four free parameters and, after the fit of σ and pos_1, the second attempt is made with only $int1$ and sky_0 as free parameters.

3.1.6 Vacuum and Heliocentric correction

The wavelength calibration solution is applied to the table that has the information of flux and σ_{flux} for each pixel position in the dispersion direction. Since the calibration was made with air wavelengths it is necessary to make the transformation to vacuum wavelengths.

The equation that relates both wavelengths is:

$$\lambda_{air} = \frac{\lambda}{n(\lambda)}$$

where λ_{air} and λ are the air and vacuum wavelengths respectively, and n is the air refractive

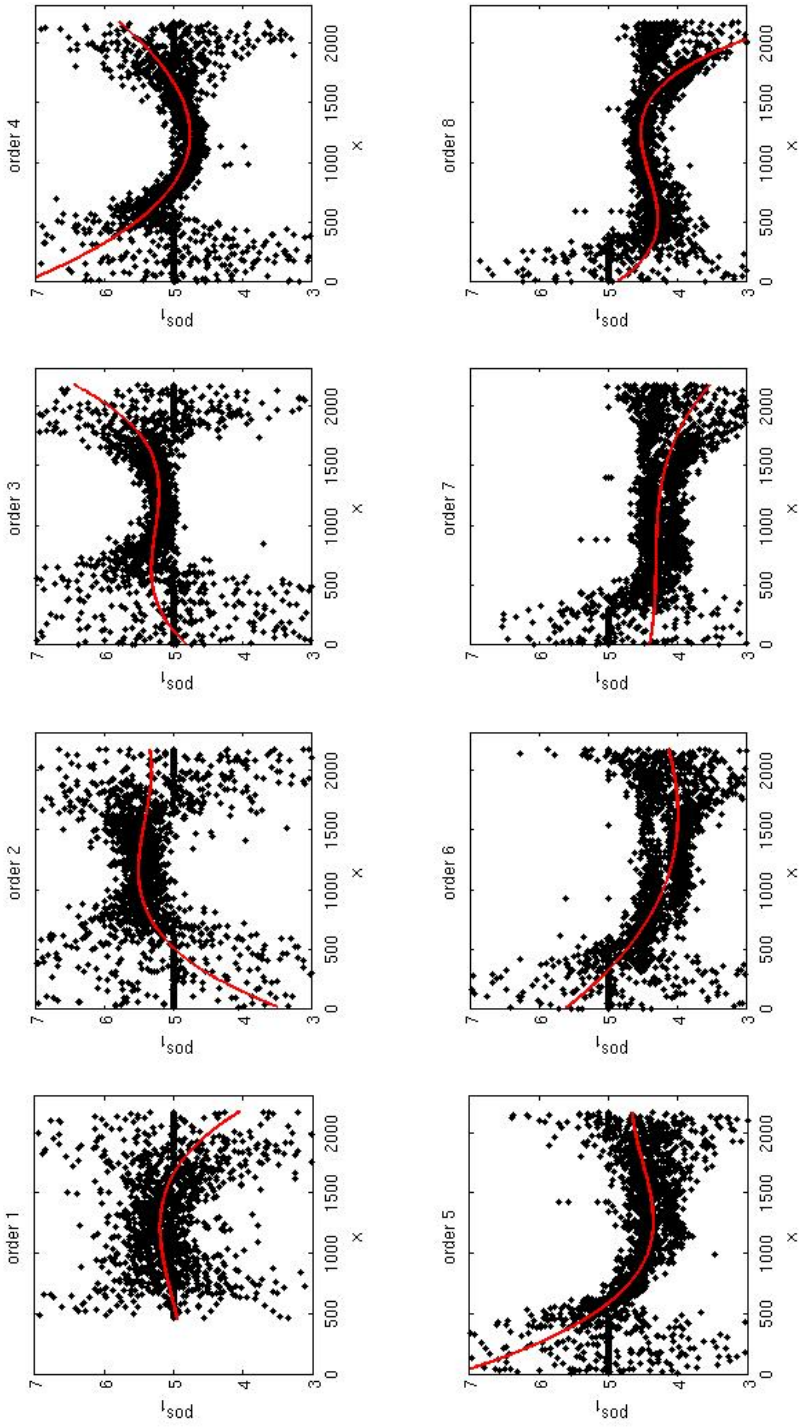

(a)

Figure 3.13: Black points are pos_1 versus position for each order after the first minimization. In red is the polynomial fit. For the second minimization this parameter is fixed to those of each polynomial. Orders 1-8. QSO 1355-2257, $slit_{width} = 0.7''$.

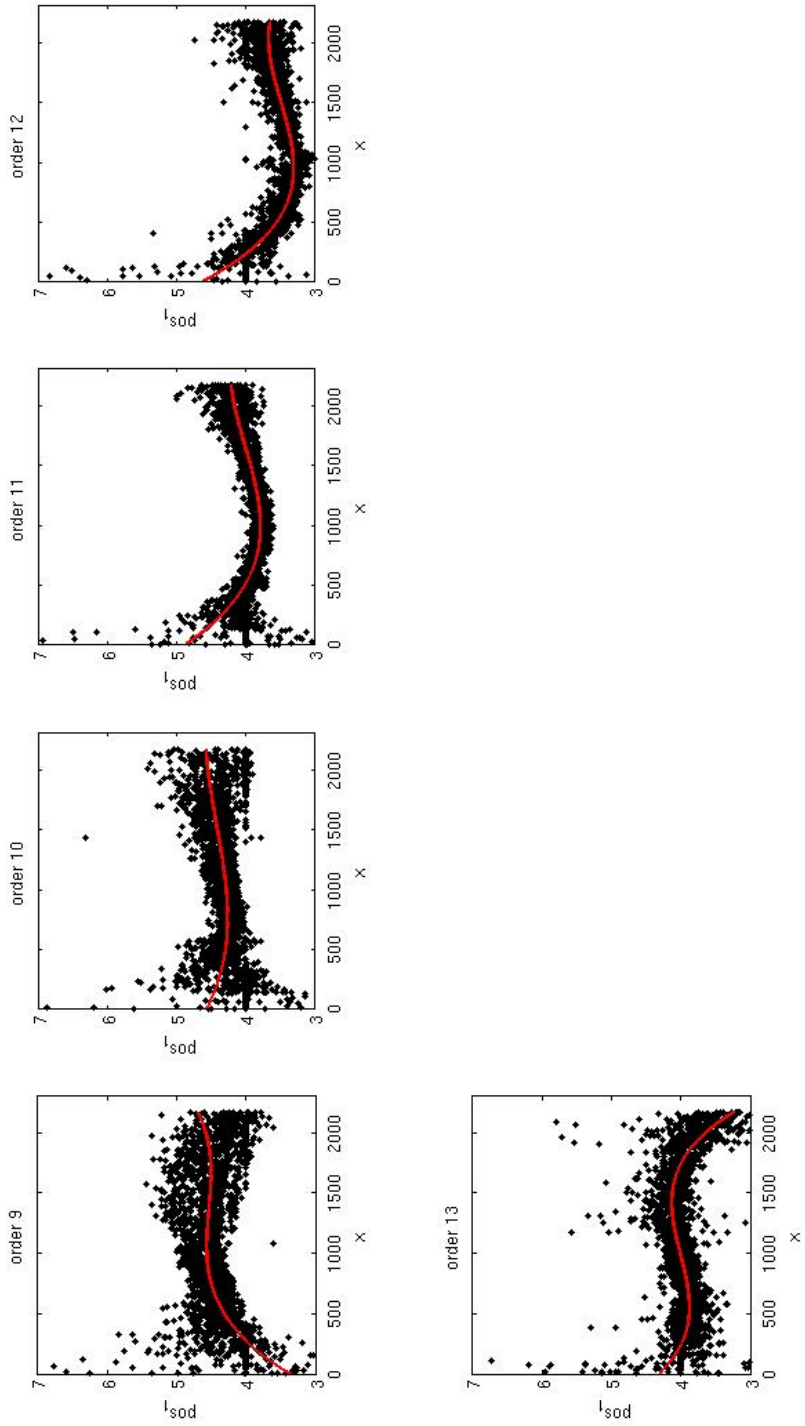

(b)

Figure 3.13: Similar to 3.13a for orders 9-13

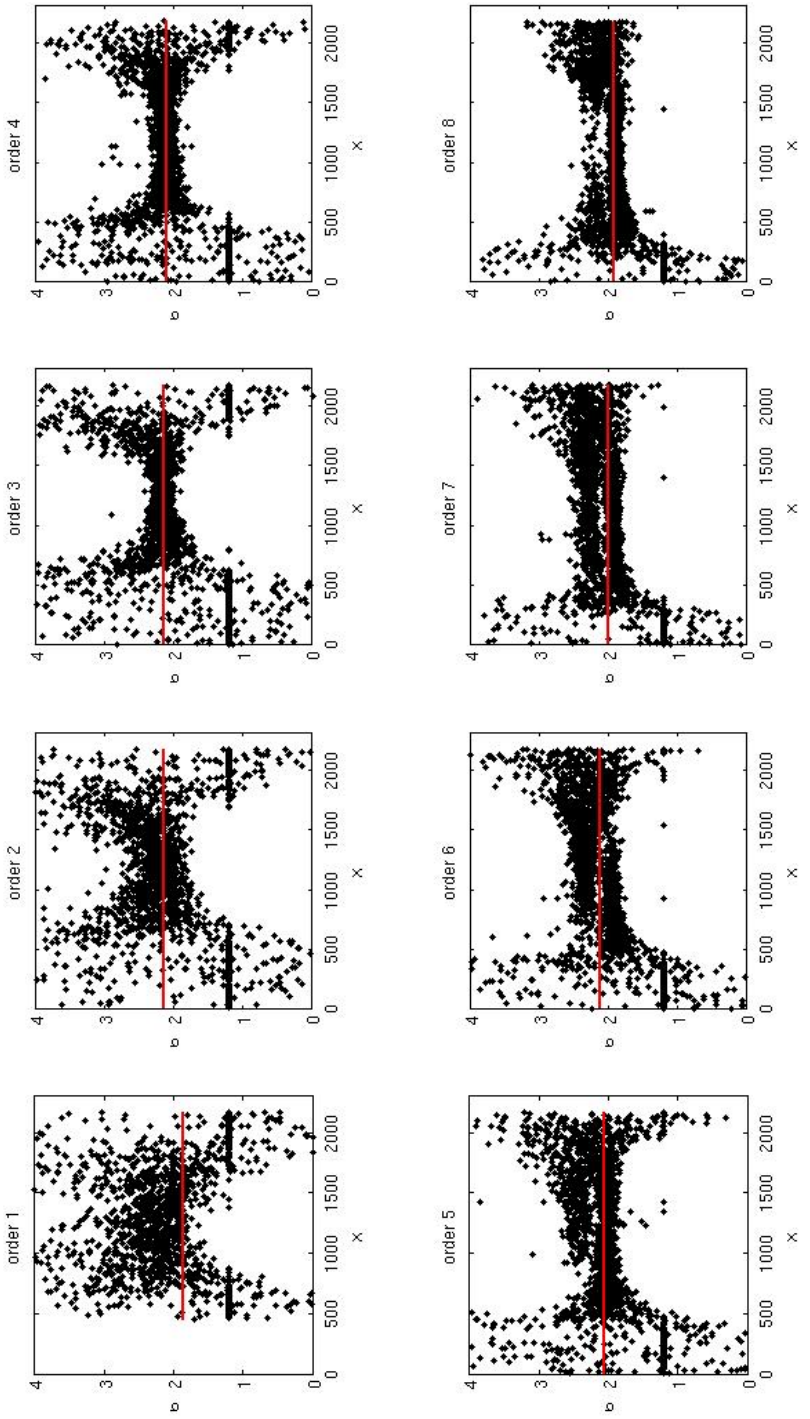

(a)

Figure 3.14: Black points are σ versus position for each order after the first minimization. In red is the fit to each order that in this case correspond to the median. For the second minimization this parameter is fixed to the median value. Orders 1-8. QSO 1355-2257, $slit_{width} = 0.7''$.

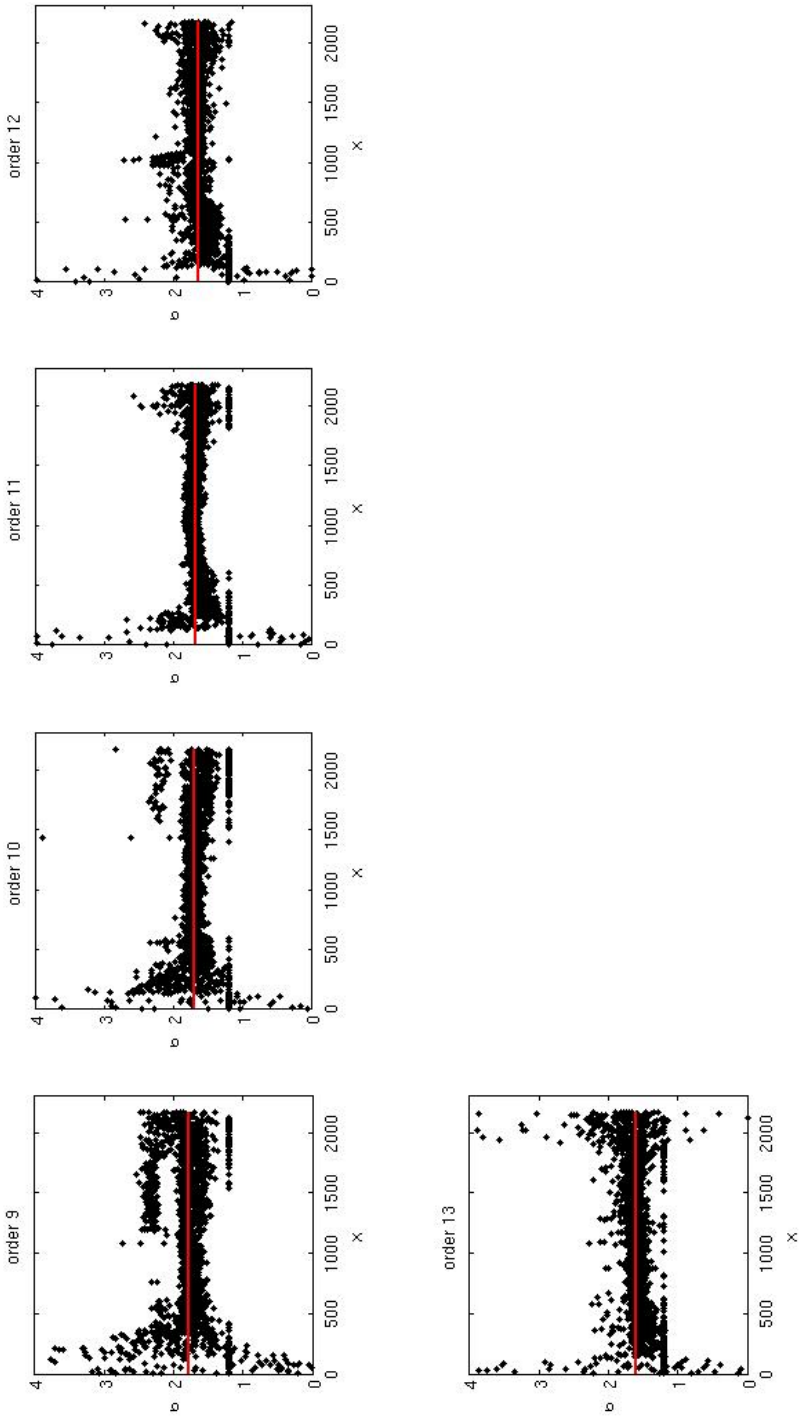

(b)

Figure 3.14: Similar to 3.14a for orders 9-13

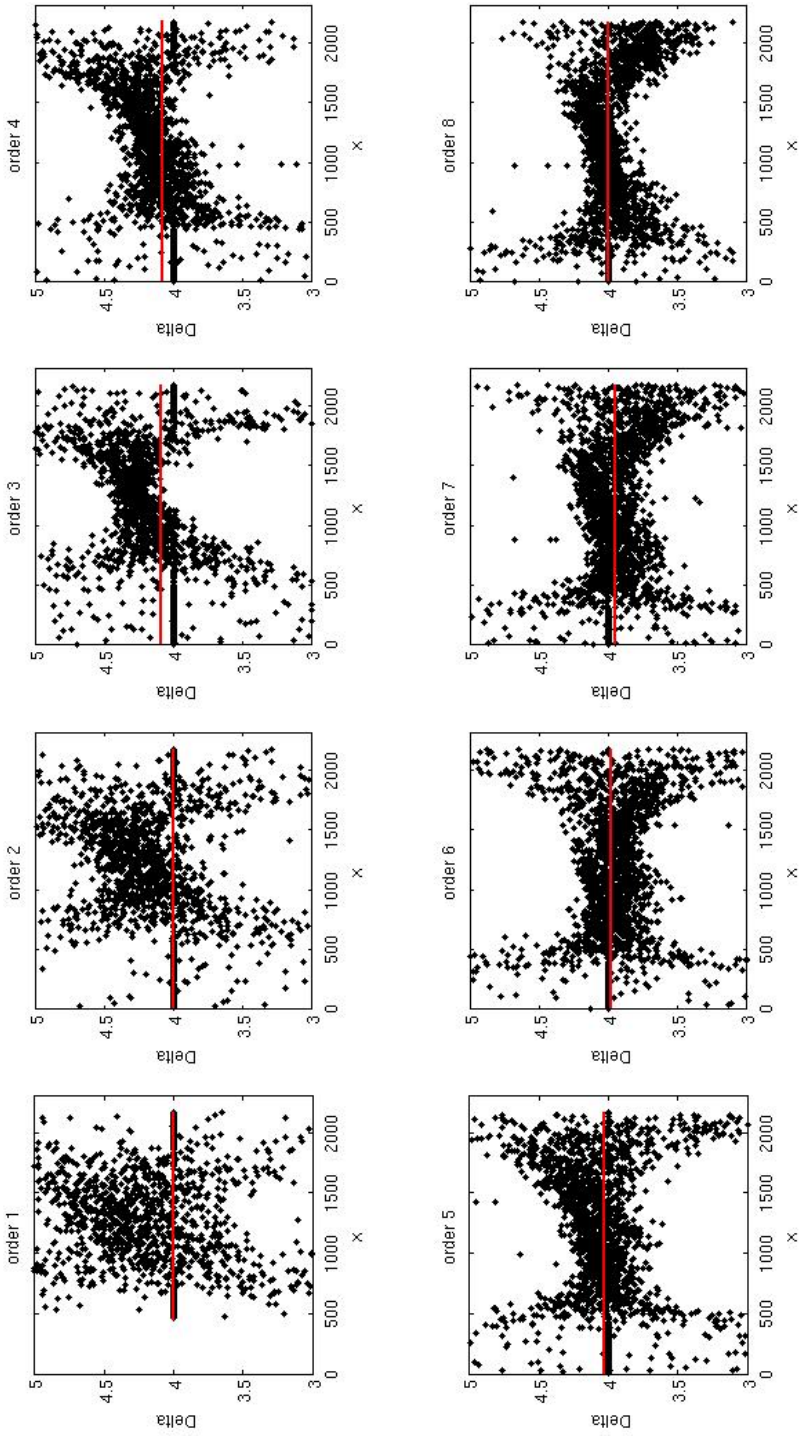

(a)

Figure 3.15: Black points are *delta* versus position for each order after the first minimization. In red is the fit to each order that in this case correspond to the median. For the second minimization this parameter is fixed to the median value. Orders 1-8. QSO 1355-2257, $slit_{width} = 0.7''$.

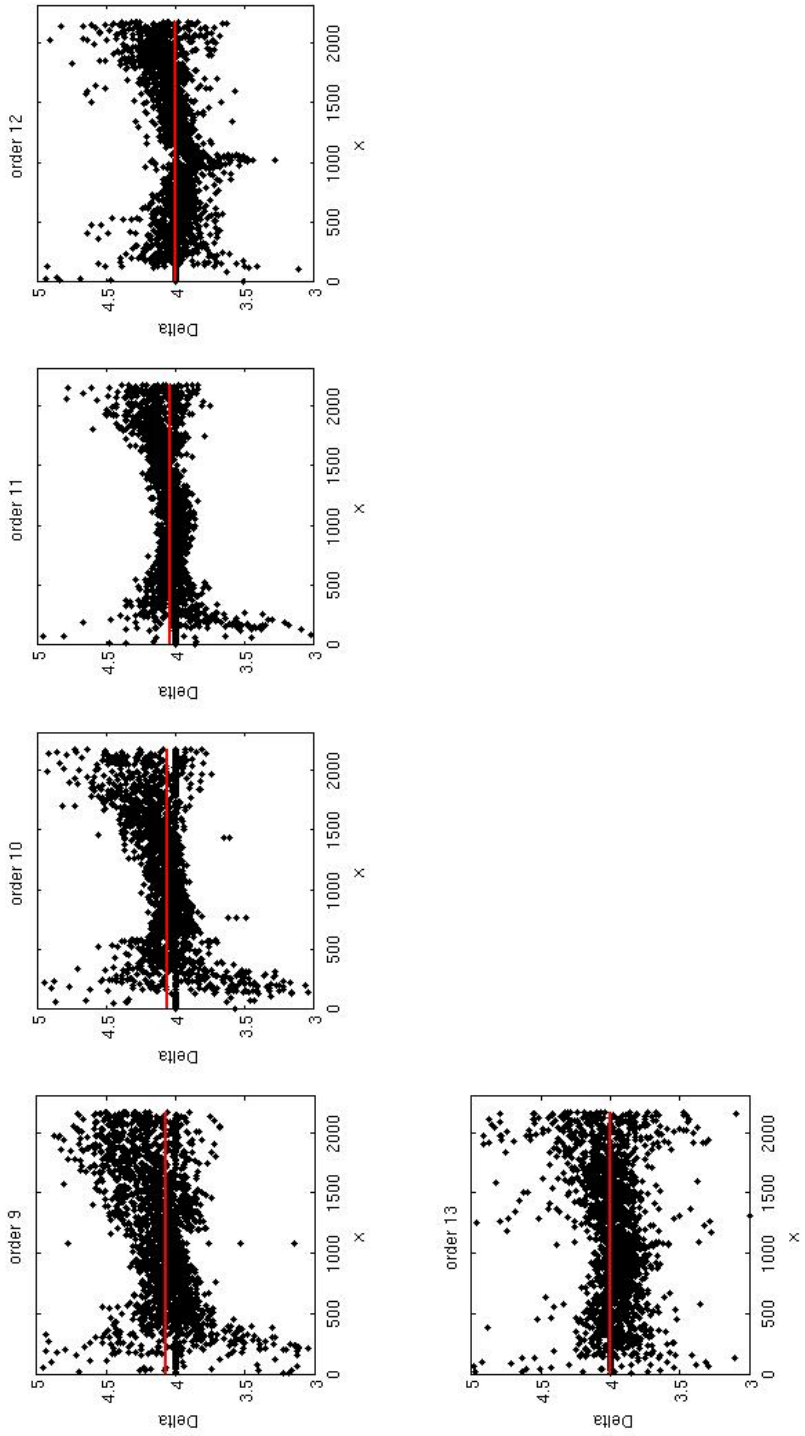

(b)

Figure 3.15: Similar to 3.14a for orders 9-13.

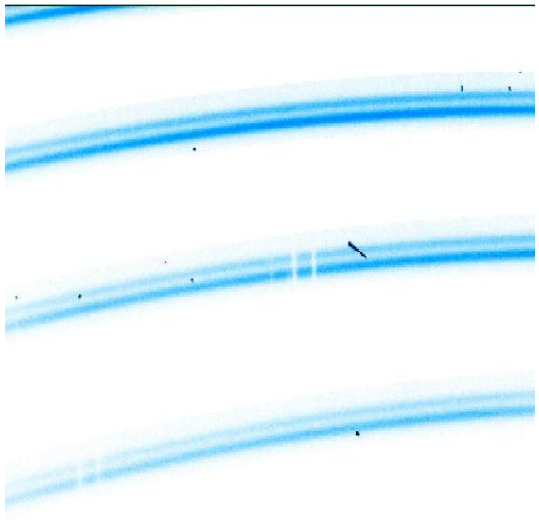

(a) QSO WFI2033-4723 real spec

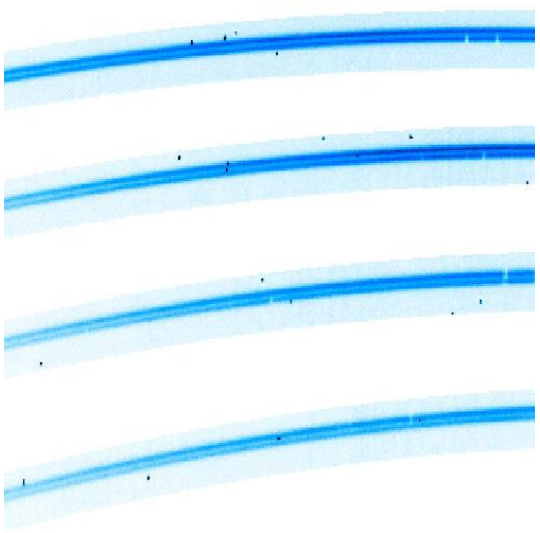

(b) QSO 1355-2257 real spec

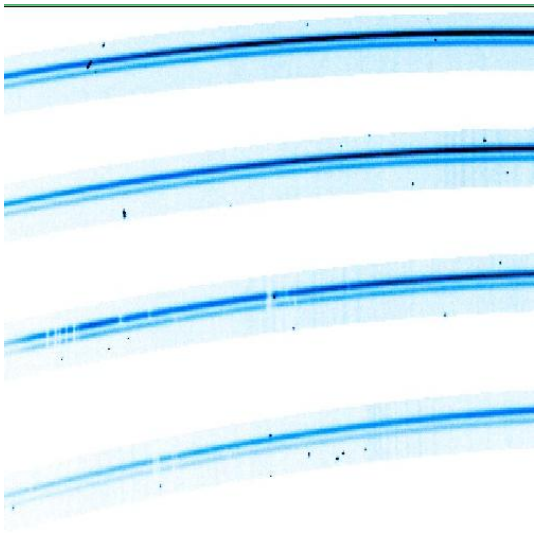

(c) QSO SDSSJ1335+0118 real spec

(d) QSO WFI2033-4723 synthetic spec

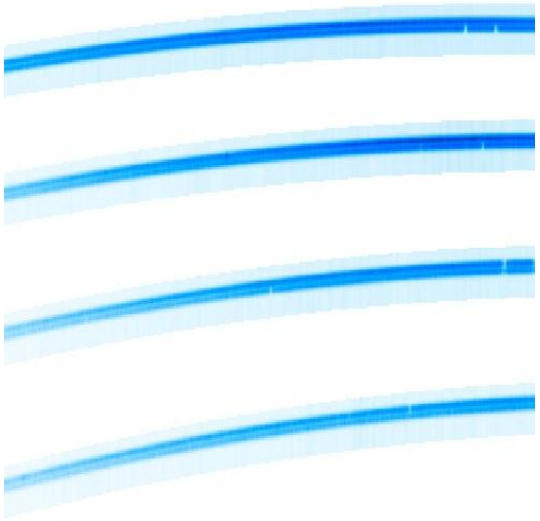

(e) QSO 1355-2257 synthetic spec

(f) QSO SDSSJ1335+0118 synthetic spec

Figure 3.16: Examples of real and synthetic spectra after the second minimization. The images are centered in the same columns that in figure 3.12 and also are shown the same orders. It is observed that the synthetics spectra are almost identical to the real ones, and on the first ones there are not cosmic thanks to the variance computed earlier.

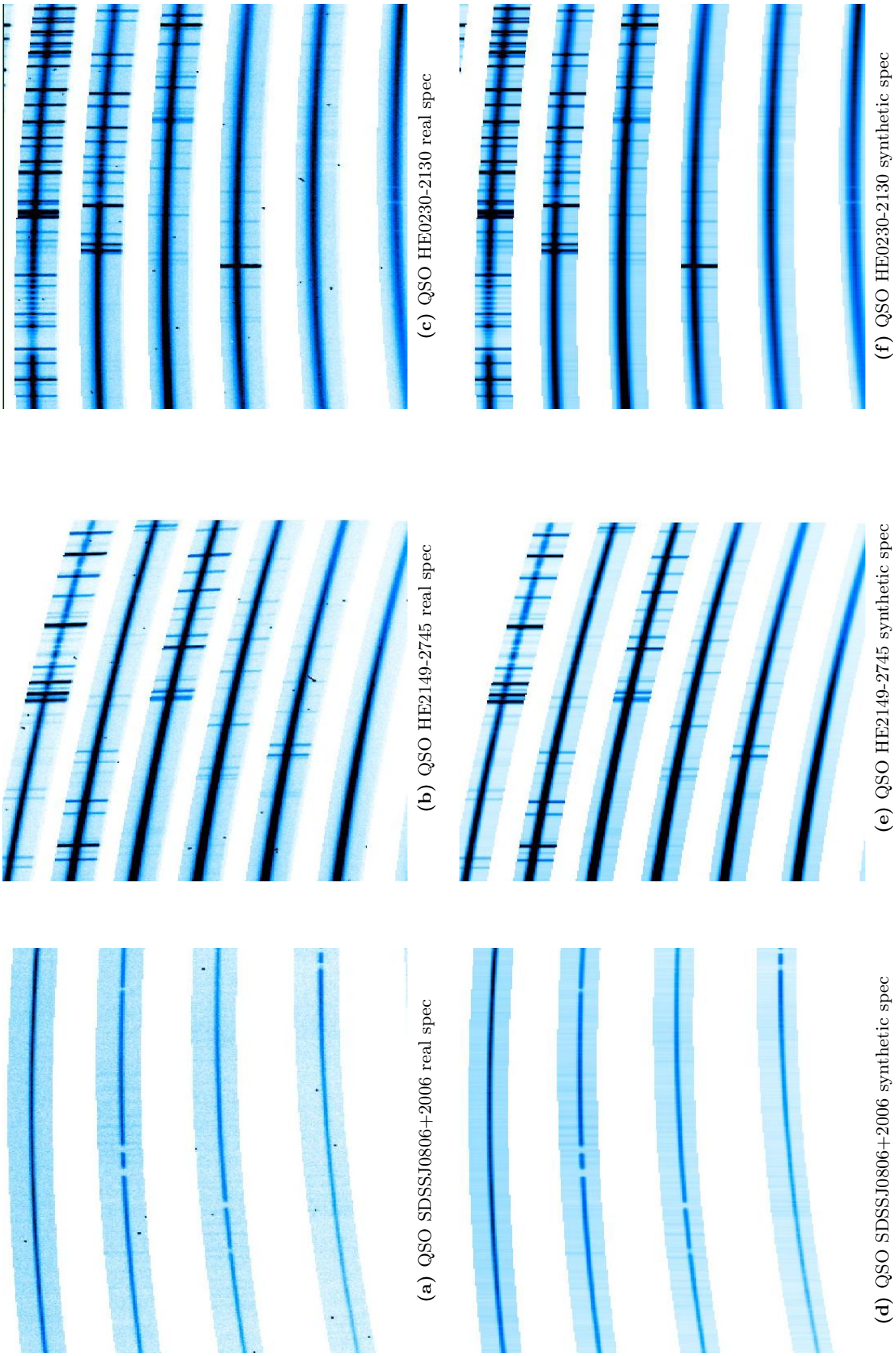

(a) QSO SDSSJ0806+2006 real spec

(b) QSO HE2149-2745 real spec

(c) QSO HE0230-2130 real spec

(d) QSO SDSSJ0806+2006 synthetic spec

(e) QSO HE2149-2745 synthetic spec

(f) QSO HE0230-2130 synthetic spec

Figure 3.17: Same as figure 3.16

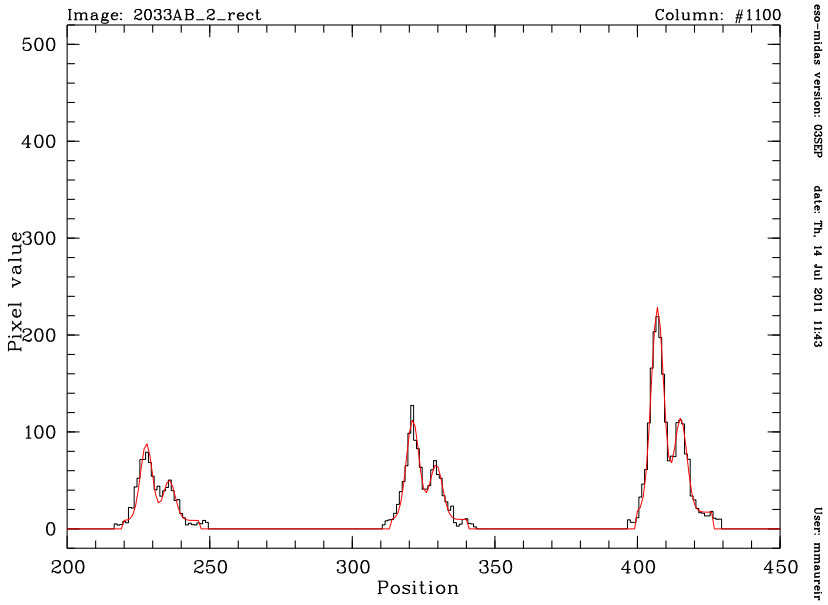

(a) QSO WFI2033-4723. $CCD_{column} = 1100$, $orders = 2, 3, 4$, $slit_{width} = 1''$.

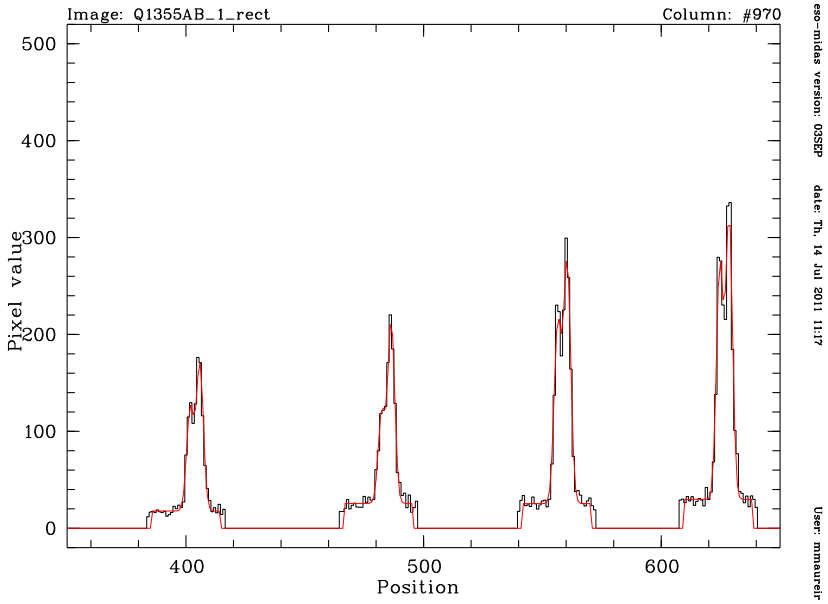

(b) QSO Q1355-2257. $CCD_{column} = 970$, $orders = 4, 5, 6, 7$, $slit_{width} = 0.7''$.

Figure 3.18: Same as in 3.12a and 3.12b but with fitted profiles overlaid. In red the Gaussian and sky respectively after the second minimization. It is observed that both Gaussians are fitted correctly even in 3.18b where an order has an absorption only in one sight of line. Therefore, the extraction accounts for the differences between QSOs even when the two spectra are close.

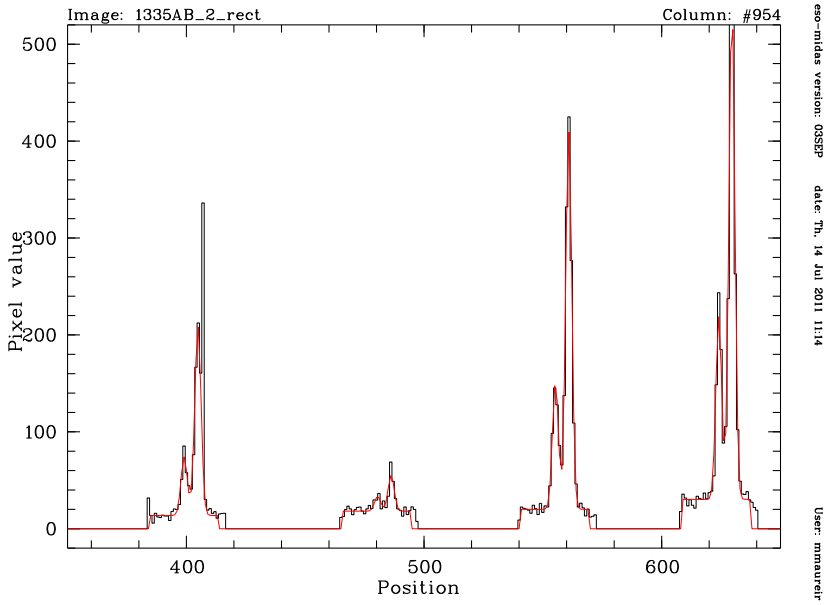

(c) QSO SDSSJ1335+0118. $CCD_{column} = 954$, $orders = 4, 5, 6, 7$, $slit_{width} = 0.7''$.

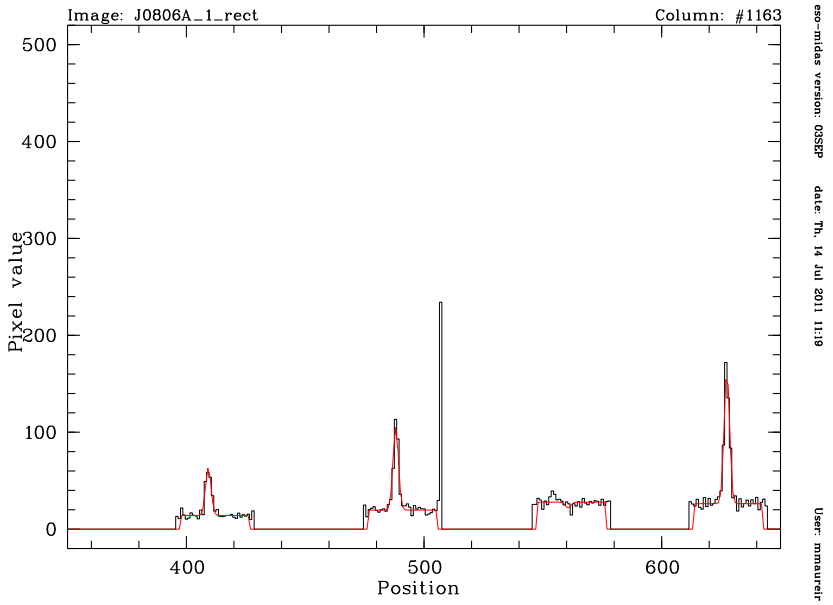

(d) QSO SDSSJ0806+2006. $CCD_{column} = 1163$, $orders = 4, 5, 6, 7$, $slit_{width} = 0.7''$.

Figure 3.18: In black the real profiles shown in 3.12c and 3.12d. In red the Gaussian and constant fits to the continuum of the quasar and sky respectively, after the second minimization.. It is observed that the cosmic in 3.18c is ignored.

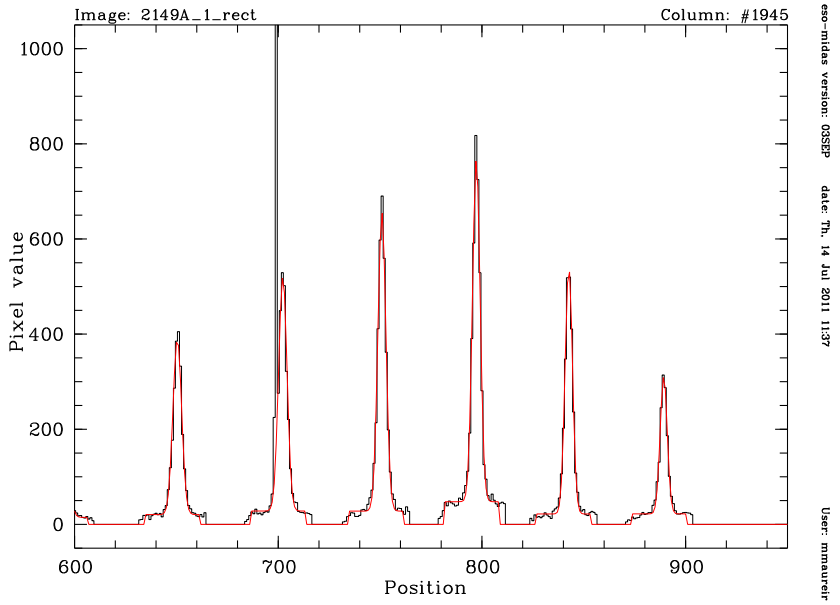

(e) QSO HE2149-2745. $CCD_{column} = 1945$, $orders = 7, 8, 9, 19, 11, 12$, $slit_{width} = 1''$.

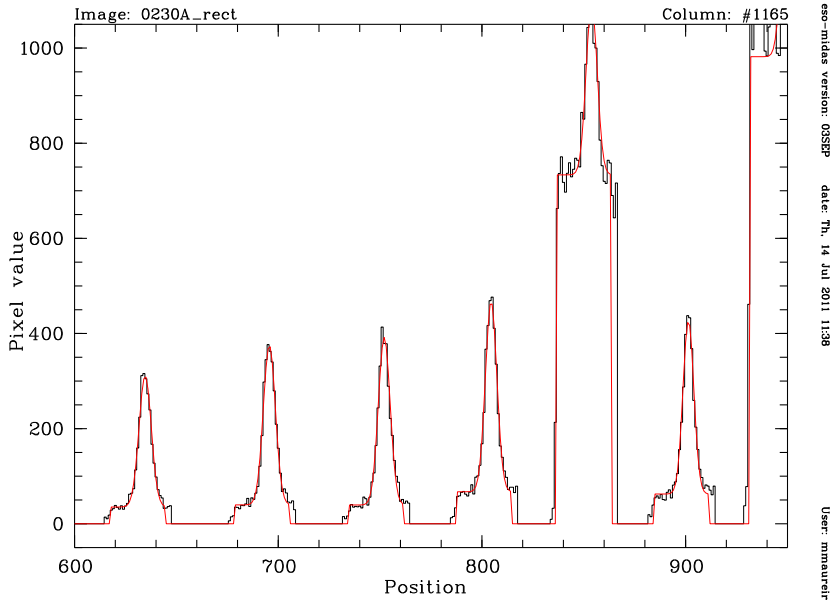

(f) QSO HE0230-2130. $CCD_{column} = 1165$, $orders = 7, 8, 9, 10, 11, 12$, $slit_{width} = 1''$.

Figure 3.18: In black the real profiles shown in 3.12e and 3.12f. In red the gaussian and constant fits to the continuums of the sight of lines and sky respectively, after the second minimization. It is observed that the cosmic in 3.18e is ignored. In 3.18f is seen that the sky line is fitted properly.

index calculated as:

$$n = 1 + 6432.8 \cdot 10^{-8} + \frac{2949810}{146 \cdot 10^8 - 10^{16}/\lambda^2} + \frac{25540}{41 \cdot 10^8 - 10^{16}/\lambda^2}$$

where λ is in Å. To calculate the air refractive index I utilized λ_{air} instead of λ since the difference between using one or the other makes changes in the order of 10^{-8} and 10^{-10} in the third and fourth terms respectively.

I calculated the heliocentric correction using the command COMPUTE/BARYCORR over the vacuum corrected wavelengths.

3.1.7 Adding exposures

For each extraction of the same line of sight, I made a rebinning in order to combine the exposures into a final spectrum. The stacking is calculated as:

$$f_{\lambda_i} = \frac{\sum_{k=1}^{N} \frac{f_{\lambda_i}^k}{{\sigma_{\lambda_i}^k}^2}}{\sum_{k=1}^{N} \frac{1}{{\sigma_{\lambda_i}^k}^2}}$$

where N is the number of exposures of a certain quasar line of sight. This procedure gets rid of possible cosmics in the individul exposures (pixels with high σ).

3.1.8 Continuum normalization

To obtain equivalent widths, the QSOs spectra must be normalized. The continuum normalization is made by adjusting a cubic spline to the flux. The spline is calculated using a median filtered spectrum in each order. The flux values to interpolate are obtained from equispaced points in the wavelength axis. I added or deleted points manually in order to improve the spline fit on absorption lines as well as on the quasar emission lines. Figure 3.19 shows, as an example, the normalization spline for each order of QSO 1355-2257 A and B.

Finally, I merged the normalized orders. In the overlapping regions I combined the orders in the same way as the combination of the different exposures of the same lines of sight.

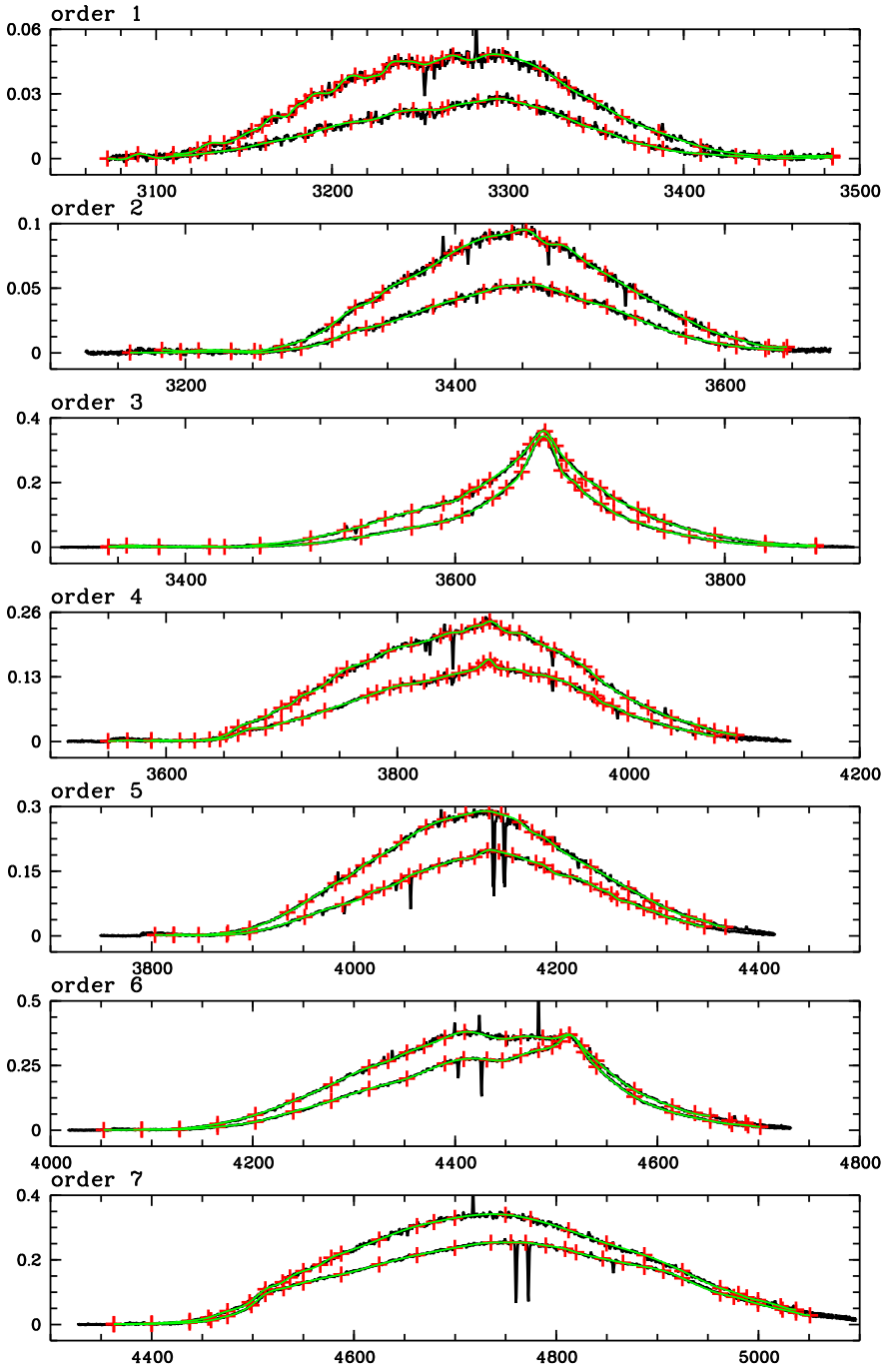

(a)

Figure 3.19: In black the final sum of all exposures of A (brighter) and B line of sight of QSO 1355-2257. In green is shown the spline to the continuums and in red the flux values used to calculate the spline. In order 3, 4, 6 are observed CIV 1559, HeII 1640 and CIII 1909 quasar emission lines respectively. Also in orders 5 and 7 are detected MgII 2796,2803 absorption lines at $\lambda \sim 4140$ and ~ 4770 respectively. The first is seen in both lines of sight while the other is only seen in B.

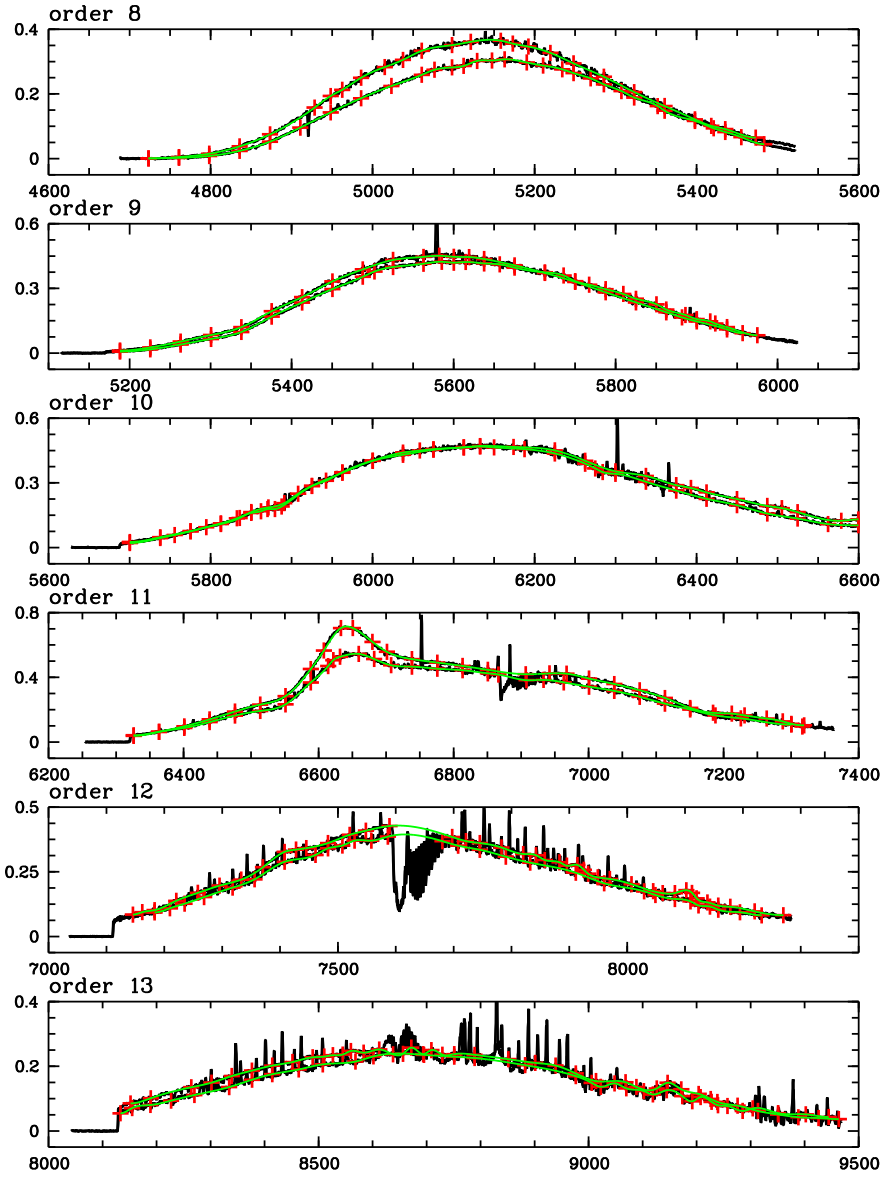

(b)

Figure 3.19: Same as 3.19a. In order 11 is observed the MgII2796 quasar emission line. In orders 11 and 12 are the 6869 and 7605 OII sky absorption lines respectively.

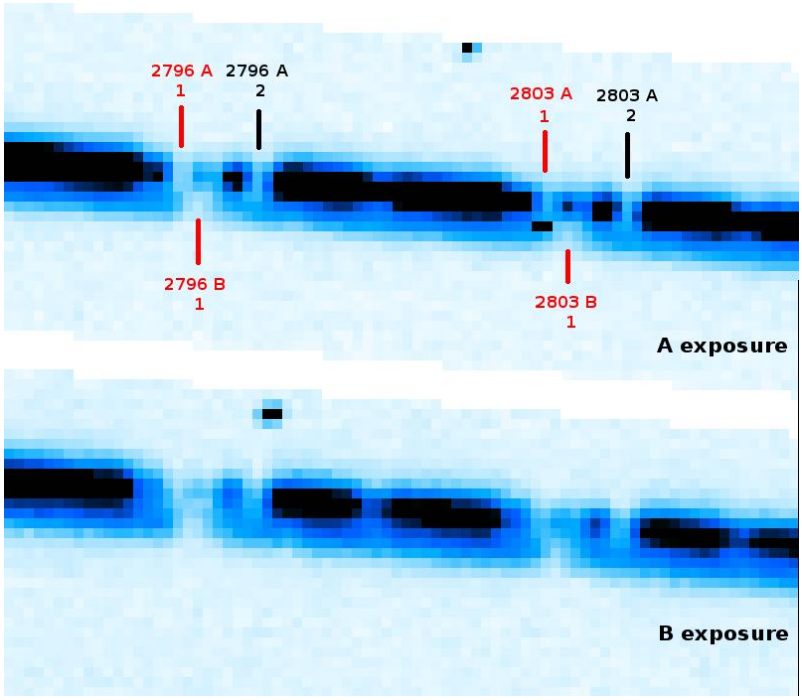

Figure 3.20: Exposure of A and B lines of sight of QSO Q1017-207 at order 9. The A line of sight is the brighter one. The absorption is a MgII system at $z \sim 1.09$ seen in both lines of sight. It has two susbsystems marked as 1 and 2. Subsystem 1 is seen in both lines of sight but with a difference in velocity. Subsystem 2 is only seen in A.

3.2 Special cases

3.2.1 QSO Q1017-207

This lensed quasar is special because it has a small separation of only $0.87''$. Because of this small separation all exposures contain both quasar images. However, despite the close distance between A and B, the extraction procedures allows one to obtain each spectrum with no contamination from the other. As an example of the good extraction, a MgII system found at $z \sim 1.09$ in both sight of lines in Figure 3.20. The Figure shows order 9 of two exposures, one centered in A and the other one in B, in which the absorption is seein. The absorption can be divided in two subsystems that were marked as 1 and 2. Subsystem 1 is seen in both lines of sight but B is redshifted with respect to A. Subsystem 2 is only seen in A. Figure 3.21 is a plot of a column crossing subsystem 2. In red is the synthetic profile of the two Gaussians. It can be observed that Gaussian of A has less amplitude than Gaussian B, thus following the real profile. Therefore, in the 1D spectrum this absorption should appear only in A. Figures 3.22 and 3.23 show the extracted spectra of both lines of sight of these exposures. This confirmes that the extraction is efficient.

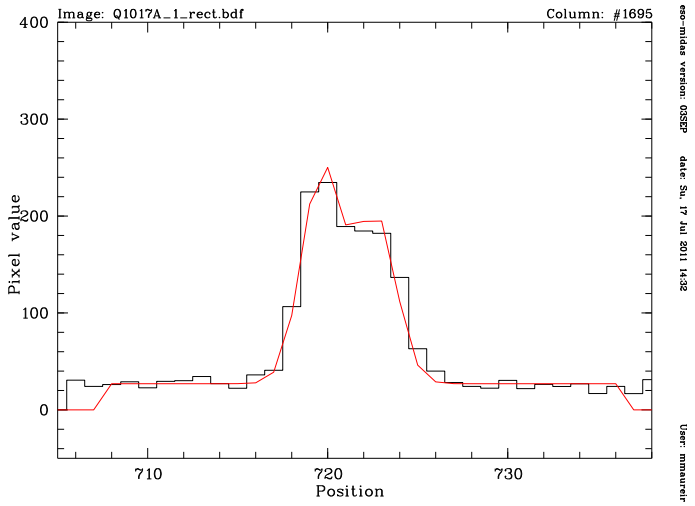

Figure 3.21: Same as 3.20 but showing a column of the exposure of A crossing subsystem 2. In red is the synthetic profile. It can be observed that the gaussian of A has less amplitude than gaussian B, thus following the real profile, despite the small QSO separation.

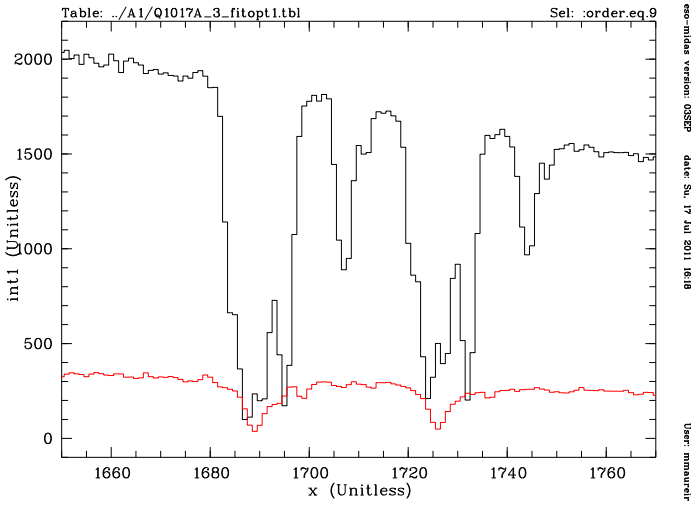

Figure 3.22: Same as 3.20 but showing extracted spectrum of A(black) and B(red) from the A exposure. The y-axis are the values of int_1 and int_2 vs the position in the dispersion direction after the second minimization. It can be observed the differences between the lines of sight as the difference in velocity of subsystem 1 and the non detection in B of subsystem 2.

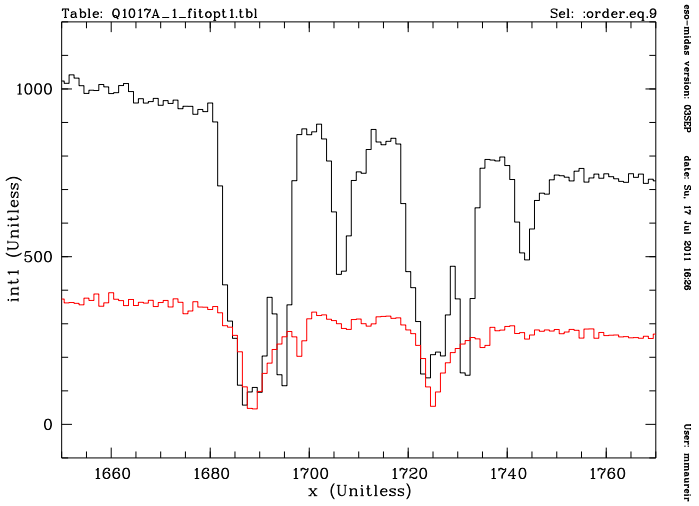

Figure 3.23: Same as 3.22 for exposure of B alone.

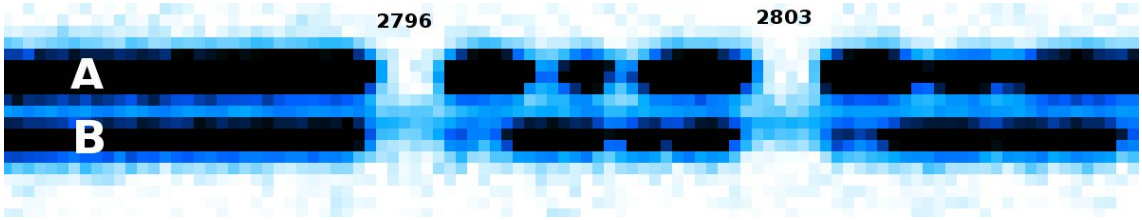

Figure 3.24: Part of an exposure of QSO SDSSJ1335+0118 in which both lines of sight are observed. The sky was subtracted. The absorption is a MgII system at $z \sim 1.42$. In the main component of the system the flux is totally absorbed in A. In B this component should be also totally absorbed, however, there is flux that contaminates B profile, whose position is not the same as the continuum of B.

3.2.2 QSO SDSSJ1335+0118

In this case the lensed quasar has a separation of $1.56''$. Some exposures contain either A or B and others both A and B, when the parallactic angle allowed to have both images on the slit. There is a MgII absorption system at $z \sim 1.42$ on order 11 (Figure 3.24). In the main component of the system the flux is totally absorbed in A, "saturated absorption" . In B this component should be also totally absorbed; however, there is flux that contaminates the B profile, whose position is offset from QSO B.

The most likely explanation for this extra flux is contamination by the continuum of the lens galaxy. Oguri et al. (2004) identified this galaxy in i band and the images (Figure 3.25). In the QSO subtracted image appeared the presence of the lens galaxy is evident. The distances of this extra emission from the QSOs in MagE data is similar to the distance found by Oguri et al. (2004): $1.08''$ and $0.49''$ from A and B, respectively. In addition,

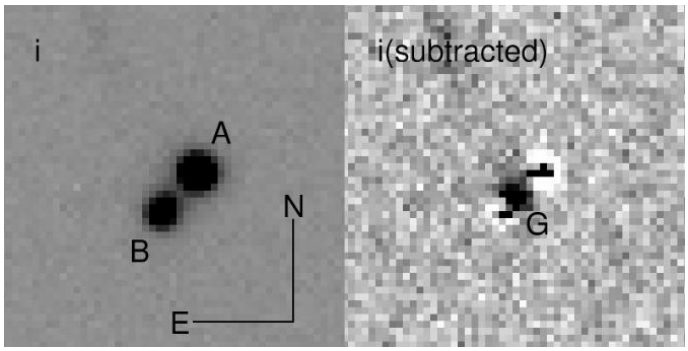

Figure 3.25: Figure 2 from Oguri et al. (2004). Left: A and B of lensed QSO SDSSJ1335+0118. Right: QSOs subtracted image in which the lensing galaxy can be observed.

Eigenbrod et al. (2006) found that the lens is an elliptical galaxy at $z = 0.44$. At this redshift the Balmer break occurs at ~ 5760 Å, which would explain why the extra flux only appears clearly at this absorption, since it is the only one that completely removes the QSO flux at $\lambda > 5760$ Å.

I did several attempts to extract the galaxy spectrum, but all were unsuccesful. In the end, It was not possible to remove this contamination from B spectrum. Consequently, in the final B spectrum, the MgII absorption at $z \sim 1.42$ do not reach zero as in A. See figure 3.26.

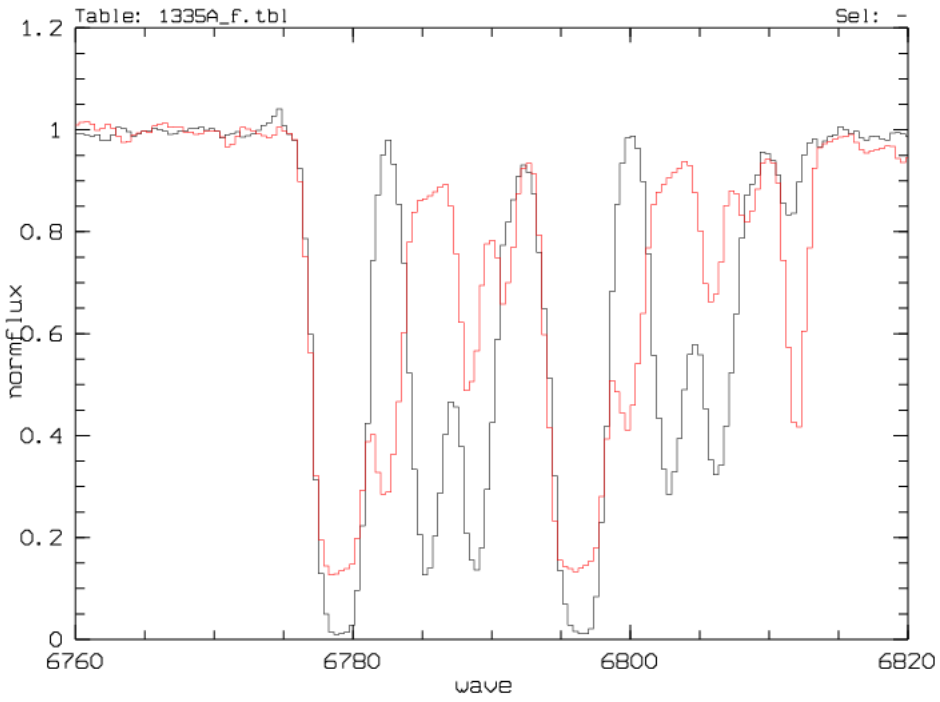

Figure 3.26: MgII absorption system at $z \sim 1.42$. In black(red) is the final spectrum of A(B) after normalization. Note the additional flux at the bottom of the B lines, which is due to the lensing galaxy (and not due to bad sky subtraction).

Chapter 4

MgII absorption systems sample

In this chapter I describe the MgII sample and its properties.

4.1 Redshift Path

The redshift path Δz of a line of sight is defined as the length of the redshift interval in which it is possible to find an absorption system by a certain transition. In a survey the sum of Δz over all lines of sight gives the total redshift path. However, the detectability of a line depends on S/N and resolution. It varies along a line of sight and also between lines of sight due to differences in S/N and resolution. In order to account for these differences, the redshift path is redefined as the range in redshift in which it is possible to detect an absorption, whose equivalent width is greater than a given threshold.

For N lines of sight the redshift path *density* is given by

$$g(W_{min}, z) = \sum_{n=1}^{N} H(z - z_n^{min}) H(z_n^{max} - z) H(W_{min} - S \cdot w^{min}(z)) \tag{4.1}$$

where H is the Heaviside step function. W_{min} is the equivalent width threshold, z_n^{min} and z_n^{max} are the minimum and maximum redshifts to search absorptions in LOS n, and S is the detection significance level. The value of z^{min} is defined as the maximum between

$$z = \frac{\lambda_{min}}{\lambda_0} - 1$$

and

$$z = \frac{\lambda_{Ly\alpha}}{\lambda_0} - 1$$

where $\lambda_0 = 2796.354$ and λ_{min} is the smallest wavelength in the spectrum. Accordingly, z^{max} is the minimum between

$$z = \frac{\lambda_{max}}{\lambda_0} - 1$$

and

$$z = ((\frac{\lambda_{MgII}}{\lambda_0} - 1)(c - \frac{v}{2}) - v)/(c + \frac{v}{2})$$

where the last equation correspond to a z at $v = 5000$ km/s of the MgII 2796 quasar emission line. λ_{max} is the greatest wavelength in the spectrum. The minimum equivalent width that can be detected at redshift z, $w^{min}(z)$, is calculated as

$$w_{min}(z) = \frac{FWHM(z)}{< S/N(z) >} \frac{1}{(1+z)} \tag{4.2}$$

where $< S/N(z) >$ is the average signal to noise over a line and FWHM the resolution in Å. Thus, $g(W_{min}, z)$ is the number of lines of sight in which an absorption at redshift z and with $W_r > W_{min}$ can be detected at the $S \cdot \sigma$ significance level. Integrating over z, Δz is obtained for a given W_{min}.

In this work I calculated the total redshift path for several W_{min} values using all quasar sample and both lines of sight. Figure 4.1 shows the total redshift path for different W_{min} values and figure 4.2 shows the redshift path density vs. redshift for $W_{min} = 1.00$, 0.30 and 0.05 Å.

Using Δz it can be calculated the number of system per unit redshift as

$$\sum_n \frac{1}{\Delta z(W_n)}$$

where the sum is over all the systems and $\Delta z(W_n)$ is the redshift path for the equivalent width of system n.

4.2 Transverse distance between the lines of sight

I used following equation from (Smette et al. 1992, and references therein) for calculating the proper distance between lines of sight at the absorber redshift, $S(z_{abs})$:

$$S(z_{abs}) = \begin{cases} \frac{\theta \cdot D_{as} D_{ol}}{D_{ls}} \cdot \frac{1+z_l}{1+z_{abs}} & z_{abs} > z_l \\ \theta \cdot D_{oa} & z_{abs} < z_l, \end{cases} \tag{4.3}$$

where, θ is the angular separation of the images from the observer point of view, D_{as} is the angular diameter distance from the absorber to the source (a quasar in this case),

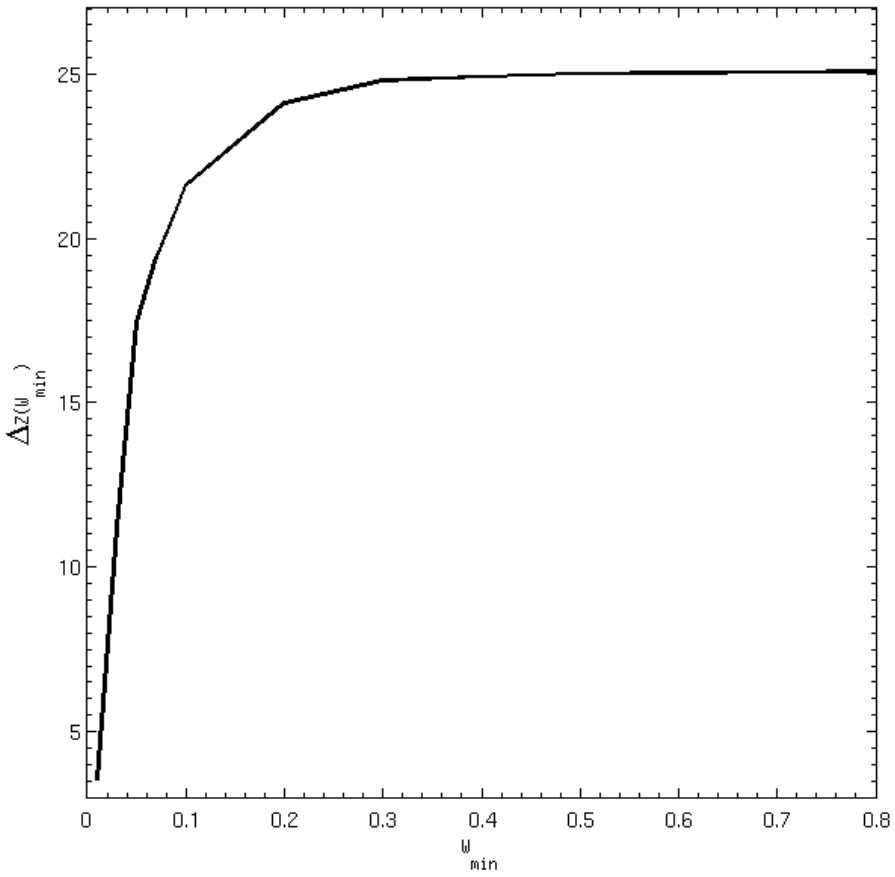

Figure 4.1: Total redshift path Δz as a function of W_{min}. For $W_{min} = 0.3$ Å the redshift path is 99% complete, and for $W_{min} = 0.05$ Å only complete to 70%.

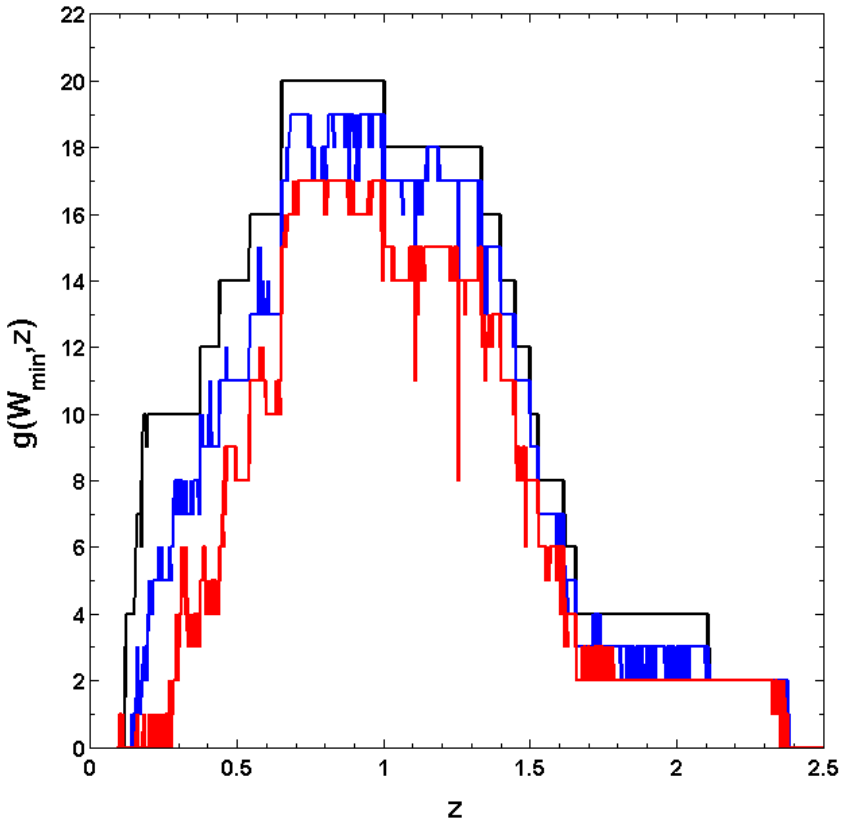

Figure 4.2: Density redshift path for three values of W_{min}: 1 Å (black), 0.3 Å (blue) and 0.05 Å (red).

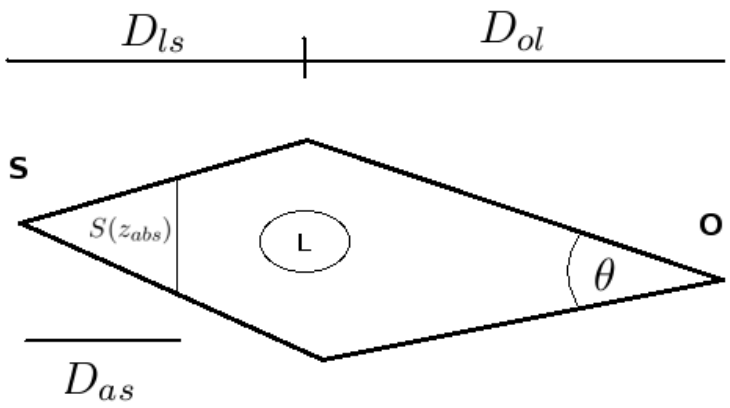

Figure 4.3: Geometry of a lens system.

D_{ol} the angular diameter distance from the observer to the lens, D_{ls} the angular diameter distance from the lens to the source, D_{oa} the angular diameter distance from the observer to the absorber, z_l the lens redshift and z_{abs} the absorber redshift. See figure 4.3.

Angular diameter distances were calculated as in Hogg (1999). The cosmological parameters used were $\Omega_k = 0$, $\Omega_m = 0.3$, $\Omega_\Lambda = 0.7$ (flat universe, accelerated universe).

4.3 The Sample

For each line of sight I made a search for MgII 2796,2803 systems by eye using velocity plots of the two transitions. The criteria to detect an absorption was that the significance of the equivalent width measure of its 2796 component was equal to or greater than 3. This sample will be called Calan sample.

I found a total of 28 systems in the Calan sample. Half of them are observed in both lines of sight and have a difference in velocity of less than 600 km/s. From now on these systems will be called coincidences. Consequently, systems observed in just one LOS will be called anticoincidences.

The range of separations between the lines of sight at the absorption redshifts is 0.29-23 kpc with an average of $\sim$ 11 kpc. The mean redshift is $\sim$0.9. I calculated the rest frame equivalent width of the 2796 component using pixel integration. I defined the limits of integration as where the flux in the first and last absorption line is recovered.

Figures 4.4 to 4.12 show the absorption profiles in velocity space. In case FeII and MgI were detected, they are also displayed.

Table 4.1 summarizes the redshifts and $Wr(2796)$ for A and B LOS, and the distances between the LOS at the absorption redshift. In case there is no absorption detected in one line of sight I give a 3σ upper limit for the $W_r(2796)$.

Some caveats

I did not find any MgII absorption system in QSO HE0230-2130. The expectation, according to dN/dz from the literature (Nestor et al. 2005, Narayanan et al. 2007) and the redshift path calculated for these specific lines of sight, is that I should have found at least one strong system and one weak system with $W_r > 0.1$ Å. So, the non detection is consistent with poisson uncertainty. However, these expectations are calculated on the basis of lines of sight that not necessarily cross a galaxy. In the case of gravitationally lensed quasars, we know that the lines of sight are at close distance from the lens galaxy and therefore, we expect to observe at least one absorption in these LOS with more probability than in common individual LOS.

I found an absorption at the redshift of the lens galaxy in most of quasars in the sample. The only two exception were quasar SDSSJ1335+0118 and, as mentioned before, quasar HE0230-2130. I give the corresponding upper limits in Table 6.1 of chapter 6 in which I refer to the systems associated with the lens in more detail.

For all MgII systems except 3 cases (Q1017 $z = 1.0859$, J1335 $z = 1.424$ and HE0512 $z = 0.9311$), the profiles in A and B expand for less than 500 km/s. In the three cases with larger Δv I divided the total range of velocity into two systems. I made this decision because velocity ranges greater than 700 km/s are hardly produced in just one galaxy. Instead, they are more probably associated with a galaxy satellite pair or a group. Also, in the literature the distribution of MgII equivalent width $n(W)$ and the number of systems per unit redshift (dN/dz) are calculated using $\Delta v < 500$ km/s (Nestor et al. 2005). I followed this definition in my work. For Q1017 at $z = 1.0859$ and HE0512 at $z = 0.9311$ each absorption in A and B is in a window of 500 km/s after the split, but for J1335 at $z = 1.424$ one of the separated absorption has a velocity range of ∼700 km/s. I decided not to divide further because of the complex kinematics and also because the profile of one of the components, at 400 km/s, is consistent with an outflow (Bond et al. 2001, Nestor et al. 2011). If that were the case, the broad absorption at 0 km/s that is also strong in MgI, unlike the absorption at 400 km/s, could represent the disk of a galaxy from where the outflow is being expelled. In addition CIV $\lambda 1548, 1550$ is detected at the velocity of the possible outflow, which also reinforce the idea that this absorption is produced in a different environment that the one at 0 km/s but not necessarily in a different galaxy. Figure 4.13 shows the MgII $\lambda 2796, 2803$ and CIV $\lambda 1548, 1550$ for both lines of sight.

Figure 4.14 shows the splitted profiles in velocity.

4.4 Sample analysis

Some statistics of the Calan sample are the following:

Number of systems per unit redshift

I calculated dN/dz considering A and B lines independently. For strong systems I obtained $dN/dz = 0.9 \pm 0.6$. Although the error is large, the value is consistent with $dN/dz = 0.78 \pm 0.03$ given by Nestor et al. (2005). For weak systems I obtained $dN/dz = 1.3 \pm 0.1$ also consistent with $dN/dz = 1.4 \pm 0.1$, the average value for the same redshift range given by Narayanan et al. (2007). In conclusion, there is no bias in the sample regarding number counts.

Equivalent Width distribution

Figure 4.15 shows the equivalent width distribution for all the systems in A and B. The solid blue and red lines are the exponential fits to the weak and strong systems given by Nestor et al. (2005). The dashed blue line is the power law fit for the weak population given by Churchill et al. (1999). For both populations the distribution is consistent with the literature. Weak population is more consistent with a power law than an exponential. Last bin of strong systems shows an inconsistency with the overall distribution. However, this bin is composed of the two systems in QSO J1335 at $z = 1.424$ which span more than 600 km/s, which is larger than the velocity window of 500 km/s imposed by Nestor et al. (2005). In conclusion, there is no bias in the equivalent width distribution of the Calan sample.

4.5 Systems from the literature

In order to increase the sample I have considered MgII absorption systems toward gravitationally lensed quasars from the literature. This sample will be called Literature sample. The Literature sample is summarized in Table 4.2. I have used eight absorptions observed in at least one of the three lines of sight of the triply imaged QSO APM08279 5255 from Ellison et al. (2004); two systems seen in at least one of three lines of sight of the quadruple gravitationally lensed quasar Q2237+0305 from Rauch et al. (2002) and sixteen systems of the quadruple lensed quasar SDSS J1004+4112, the triply imaged quasar SDSS

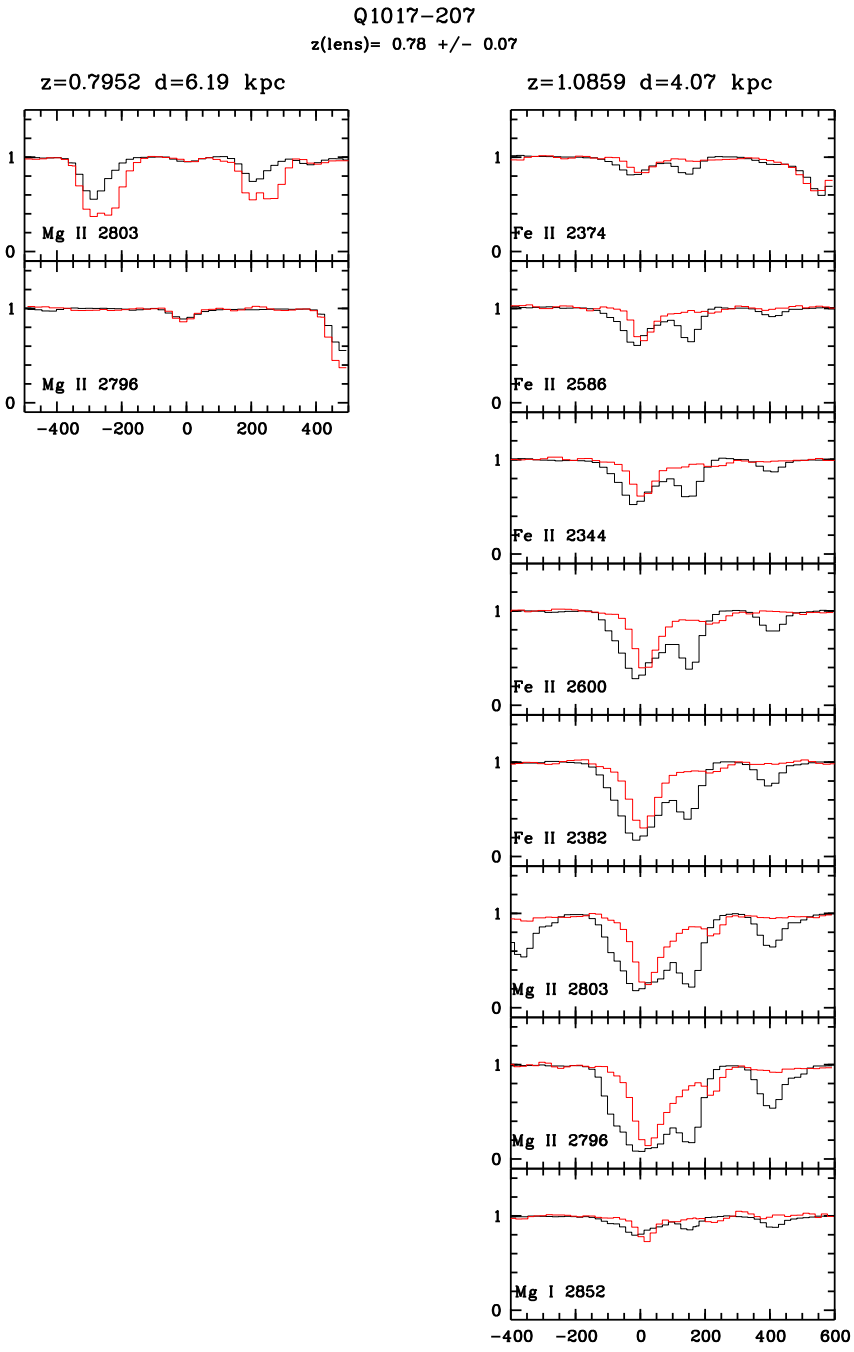

Figure 4.4: MgII absorptions systems in QSO 1017-207. Spectrum of QSO A is in black and that of QSO B is in red.

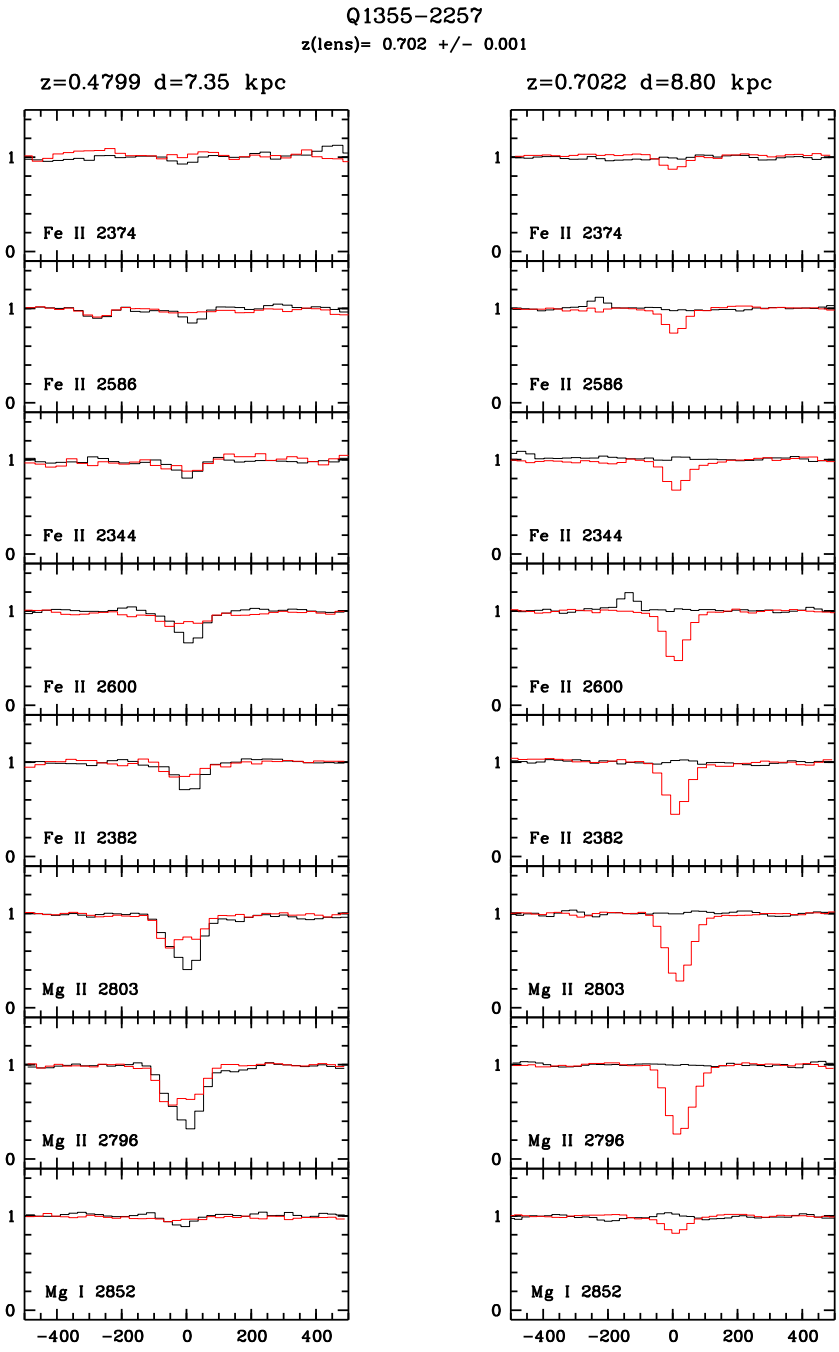

Figure 4.5: MgII absorptions systems in QSO 1355-2257. Spectrum of QSO A is in black and that of QSO B is in red.

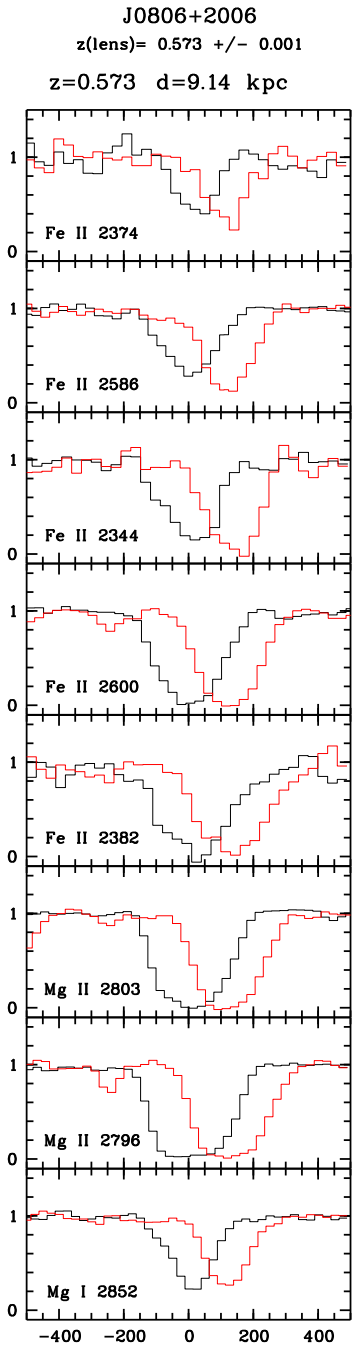

Figure 4.6: MgII absorptions systems in QSO J0806+2006. Spectrum of QSO A is in black and that of QSO B is in red.

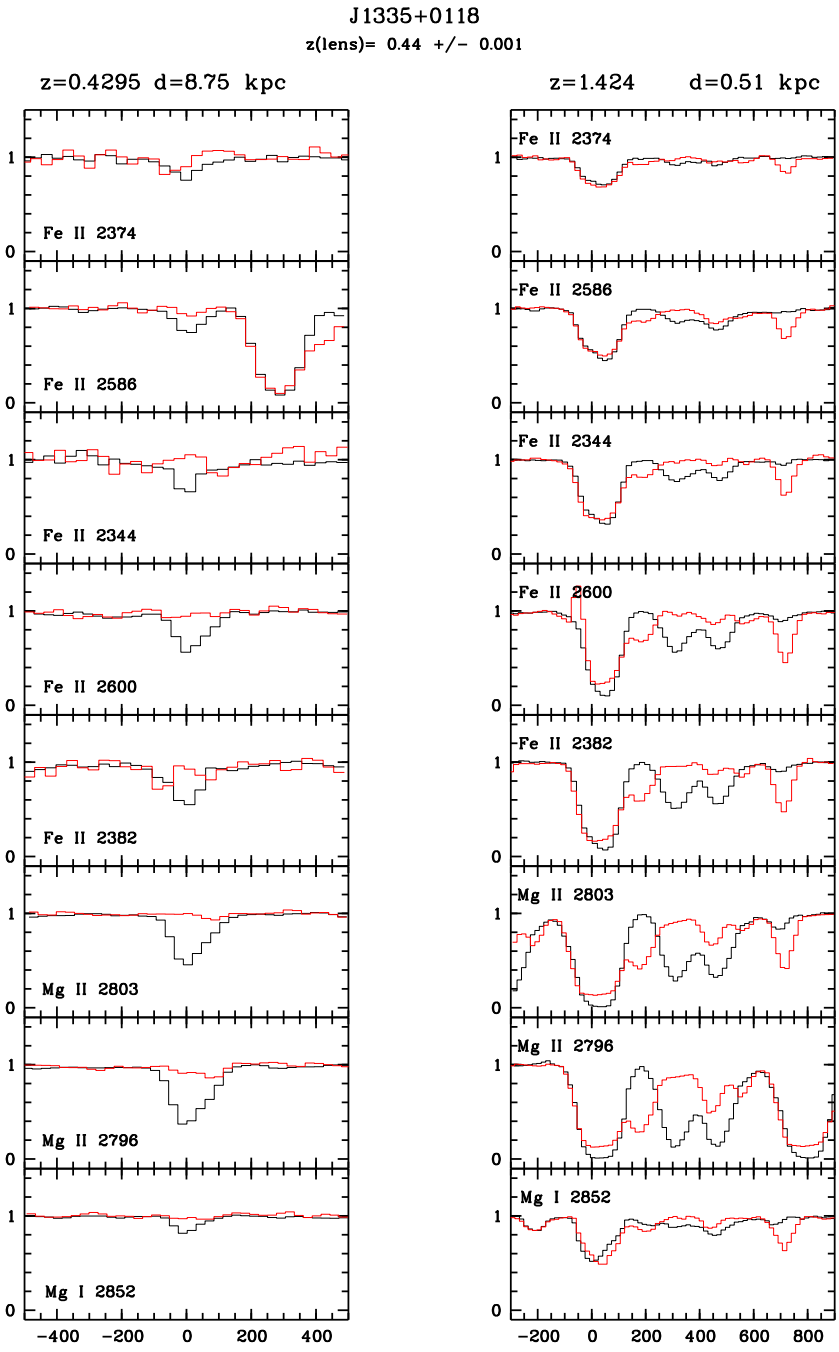

Figure 4.7: MgII absorptions systems in QSO J1335+0118. Spectrum of QSO A is in black and that of QSO B is in red.

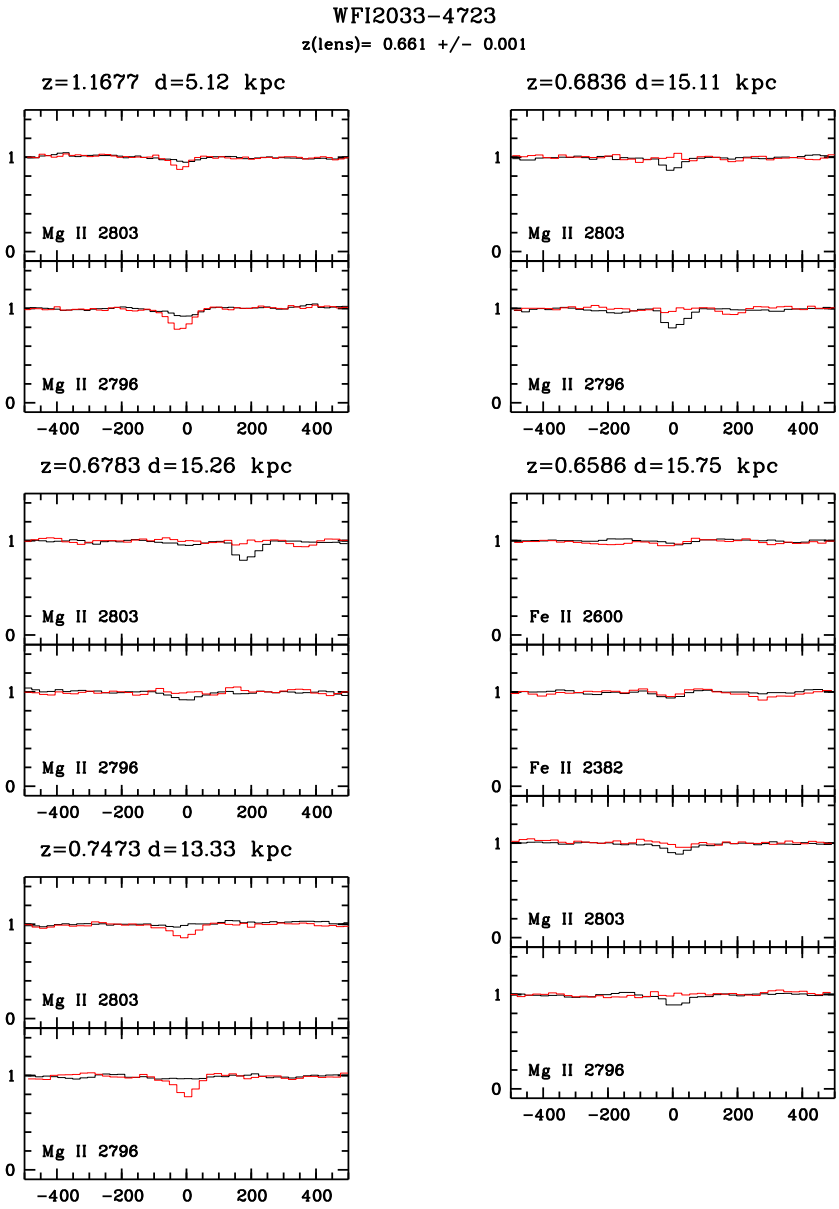

Figure 4.8: MgII absorptions systems in QSO WFI2033-4723. Spectrum of QSO A is in black and that of QSO B is in red.

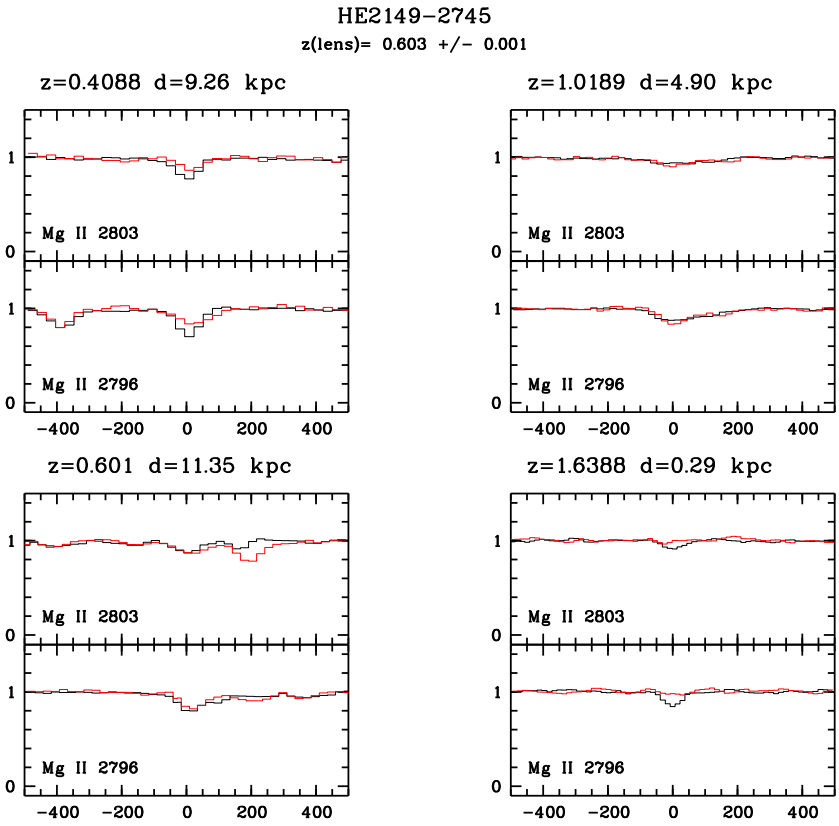

Figure 4.9: MgII absorptions systems in QSO HE2149-2745. Spectrum of QSO A is in black and that of QSO B is in red.

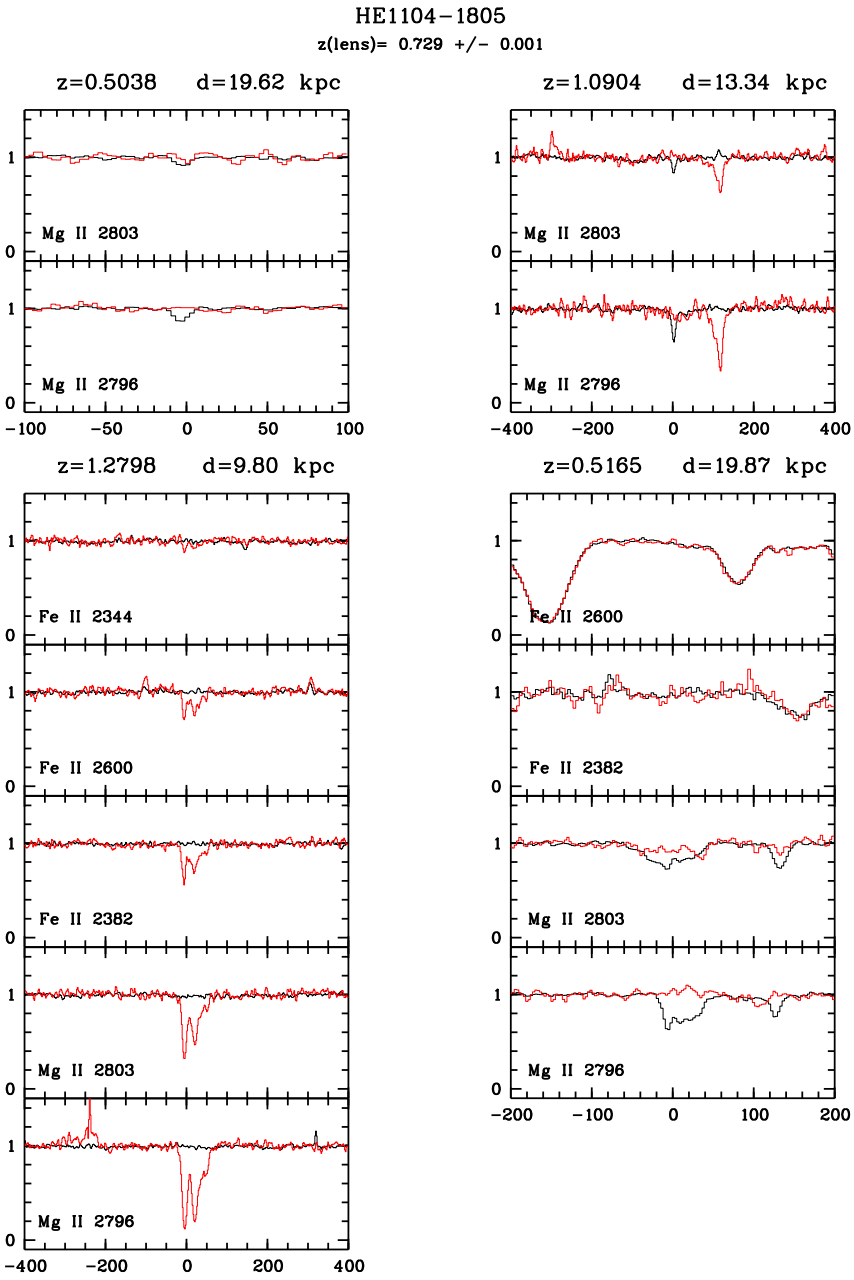
HE1104−1805
z(lens)= 0.729 +/− 0.001
z=0.5038 d=19.62 kpc
Mg II 2803
Mg II 2796
z=1.0904 d=13.34 kpc
Mg II 2803
Mg II 2796
z=1.2798 d=9.80 kpc
Fe II 2344
Fe II 2600
Fe II 2382
Mg II 2803
Mg II 2796
z=0.5165 d=19.87 kpc
Fe II 2600
Fe II 2382
Mg II 2803
Mg II 2796

(a)

Figure 4.10

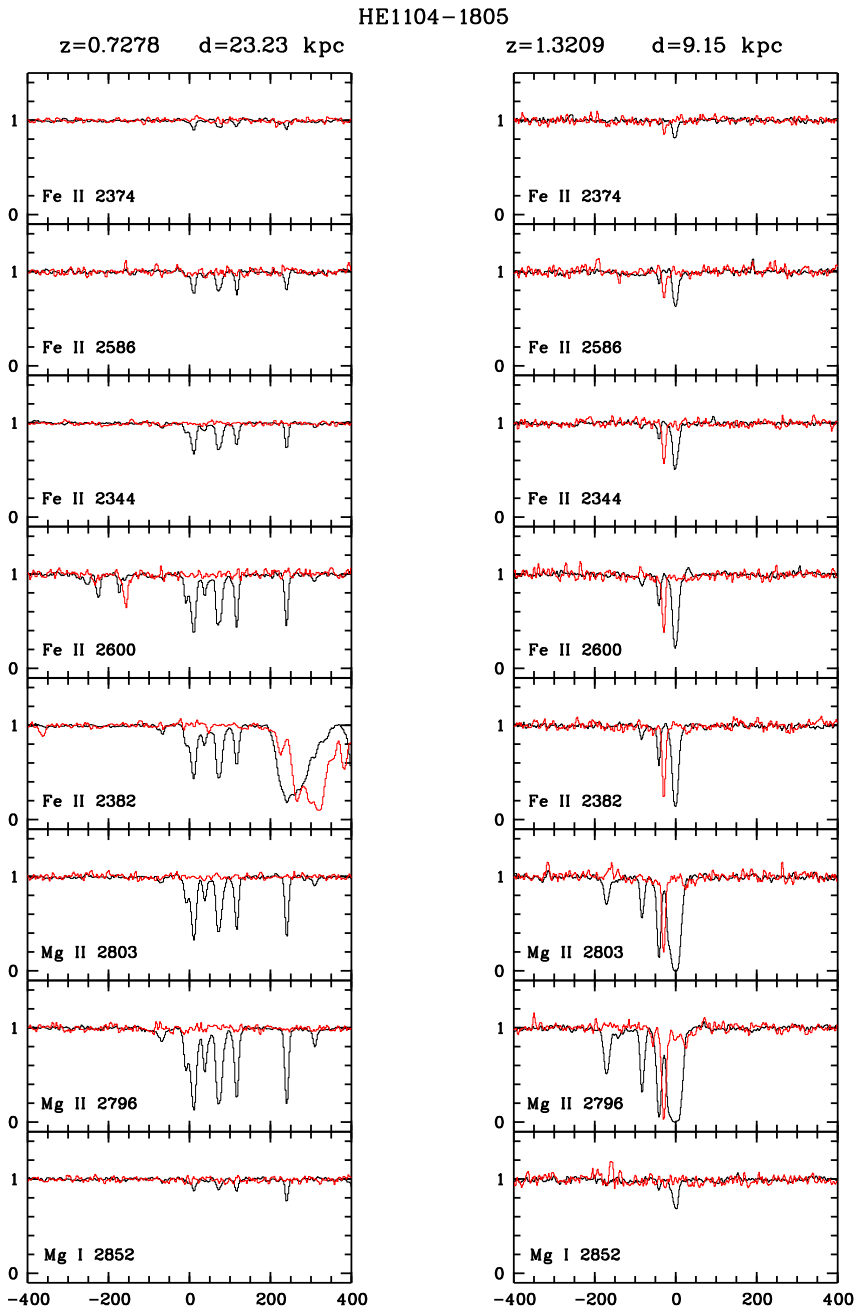

(b)

Figure 4.10: MgII absorptions systems in QSO HE1104-1805. Spectrum of QSO A is in black and that of QSO B is in red.

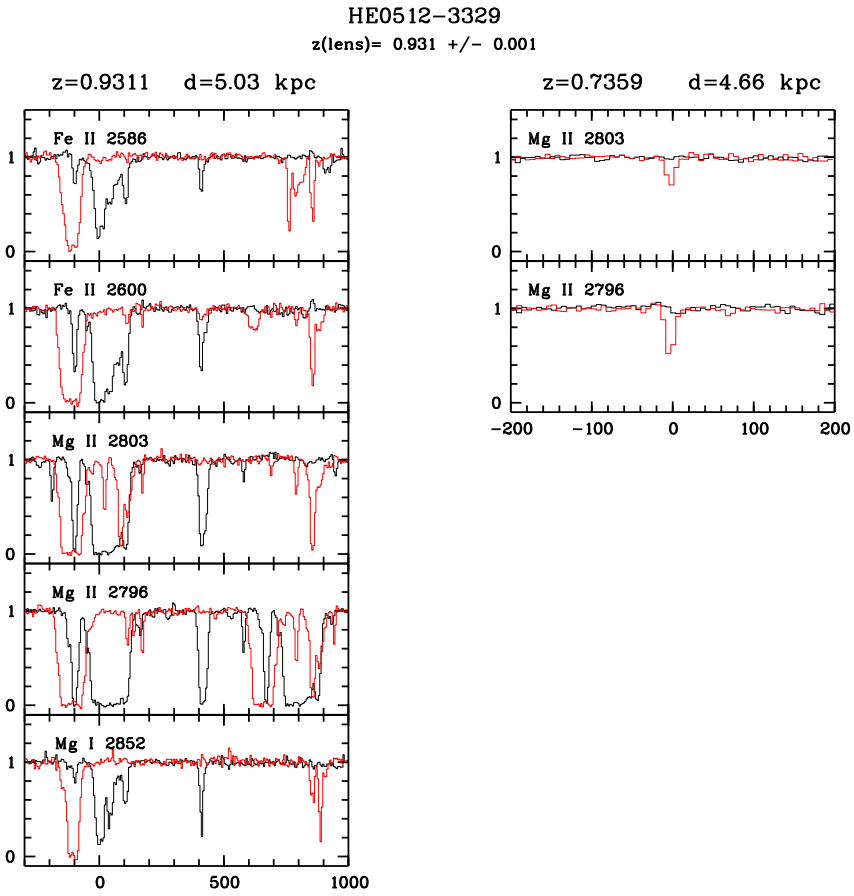

Figure 4.11: MgII absorptions systems in QSO HE0512-3329. Spectrum of QSO A is in black and that of QSO B is in red.

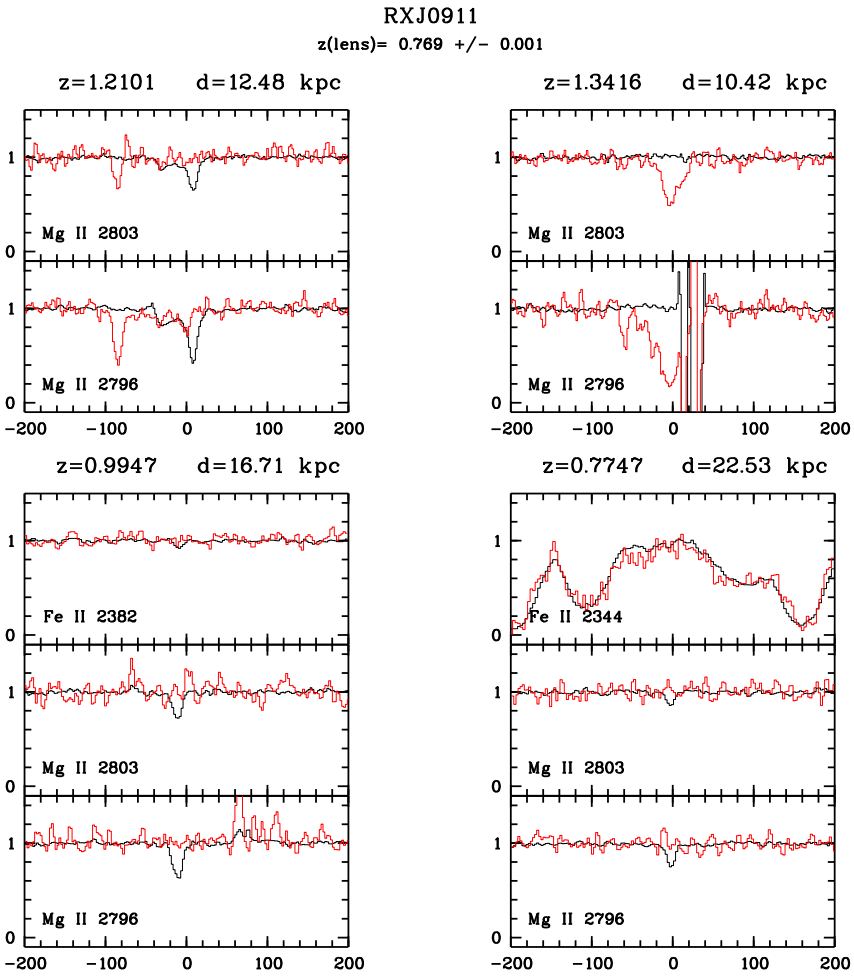

Figure 4.12: MgII absorptions systems in QSO RXJ0911. Spectrum of QSO A is in black and that of QSO B is in red.

Table 4.1: MgII absorption systems. Calan sample.

QSO	z^A_{abs}	$W^A_r(2796)$ [Å]	z^B_{abs}	$W^B_r(2796)$ [Å]	Dist(A-B) $[h^{-1}_{70}\mathrm{kpc}]$
Q1017	0.7952^L	0.10±0.01	0.7953	0.09±0.01	6.19
	1.0859	2.23± 0.01	1.0861	1.29± 0.02	4.07
	1.0887	0.42± 0.01	...	<0.08	4.06
Q1355	0.4799	0.75 ± 0.02	0.4797	0.55±0.02	7.35
	...	<0.06	0.7022^L	0.62± 0.02	8.80
J0806	0.5730^L	2.41±0.04	0.5736	2.37±0.06	9.14
J1335	0.4295	0.78±0.01	0.4299	0.15±0.02	8.75
	1.4240	3.62 ± 0.01	0.4243	2.96 ± 0.01	0.51
	1.4296	0.26 ± 0.02	1.4298	0.80 ± 0.02	0.49
WFI2033	0.6586^L	0.10±0.01	...	<0.09	15.75
	0.6783	0.07± 0.01	...	<0.09	15.26
	0.6836	0.14± 0.01	...	<0.07	15.11
	...	<0.05	0.7473	0.15± 0.02	13.33
	1.1677	0.08± 0.01	1.1676	0.16± 0.01	5.12
HE2149	0.4088	0.21± 0.02	0.4089	0.19±0.03	9.26
	0.6010^L	0.25± 0.01	0.6011	0.27± 0.02	11.35
	1.0189	0.23± 0.01	1.0189	0.22± 0.01	4.90
	1.6388	0.09± 0.01	...	<0.07	0.29
HE1104	0.5038	0.013±0.002	...	<0.006	19.62
	0.5165	0.193± 0.003	...	<0.007	19.87
	0.7278^L	0.674±0.003	...	<0.007	23.23
	1.0904	0.058± 0.001	1.0912	0.134± 0.001	13.34
	...	<0.004	1.2798	0.338± 0.003	9.80
	1.3209	0.732± 0.002	1.3207	0.196±0.004	9.15
HE0512	...	<0.005	0.7359	0.053± 0.001	4.66
	0.9311^L	1.934 ±0.003	0.9304	1.233 ±0.004	5.03
	0.9338	0.428 ±0.003	0.9366	0.411± 0.007	4.99
RXJ0911	0.7747^L	0.035±0.002	...	<0.050	22.534
	0.9947	0.048± 0.002	...	<0.060	16.708
	1.2102	0.125± 0.002	1.2095	0.084± 0.007	12.476
	...	<0.014	1.3416	0.259± 0.034	10.416

^{L} Redshift similar to the lens galaxy.

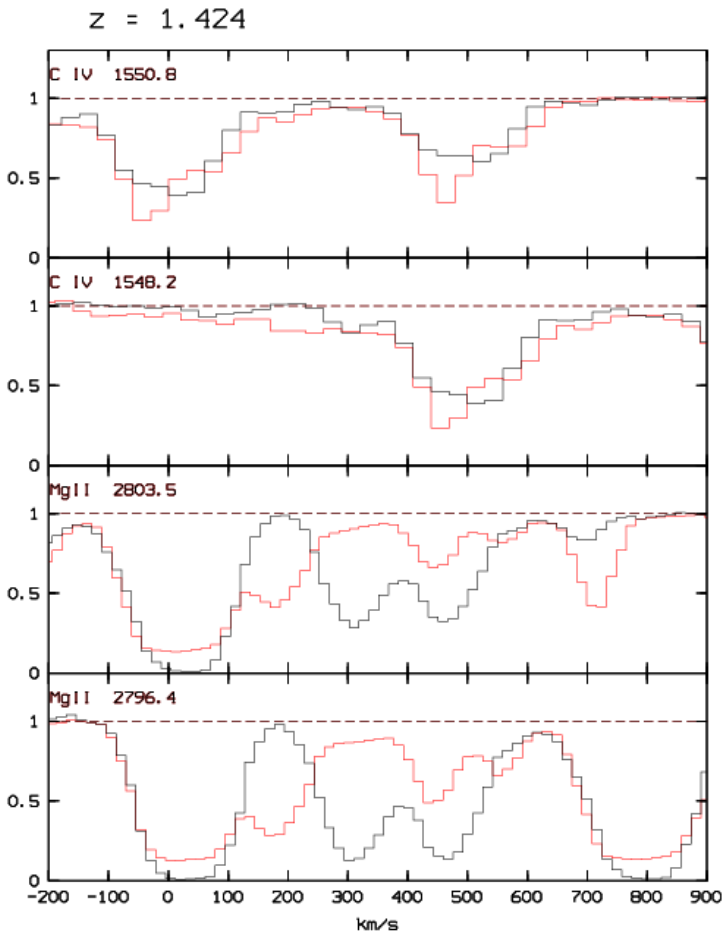

Figure 4.13: QSO J335+0118. Absorption system at $z = 1.4240$. Lines of sight A and B are in black and red respectively. There is a CIV absorption at velocity consistent with the absorption at ~ 400 km/s.

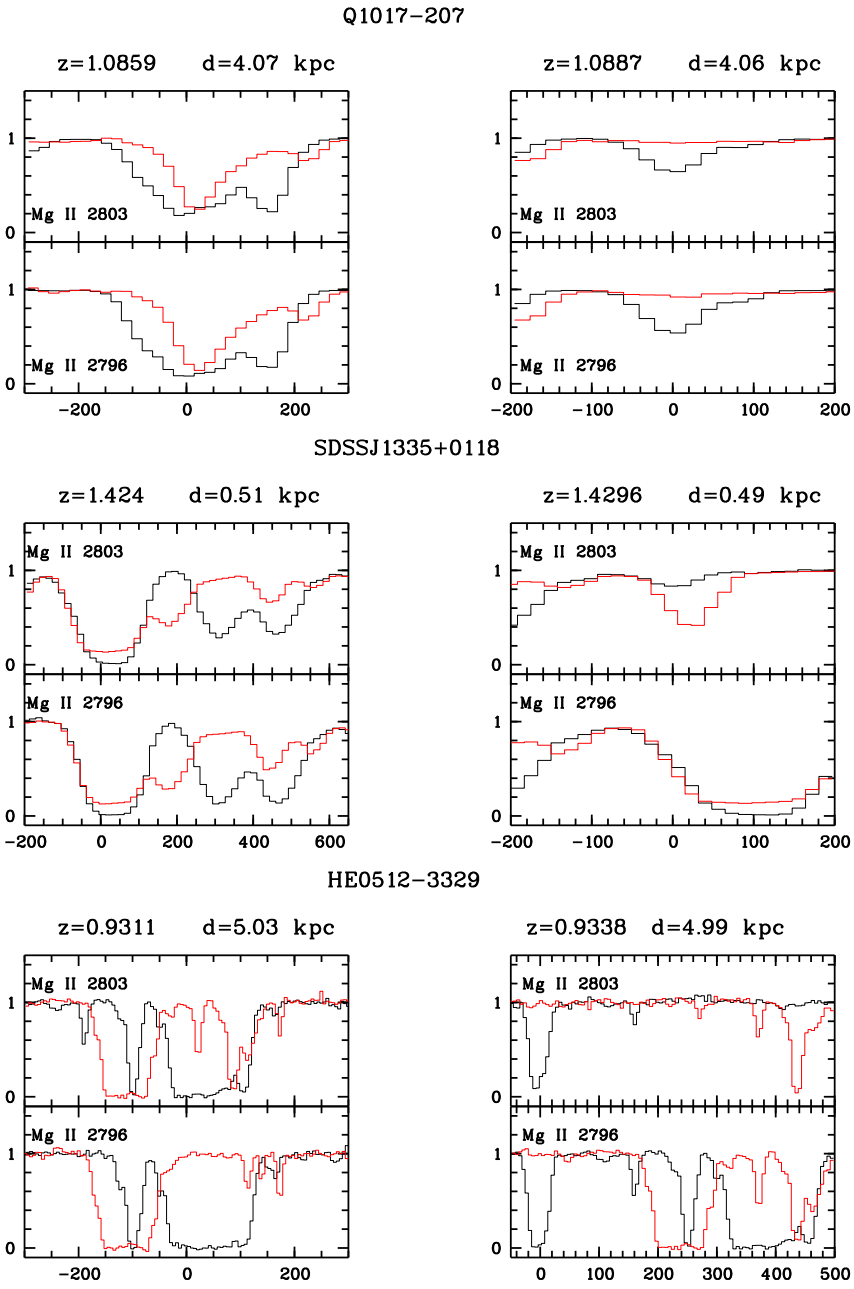

Figure 4.14: The two absorption after the split of the systems in the three cases that the velocity width of the absorption expand for more than 700 km/s.

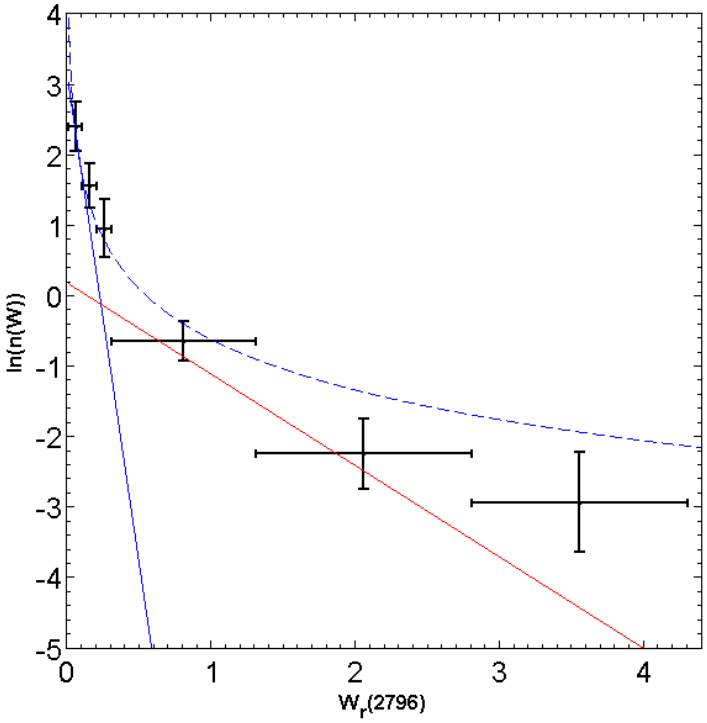

Figure 4.15: Equivalent width distribution for all systems in A and B. Blue solid line is the exponential function for weak systems given by Nestor et al. (2005). Dashed blue line is the power law fit for the weak systems given by Churchill et al. (1999). The red line is the exponential function for strong systems given also by Nestor et al. (2005).

Table 4.2: Literature sample

QSO	N[a]	Transverse distances[b] $[h_{70}^{-1}$ kpc]	Reference
APM08279+5255 A B C	26	0.4-2.5	*Ellison et al. (2004)*
Q2237+0305 A B C	4	0.3-0.5	*Rauch et al. (2002)*
SDSS J1004+4112 A B C D	26	4-101	*Rogerson (2011)*
SDSS J1029+2623 B C	3	0.8-10	*Rogerson (2011)*
SDSS J0904+1512 A B	3	0.1-0.5	*Rogerson (2011)*
SDSS 1054+273 A B	1	1.9	*Rogerson (2011)*
HE1104-1805 A B	1	4.8	*Smette et al. (1995)*

[a]Number of absorptions seen in at least one of two lines of sight. In case the lens system has more than two lines of sight, I considered all the combinations of two LOS. See text.
[b]Range of transverse distances at z_{abs}

J1029+2623 (the paper only have two lines of sight), and the two imaged quasar SDSS J0904+1512 and SDSS 1054+273 from Rogerson (2011). Finally, I have also added one system from Smette et al. (1995) in the LOS to HE1104-1805, which is not covered by my UVES spectra.

The merge of the Calan sample and Literature sample will be called full sample. Considering the full sample the transverse distances range from 0.13 to 100 h_{70}^{-1} kpc.

Note on triply lensed QSOs

In case the lens system has more than two lines of sight, I considered all the combinations of two LOS in the sample. For example if a system is detected in two of three LOS it is added to the sample as two anticoincidences and one coincidence (at the corresponding LOS separations).

4.6 Transverse distances

Figure 4.16 shows the normalized histogram of transverse distances between lines of sight for systems observed in both lines of sight A and B, and for those systems only seen in one line of sight for all the systems in the full sample. It is observed that at transverse separations less than 14 kpc the coincidences dominate over the anticoincidences. On the other hand, for transverse separations greater than 14 kpc the systems are only anticoincidences except in one case. This cut could represent a crude estimation on the sizes on these systems; however, this must to take it with caution because the upper limits for the

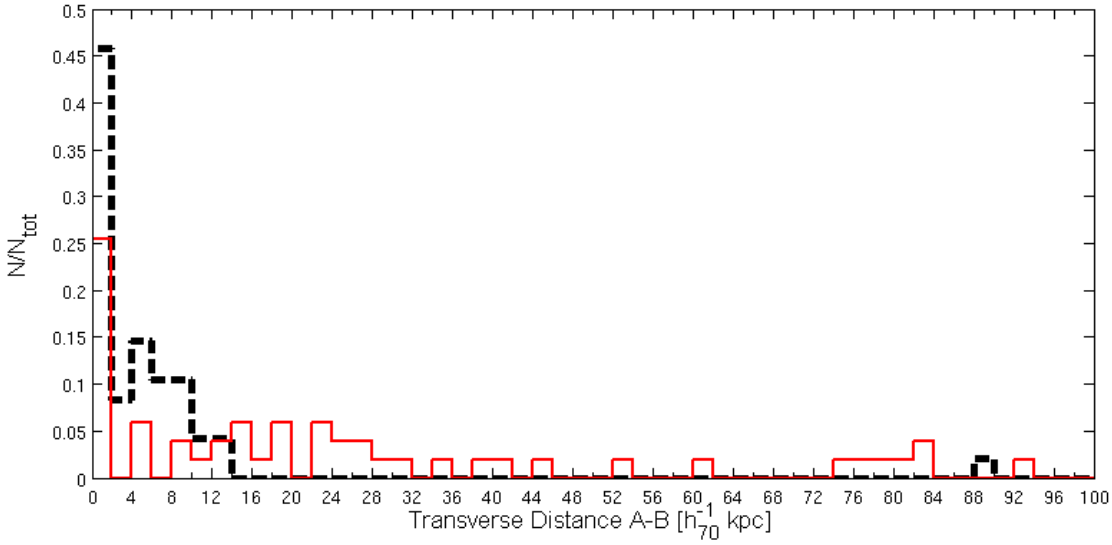

Figure 4.16: Histogram of transverse distances for the full sample. In black are coincidences and in red are anticoincidences. It is observed that at transverse separations less than 14 kpc the coincidences dominate over the anticoincidences. On the other hand, for transverse separations greater than 14 kpc, except for one case, the systems are only anticoincidences.

anticoincidences vary between 0.01 Å and 0.3 Å, even there is one case with upper limit of 1 Å. Therefore, the possibility exists that some anticoincidences become a coincidence if observed in higher SN or resolution spectra.

4.7 Equivalent Width differences between the LOS

Figure 4.17 shows the equivalent width in LOS B versus the equivalent width in LOS A. The literature sample is in black and the Calan sample is in red. The figure also shows upper limits. Significant variation of W_r is observed between the lines of sight in at all equivalent widths. Several anticoincidences are found, some cases even at large W_r. I remark this since, in case the gas falls smoothly with impact parameter those cases are produced only for distances comparable to the size of the absorber in case of a spherical geometry, or for highly inclined disk. Below I show which is the range of transverse distances covered by those cases.

4.8 Fractional equivalent width difference between the LOS

In order to analyze the differences between the lines of sight I defined, as in Ellison et al. (2004), the fractional equivalent width difference ΔW_r as

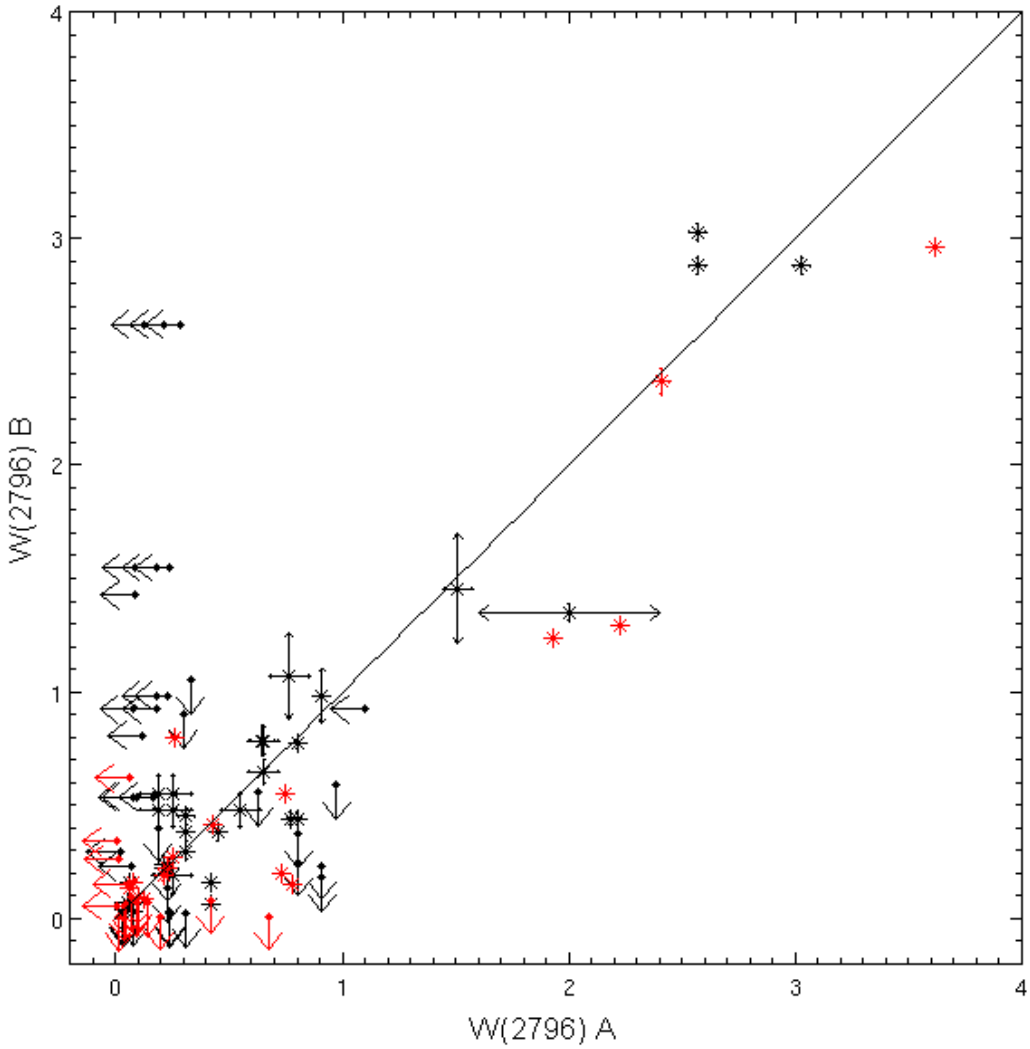

Figure 4.17: Equivalent width in A vs B line of sight. In black is the literature sample. In red is the Calan sample. I show the upper limits in A as left-pointing arrows and the upper limits in B as down-pointing arrows. The solid line represent $W_r^A = W_r^B$.

$$\Delta W_r = \frac{|W_r^A - W_r^B|}{max(W_r^A, W_r^B)} \tag{4.4}$$

In the case of anticoincidences, if the upper limit is lower than the measured equivalent width of the other LOS, then ΔW_r would be the value calculated using the W_r upper limit or higher, i.e in these cases the value of ΔW_r represent a lower limit. In case the upper limit is greater than the measured equivalent width, the real ΔW_r value can be greater or less than the calculated using the W_r upper limit. In the following analysis I did not use those systems because they do not provide much information (three absorptions in my sample and four in the literature sample).

4.8.1 ΔW_r versus equivalent width and transverse distance

Weak systems

I define weak systems as those in where the maximum equivalent width between the two absorptions is less than 0.3 Å

Figure 4.18 shows the fractional equivalent width difference versus (a) the maximum equivalent width between the two absorptions and (b) the transverse distance. Only the points with error bars less than 0.4 were plotted. I show the anticoincidences (that produce lower limits in ΔW_r) as up-pointing triangles.

There seems to be a trend of decreasing ΔW_r with equivalent width. In the case of transverse distances there is a trend of increasing ΔW_r until $\sim$ 4 kpc, after this, most of the points show low ΔW_r, even when the LOS are separated for $\sim$ 10 kpc. It is observed that most of the points that show low ΔW_r also show high W_r. Some of them are separated by $\lesssim$ 1 kpc, and the other group are absorptions separated by $\sim$ 10 kpc. There are anticoincidences in all the range of equivalent width and transverse separations.

Strong systems

I define strong systems as those in where the maximum equivalent width between the two absorptions is greater than than 0.3 Å

Figure 4.19 shows the fractional equivalent width difference versus (a) the maximum equivalent width between the two absorptions and (b) the transverse distance. Only the points with error bars less than 0.4 were plotted. I show the anticoincidences (that produce lower limits in ΔW_r) as up-pointing triangles.

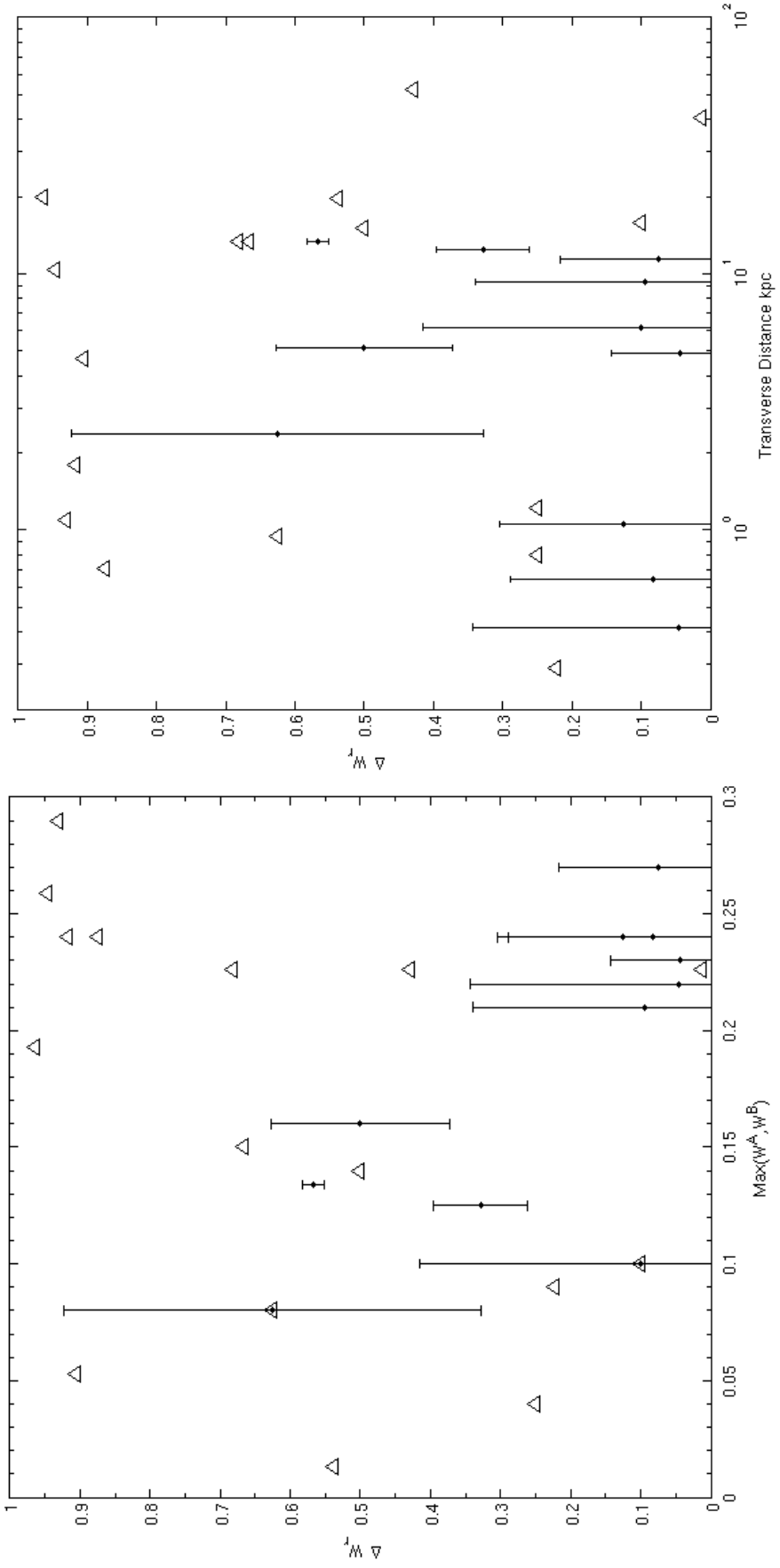

Figure 4.18: Fractional equivalent width difference versus (a) equivalent width and (b) transverse distance, for weak systems. Only the points with error bars less than 0.4 were plotted. The triangles represent lower limits.

In this case there is also a trend of decreasing ΔW_r with W_r. There is high dispersion for $W_r \lesssim 1.5$ Å and beyond this value, the dispersion is reduced and there are only coincidences with low ΔW_r and anticoincidences with high ΔW_r. The separations between the lines of sight at the absorption redshift of the coincidences with $W_r \gtrsim 1.5$ Å range between $0.5 < d < 10.5\ h_{70}^{-1}$ kpc. On the other hand, for anticoincidences (in the same equivalent width range) the separations range between $35 < d < 82\ h_{70}^{-1}$. Then, the anticoincidences occur at larger transverse distances that coincidences, in agreement with a smooth gas distribution. Following with the assumption of a smooth gas distribution (that it does not seem so unrealistic since we did not find anticoincidences at small transverse distances for high W_r) the smallest transverse distance of these anticoincidences ($35\ h_{70}^{-1}$ kpc) could represent then the size for strong systems in case of a spherical geometry and a lower limit for the size in case disk-like geometry.

The second plot shows that ΔW_r increase with the transverse separation. Also, most of the coincidences occur at large transverse separations not as weak systems.

These observations, for weak and strong systems, reinforce the idea that weak systems are smaller or more patchy than strong systems.

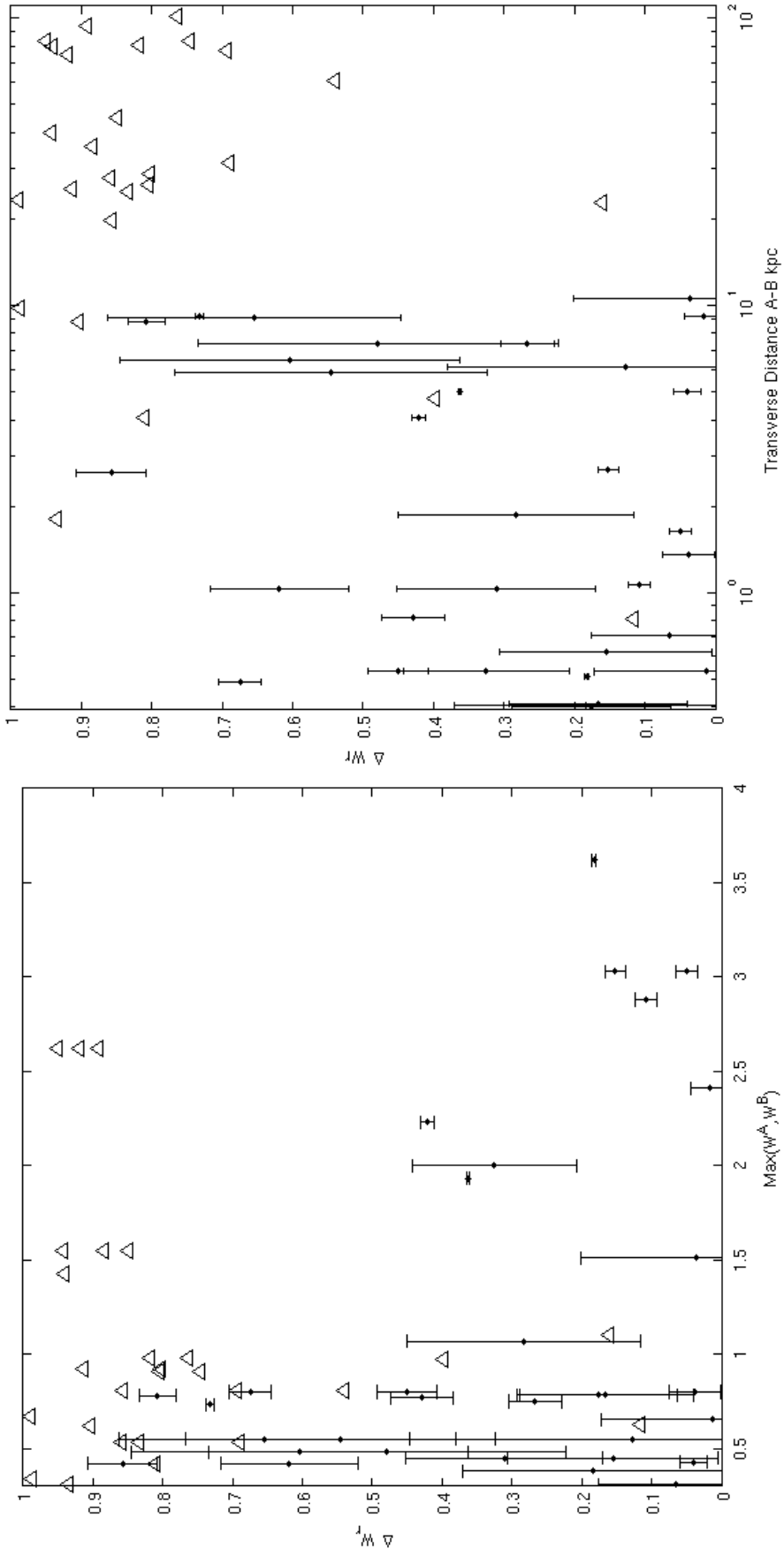

Figure 4.19: Fractional equivalent width difference versus (a) equivalent width and (b) transverse distance, for strong systems. Only the points with error bars less than 0.4 were plotted. The triangles represent lower limits.

Chapter 5

Characteristic sizes of MgII gaseous halos

In this chapter, two methods are presented that were used independently to estimate transverse sizes of MgII systems, both based on a likelihood analysis. Below I explain the methods and show the results.

5.1 Standard Likelihood analysis

This method is used to calculate the size of the absorber by maximizing the probability of having the observed number of coincidences and anticoincidences for a given transverse distance between the lines of sight. The analysis is purely geometric, i.e, it does not consider the strength of the absorptions, it just test the probability that the LOS cross the absorber. The formalism was developed by McGill (1990) and used the first time by Dinshaw et al. (1997). The method is "standard" in some sense because it has been used before to study Lyα systems size (Dinshaw et al. 1997, Lopez et al. 2000) and MgII systems (Smette et al. 1995, Ellison et al. 2004).

5.1.1 Calculating the Likelihood function

According to McGill (1990), the probability ϕ that a line of sight at distance d from the other line of sight crosses an absorber of radius R given that the last one did is

$$\phi_s = \begin{cases} \frac{2}{\pi}\left(\arccos(X) - X\sqrt{1-X^2}\right) & \text{for } X = \frac{d}{2R} \leq 1 \\ 0 & \text{for } X = \frac{d}{2R} > 1 \end{cases} \tag{5.1}$$

for spherical geometry, and

$$\phi_d = \begin{cases} \int_{-\pi/2}^{\pi/2} \frac{\cos(i)}{\pi} \left(\frac{\arccos(X)}{\cos(i)} - \frac{X}{\cos i}\sqrt{1 - \left(\frac{X}{\cos(i)}\right)^2} \right) di & \text{for } X = \frac{d}{2R} \leq \cos(i) \\ 0 & \text{for } X = \frac{d}{2R} > \cos(i) \end{cases} \tag{5.2}$$

for an infinitely thin disk-like geometry, where i is the inclination angle.

Then, the probability ψ that both lines of sight cross the absorber, given that one of them, A or B, crosses the absorber is

$$\psi_{s,d} = \frac{\phi_{s,d}}{2 - \phi_{s,d}} \tag{5.3}$$

The likelihood function, i.e, the probability of having N_c coincidences and N_a anticoincidences becomes

$$\mathcal{L} = \prod_{i=1}^{N_c} \psi_{s,d}(X) \cdot \prod_{i=1}^{N_a} [1 - \psi_{s,d}(X)] \tag{5.4}$$

Calculating $\mathcal{L}$ for several radii allows one to find the most probable radius.

5.1.2 Results

The full sample can be divided into weak ($W_r < 0.3$ Å) and strong ($W_r > 0.3$ Å) systems. I applied the method to 3 samples: full, weak and strong.

Figure 5.1 shows the likelihood functions for spherical geometry for the full (black), strong (red) and weak (blue) samples, along with their respectively cumulative distribution functions.

Table 5.1 summarizes the results for spheres and disks and the 1σ confidence intervals derived from the cumulative distribution function.

Two properties can be noted. The sizes inferred for spheres and disks are similar. Weak

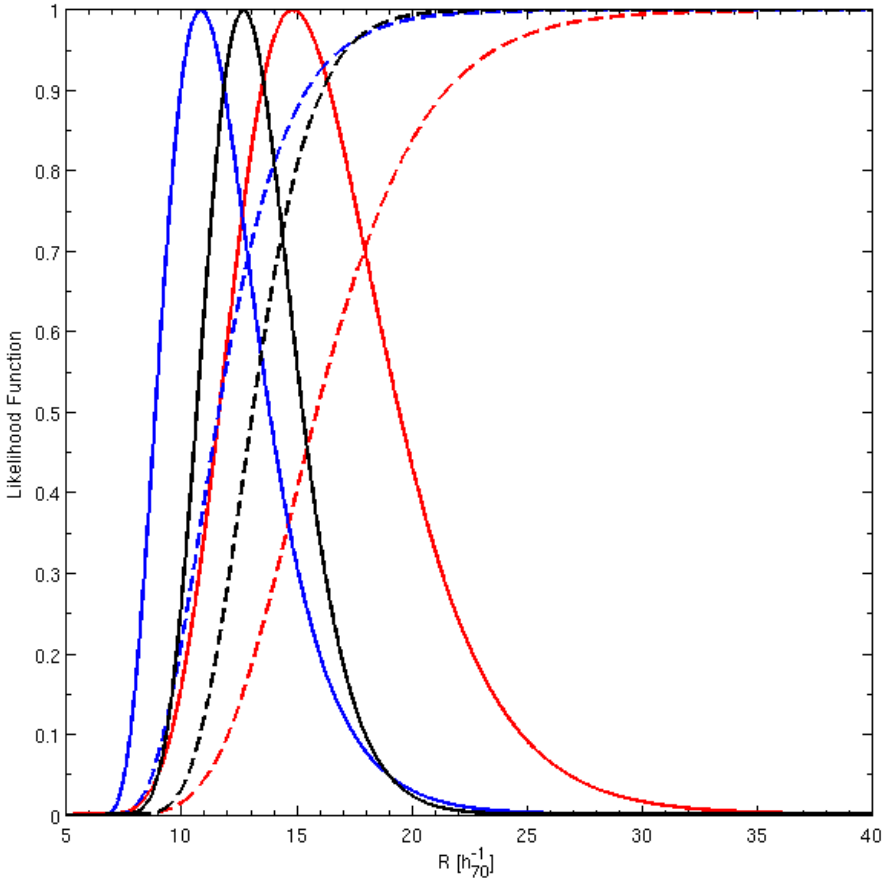

Figure 5.1: Likelihood function for spherical geometry. In black is the full sample, in red the strong sample and in blue the weak sample.

systems show a smaller size than strong systems.

5.1.3 Caveats

As pointed out by Martin et al. (2010), this technique does not converge to a reliable size if the transverse distances between LOS are comparable to the absorber diameter. This is because the calculated radius is at least half of the largest transverse separation at which a coincidence is observed.

In order to see if there is convergence in my results, following Martin et al. (2010) I calculated the likelihood function for 10 subsamples from the full sample with different maximum transverse distances at which a coincidence is observed. Figure 5.2 shows the most probale radius obtained from the maximum of the likelihood function versus the maximum transverse separation of each subsample (which is also the maximum trans-

Table 5.1: Results Standard Likelihood analysis

Geometry	R (Full sample) $[h_{70}^{-1}$ kpc]	R (Weak systems) $[h_{70}^{-1}$ kpc]	R (Strong systems) $[h_{70}^{-1}$ kpc]
Sphere	12.7 [11.3,15.4]	10.4 [9.7,14.4]	14.8[12.8,20.1]
Disk	12.5 [11.2,15]	11.1 [9.9,14.2]	14.5[12.5,15.4]

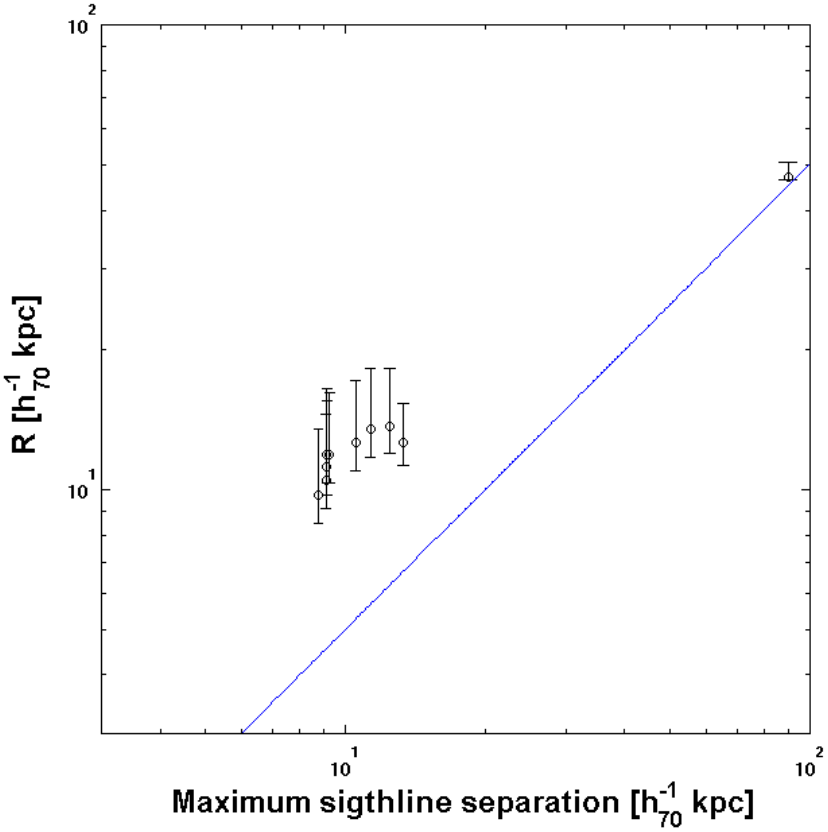

Figure 5.2: Radius obtained from the maximum of the likelihood function versus the maximum transverse separation for different subsamples from the full sample. The blue line represent $R = d/2$.

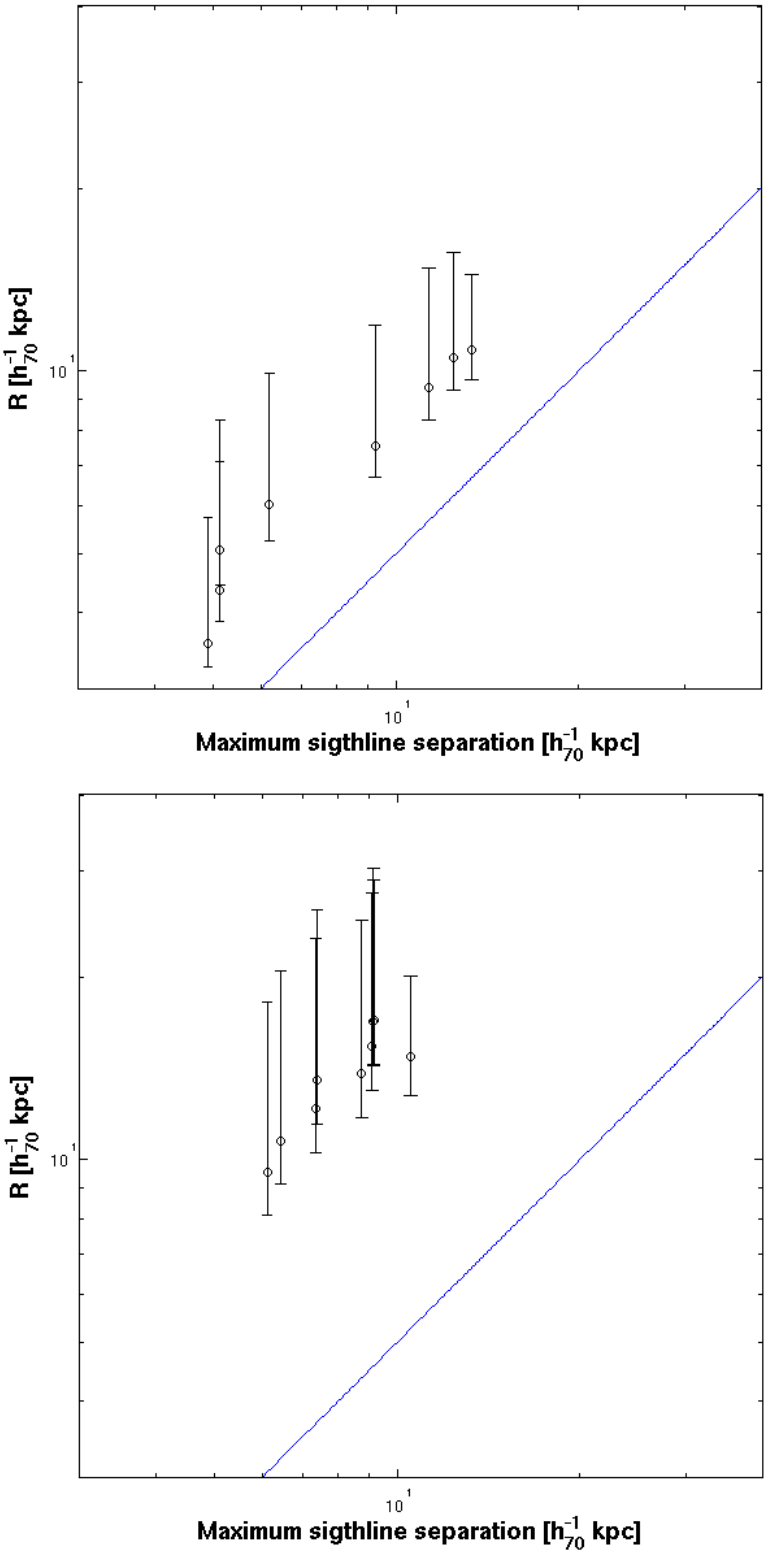

Figure 5.3: Radius obtained from the maximum of the likelihood function versus the maximum transverse separation for different subsamples from the sample (top) and strong (bottom) samples. The blue line represent $R = d/2$.

verse separation of a coincidence) for a spherical geometry. It is observed that when the maximum transverse distance increases, so does the most probable radius. For the largest transverse separation of a coincidence in the full sample, $\sim 90\ h_{70}^{-1}$ kpc, the radius obtained is in the line that represent $R = d/2$, i.e, it is not a reliable size. However, the method seems to converge for the four points before the last one. Figure 5.3 shows the same plot for the weak and strong population separately. In the case of weak absorption systems the method seems not to converge to a characteristic radius, i.e the most probale radius is always increasing with the maximum transverse separation. For strong systems it appears to be convergence for the last four points without consider the system separated by ~ 90 h_{70}^{-1} kpc mentioned before.

In the disk case the same trend is observed, i.e, convergence for the full and strong sample and no convergence for the weak sample.

For the full and strong sample the sizes in Table 5.1 correspond to the radius of maximum probability using the subsample that shows convergence with the larger number of pairs of systems. For weak systems the radius correspond to the last point in figure 5.3 calculated also using the subsample with the larger number of pairs.

5.2 Likelihood analysis including Equivalent width

The standard likelihood method can be improved by including information on line strengths. The idea is to infer a size using equivalent width in both LOS along with the calculated transverse separations of each z_{abs}. The weak and strong samples are treated separately. This idea was applied before to $Ly\alpha$ clouds by Dinshaw et al. (1997) and Smette et al. (1995).

The question to be answered is the following. Assuming a functional form for the equivalent width, as a function of impact parameter to the absorber, which size maximizes the probability of observing the measured equivalent widths?. The answer leads to the definition of a new Likelihood function, which gives the probability of having both, A and B equivalent widths as a function of transverse distance and assuming $W = W(r)$. As in the standard method, this likelihood depends on the assumed size so one can find the one that maximizes it for each pair of equivalent widths at the same time.

5.2.1 Equivalent Width as a function of impact parameter to the absorber

For the function describing W_r as a function of impact parameter I probed two forms: a logarithmic function and a power law.

The logarithmic function is motivated by the results of Nestor et al. (2005) regarding the equivalent width distribution $n(W)$[1]. Those authors studied SDSS data on 1300 systems with $W_r > 0.3$ Å and found that the strong population can be fitted by an exponential in the form of $n(W) = (N^*/W^*)e^{-W/W^*}$. Using data from Churchill et al. (1999) they concluded that the weak population also can be fitted by an exponential function with different values for N^* and W^*. I use this function to link the probability of obtaining an absorption system with $W > W'$ with the probability that the line of sight cross the absorber at impact parameter $r < r'$. The first probability is given by

$$P(W > W') = \int_{W'}^{\infty} \frac{N^*}{W^*} e^{-W/W^*} dW \tag{5.5}$$

Assuming that $W_r(r)$ is decreasing with impact parameter the probability of having an absorption system with $W > W'$ is equivalent to the probability that the LOS cross the absorber at impact parameter $r < r'$, where $W_r(r') = W'$. This last probability is given by

$$P(r < r') = \left(\frac{r'}{R_0}\right)^2 \tag{5.6}$$

where R_0 is the radius of the absorber. Then, combining equations 5.5 and 5.6 yields

$$W(r) = 2W^* \cdot \ln\left(\frac{R_0\sqrt{N^*}}{r}\right) \tag{5.7}$$

The power law function is motivated by the fit of Churchill et al. (1999) to the weak population: $dn/dW = C \cdot W^{-\alpha}$. Applying equation 5.5 to this distribution and combining with equation 5.6 gives

$$W(r) = r^{\frac{2}{1-\alpha}} \cdot \left(\frac{\alpha - 1}{CR_0^2}\right)^{\frac{1}{1-\alpha}} \tag{5.8}$$

In order to compare both functional forms I define a radius R_{max} at which the equivalent width reaches value of W_{min}. For radius larger than R_{max} I will consider that the

[1] $n(W) = d^2N/dzdW$

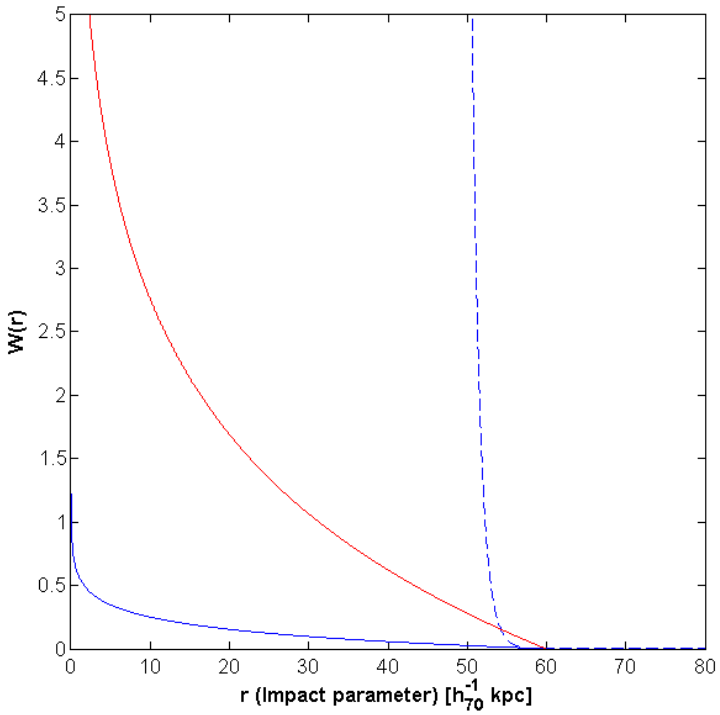

Figure 5.4: $W_{log}(r)$ and $W_pl(r)$ versus r for $W_{min} = 0.001$ Å and $R_{max} = 60\ h_{70}^{-1}$ kpc. The solid and dashed blue lines are $W_{log}(r)$ and $W_{pl}(r)$ for weak systems ($W^* = 0.07$, $\alpha = 1.04$). The red line is $W_{log}(r)$ for the strong systems ($W^* = 0.8$).

equivalent with is zero. Hence, the power law and logarithmic functions to test are given by

$$W_{pl}(r) = W_{min}\left(\frac{r}{R_{max}}\right)^{\frac{2}{1-\alpha}}, \tag{5.9}$$

and

$$W_{log}(r) = 2W^* \ln\left(\frac{R_{max}}{r}\right) + W_{min} \tag{5.10}$$

Figure 5.4 shows $W_{log}(r)$ and $W_{pl}(r)$ for $W_{min} = 0.001$ Å and $R_{max} = 60\ h_{70}^{-1}$ kpc. The solid and dashed blue lines are $W_{log}(r)$ and $W_{pl}(r)$ for weak systems ($W^* = 0.07$, $\alpha = 1.04$). The red line is $W_{log}(r)$ for the strong systems ($W^* = 0.8$).

Next step is to obtain R_{max} for each population assuming equations 5.9 or 5.10 and using values close to those given by Nestor et al. (2005) and Churchill et al. (1999) for α and W^* :

$$W^*_{weak} = 0.072$$

$$W^*_{strong} = 0.771$$

$$\alpha = 1.04$$

5.2.2 Calculating the Likelihood function $\mathcal{L}$

To get the likelihood function, L, I simulated pairs of LOS separated by different distances d at random impact parameters and orientations from a disk with random inclinations. Using these random LOS I then calculated the probability that an absorption in line of sight A has an equivalent width W^A and the other absorption in line of sight B has an equivalent width W^B given that they are separated by d. I calculated the equivalent width of each simulated line of sight using the equation 5.9 or 5.10 (with W_{min}=0.001 Å).

When a disk of radius R_{max} has an inclination i with respect to the line of sight the cross section becomes an ellipse with semiaxis R_{max} and $R_{max}\cos(i)$. Then, the idea is to randomly create pairs of points $[(x^A, y^B), (x^B, y^B)]$ that represent the coordinates of LOS A and LOS B such as at least one of them is inside the ellipse, meaning that *at least one line of sight, A or B, will have an absorption.*

Simulating pairs of LOS

For the first LOS I calculate a random coordinate x^A between $R_{max}+d$ and $-(R_{max}+d)$. Accordingly the coordinate y^A is calculated between $R_{max}\cos(i)+d$ and $R_{max}\cos(i)-d$, where i is the random inclination angle. After that, I set the coordinates of the second LOS as $x^B = x^A + d\cos(\phi)$ and $y^B = y^A + d\sin(\phi)$ where ϕ is a uniform random angle between 0 and 2π. I verify that the points (x^A, y^A) and (x^B, y^B) are inside the ellipse of semiaxis $R_{max}+d$ and $R_{max}\cos(i)+d$ and finally I accept the point only if the two pairs of coordinates $[(x^A, y^B), (x^B, y^B)]$ meet the condition that either (x^A, y^B) or (x^B, y^B) is inside the ellipse. The impact parameter is calculated as $r^{A,B} = \sqrt{(x^{A,B})^2 + \left(\frac{y^{A,B}}{cos(i)}\right)^2}$. Using the impact parameter, I obtain W^A and W^B using equation 5.10 or 5.9. This procedure was repeated to obtain N pairs $[W^A, W^B]$.

Note that the distribution of inclination angles is not uniform; indeed is proportional to $\sin(i)$, which reflects the fact that it is more likely that a disk is edge-on than face-on with respect to the sightline [2]. Select random inclination angles from this distribution is equivalent to select uniform distributed values to $\cos(i)$ between -1 and 1.

[2]However, in a real survey it has to be also considered that is more likely to cross a disk face-on than edge-on. I decided to not consider this effect

Figure 5.5 shows N=5 000 pairs of coordinates for sightlines crossing a spherical halo ($i = 0$), a disk with fixed inclination, and disks with randomly selected inclinations. It is observed that there are less points in the ring of width d. This is because if one LOS is inside the ring it is less likely that the other one is inside the cross section of the absorber, and therefore in these regions there are less pairs of LOS that meet the conditions.

Since both $W_{pl}(r)$ and $W_{log}(r)$ diverge at zero, I have constrained the simulations to $W^A \leq 5$ Å and $W^B \leq 5$ Å.

Simulated equivalent width in two LOS

Figure 5.6 shows $N = 50\,000$ values of W^A,W^B calculated using the logarithmic function $W_{log}(r)$ with two different W^* values close to the Nestor et al. (2005) values for the strong systems. Each plot has a fixed R_{max}, W^* and d and two geometries are used: spheres and randomly inclined disks. It is observed that the difference between spheres and disks is that the disks do not have sharp limits defining zero probability. This is due to the random inclinations.

The level of correlation between W^A and W^B depends on the ratio $\frac{d}{R_{max}}$. The smaller the distances more similar are W^A and W^B. Figures 5.6 show two cases, in one the equivalent widths are correlated and in the other, as d increases, they become highly anticorrelated. The level of correlation depends on the equivalent width. The correlation decreases with equivalent width.

If parameter W^* is increased, zones of high equivalent width start to populate (the upper right corner of the figures), thus increasing the probability of pairs with high W_r, and also increasing the more probable limits in which the equivalent width of one LOS can vary with respect the other.

Figure 5.7 shows W^A versus W^B calculated using the logarithmic and power law functions with two different W^* and α close to the literature values for weak systems.

The plots show the same properties that 5.6 with the variation of d at fixed radius and with increasing W^* or decreasing α. It is observed that the ratio between d and R_{max} that produce high or low correlation is different for $W_{log}(r)$ or $W_{pl}(r)$. For a fixed d, high correlation is reached at larger R_{max} for $W_{pl}(r)$ than for $W_{log}(r)$.

Before calculating L, some conclusions can be discerned from the models . The random inclinations allow one to obtain different equivalent widths for the same impact parameter. This is in agreement with the results of surveys that identified the galaxies responsible for

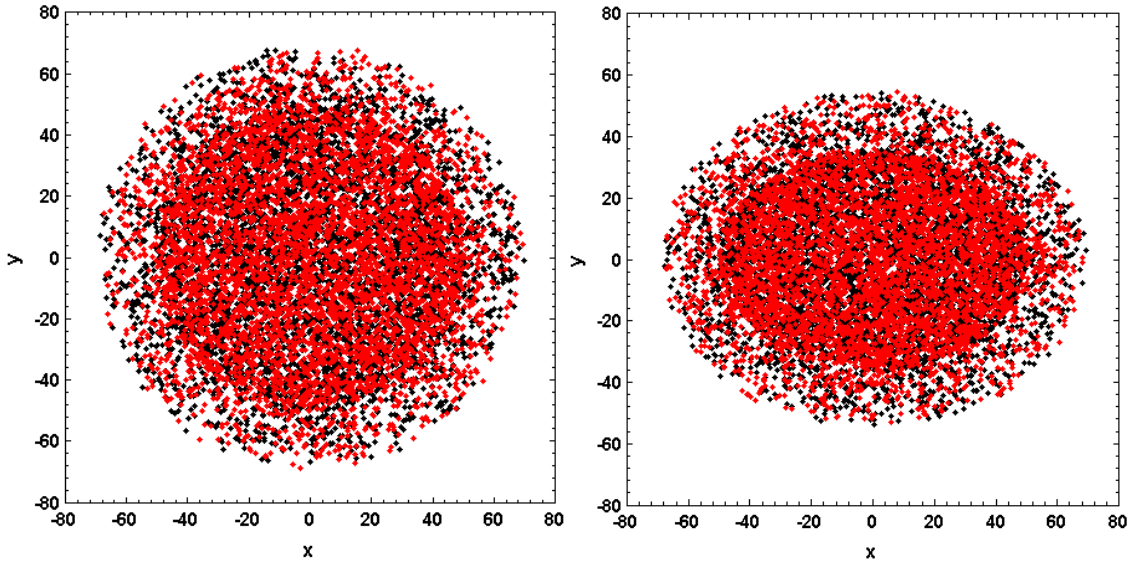

(a) sphere, $i = 0$

(b) disk, $i = \frac{\pi}{4}$

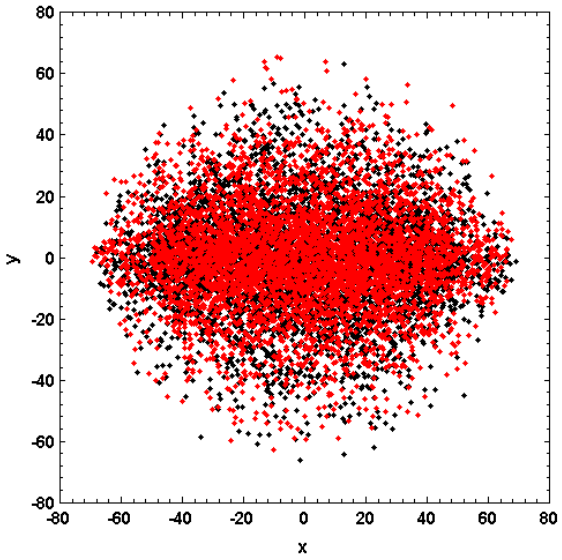

(c) disk, $-1 < \cos(i) < 1$

Figure 5.5: Example of random pairs $[(x^A, y^B), (x^B, y^B)]$ for a sphere (a), a disk with fixed inclination (b) and a disk with random inclinations (c). Black and red points represent LOS A and LOS B, respectively. In this particular sample $R_{max} = 50$, $d = 20$ and $N = 5000$. It is observed that there are less points in the ring of width d. This is because if one LOS is inside the ring it is less likely that the other one is inside the cross section of the absorber, and therefore in these regions there are less pairs of LOS that meet the conditions.

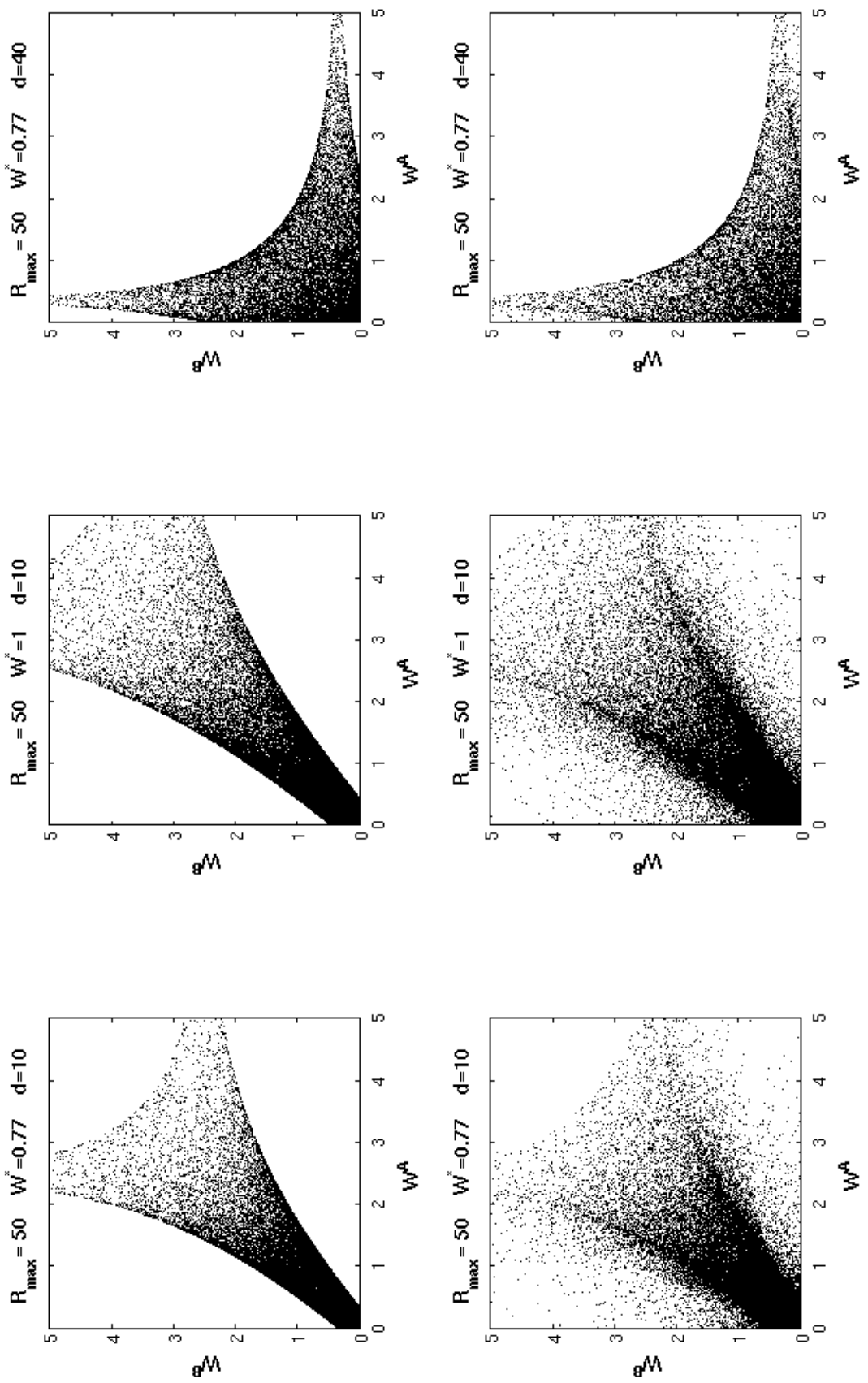

Figure 5.6: W^A versus W^B calculated using the logarithmic function $W_{log}(r) = 2W^* \ln(R_{max}/r) + W_{min}$ with two different characteristic W^*, both close to the Nestor et al. (2005) value for strong systems. Top: spherical geometry. Bottom: disk-like geometry.

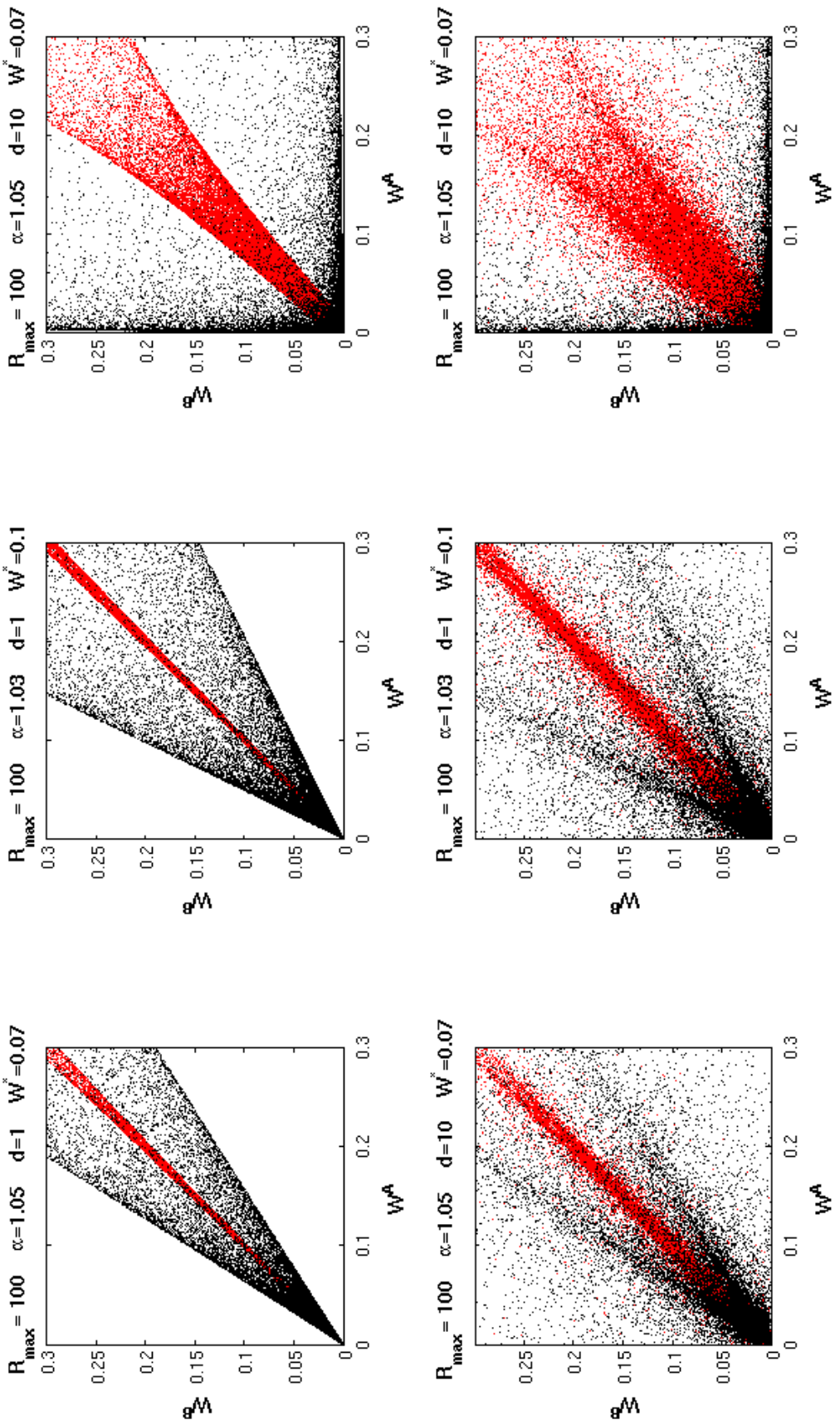

Figure 5.7: W^A versus W^B calculated using the logarithmic (red) $W_{log}(r)$ and power law $W_{pl}(r)$ (black) functions with two different W^* and α values close to the value by Nestor et al. (2005) and Churchill et al. (1999) for weak systems. Top: spherical geometry. Bottom: disk-like geometry.

the absorption since such surveys found patchy absorption below a certain impact parameters. For instance, Kacprzak et al. (2011) show that inclined disk help in reproducing the patchy absorptions. In addition my models show that disks can reproduce anticoincidences even at large equivalent width and small transverse distances.

Calculating the probabilities

In order to compare with observations, a likelihood function $\mathcal{L}$ must be calculated. $\mathcal{L}$ is defined such as for each z_{abs}, in a pair of lines of sight separated by $d(z_{abs})$, the probability that one LOS shows an absorption with W_r^A and the other one shows an absorption with W_r^B is calculated. One advantage of this method over the standard likelihood analysis is that I can use the anticoincidences considering particular upper limits on W_r.

For each z_{abs} in the sample I simulate $N = 100\,000$ pairs of $[W^A_{sim}, W^B_{sim}]$ whose LOS are separated by the observed transverse distance using the procedure explained above. Then, I calculate the probability that the real values of equivalent widths, $[W^A_{real}, W^B_{real}]$ occur under the assumed $W(r)$ function as

$$P(z_{abs}, d) = \begin{cases} \frac{N_{AB}}{N} & N_{AB} = \text{N\# pairs such that} \quad W^A_{sim} \in [W^A_{real} - 3E_{W^A_{real}}, W^A_{real} + 3E_{W^A_{real}}] \\ & \qquad\qquad W^B_{sim} \in [W^B_{real} - 3E_{W^B_{real}}, W^B_{real} + 3E_{W^B_{real}}] \\ & \qquad\qquad \text{if coincidence} \\ \frac{N_A}{N} & N_A = \text{N\# pairs such that} \quad W^A_{sim} \in [W^A_{real} - 3E_{W^A_{real}}, W^A_{real} + 3E_{W^A_{real}}] \\ & \qquad\qquad W^B_{sim} \leq UL_{W^B_{real}} \\ & \qquad\qquad \text{if the absorption is only seen in A} \\ \frac{N_B}{N} & N_B = \text{N\# pairs such that} \quad W^B_{sim} \in [W^B_{real} - 3E_{W^B_{real}}, W^B_{real} + 3E_{W^B_{real}}] \\ & \qquad\qquad W^A_{sim} \leq UL_{W^A_{real}} \\ & \qquad\qquad \text{if the absorption is only seen in B} \end{cases} \tag{5.11}$$

for the weak population and

$$P(z_{abs},d)=\begin{cases}\frac{N_{AB}}{N} & N_{AB}=\text{N\# pairs such that} \quad W^A_{sim}\in[W^A_{real}-0.4,W^A_{real}+0.4] \\ & \qquad\qquad W^B_{sim}\in[W^B_{real}-0.4,W^B_{real}+0.4] \\ & \qquad\qquad \text{if coincidence} \\ \frac{N_A}{N} & N_A=\text{N\# pairs such that} \quad W^A_{sim}\in[W^A_{real}-0.4,W^A_{real}+0.4] \\ & \qquad\qquad W^B_{sim}\leq UL_{W^B_{real}} \\ & \qquad\qquad \text{if the absorption is only seen in A} \\ \frac{N_B}{N} & N_B=\text{N\# pairs such that} \quad W^B_{sim}\in[W^B_{real}-0.4,W^B_{real}+0.4] \\ & \qquad\qquad W^A_{sim}\leq UL_{W^A_{real}} \\ & \qquad\qquad \text{if the absorption is only seen in B}\end{cases} \tag{5.12}$$

for the strong population.

$E_{W^X_{real}}$ is the error in the measured equivalent width in LOS X and $UL_{W^X_{real}}$ is the 3σ upper limit in LOS X in case there is not a detection, calculating using equation 4.2.

The only difference in the calculation of the probabilities is that for the weak population I include the points in the $(W^A,W^B)_{space}$ that are in a rectangle proportional to the errors and for the strong population I count the points in a square of side 0.8 Å. The reason for this is that the points in the $(W^A,W^B)_{space}$ are much less for the case of strong system than for weak systems and so, a small square or rectangle would produce a zero probability even with very high number of realizations.

Finally, the Likelihood function for each model is calculated as the product the probabilities calculated for each z_{abs}.

5.2.3 Results

Figures 5.8 and 5.9 show the likelihood function using the logarithmic and the power law functions for the weak sample. Figure 5.10 shows the Likelihood function using the logarithmic function for the strong sample.

In the case of weak systems, I started the simulations with $W^* \approx 0.07$ Å for $W_{log}(r)$ and I found better probabilities for values slightly higher. The more probable R_{max} is between 15 and 25 h_{70}^{-1} kpc having the higher probability for 20 h_{70}^{-1} kpc. As expected, R_{max} calculated using the power law function is larger. The higher probability is given by $\alpha = 1.04$ the same value of Churchill et al. (1999) and with R_{max} around 200 and 300 h_{70}^{-1} kpc with a most probably value of 250 h_{70}^{-1} kpc.

For the strong population R_{max} is around 20 and 60 h_{70}^{-1} kpc with a most probable value of 40 h_{70}^{-1} kpc.

In general I noted that the probabilities fluctuated a little when I calculated the Likelihood function more than once with the same W^* or α parameters, but they tend to have their maximum around the same values of R_{max}. Adding more points to the grid of R_{max} values require a lot of CPU time. Improving the efficiency of the method is possible by artificially populating more the high equivalent width zone and then make corrections by weighting the number of points. This would help improving accuracy since several R_{max} would be tested at fixed W^* or α.

5.2.4 Comparisons with the sample

ΔW_r **vs** $max(W_r^A, W_r^B)$

One advantage of this method is that it allows one to compare with the data.

For instance, figure 5.11 shows ΔW_r vs $max(W_r^A, W_r^B)$ of random LOS pairs generated using the same range of transverse distances from the weak sample and whose equivalent widths were calculated using the power law and the logarithmic function $W(r)$ with the parameters obtained from the likelihood method. The colors and contours indicate probability calculated from the fraction of points in smaller squares. Top figures show the distribution of points using the power law. To the left, all random LOS pairs are coincidences, the selected transverse distances are within the range given by the coincidences in the weak sample. To the right, the random LOS pairs can be coincidences or anticoincidences. The selected transverse distances are within the range given by the anticoincidences in the weak sample. In black is the full sample, points with error bars are the coincidences and triangles represent lower limits for anticoincidences. Bottom figures show the same, but the equivalent widths are calculated using the logarithmic function.

It can be seen that the power law function does not match with the data points in the case of coincidences. It predicts that the data should concentrate at high ΔW_r but instead the data show a dispersion along ΔW_r with a trend of declination at higher W_r. The

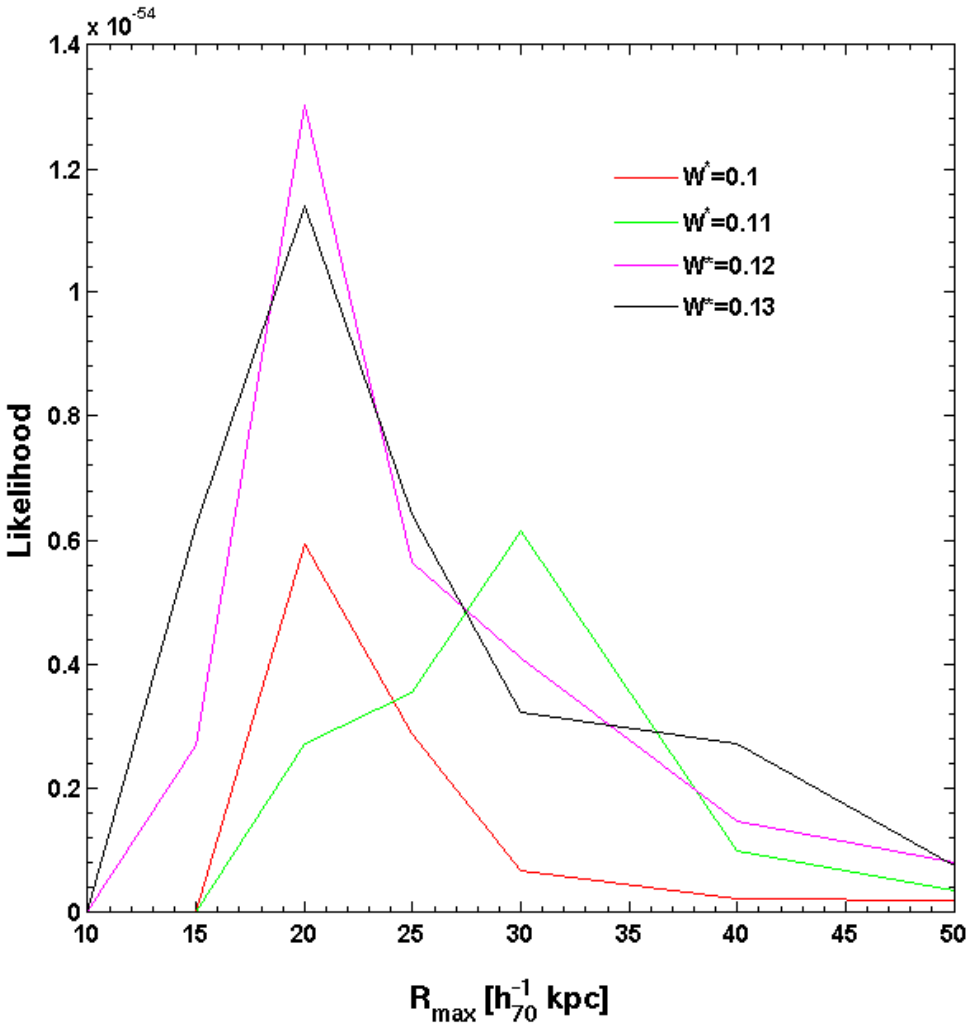

Figure 5.8: Likelihood function for the weak population, using the logarithmic function for different W^* close to $W^* = 0.07$ given by Nestor et al. (2005).

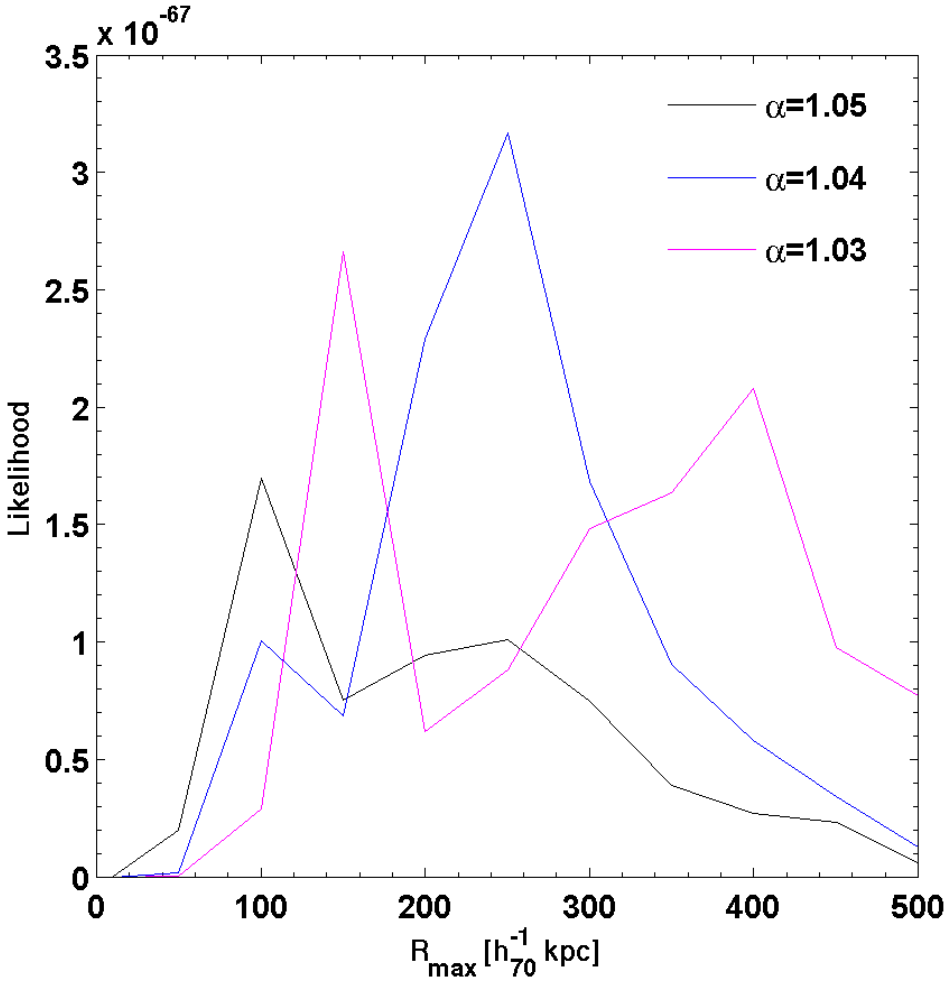

Figure 5.9: Likelihood function for the weak population, using the power law function for different α close to $\alpha = 1.04$ given by Churchill et al. (1999).

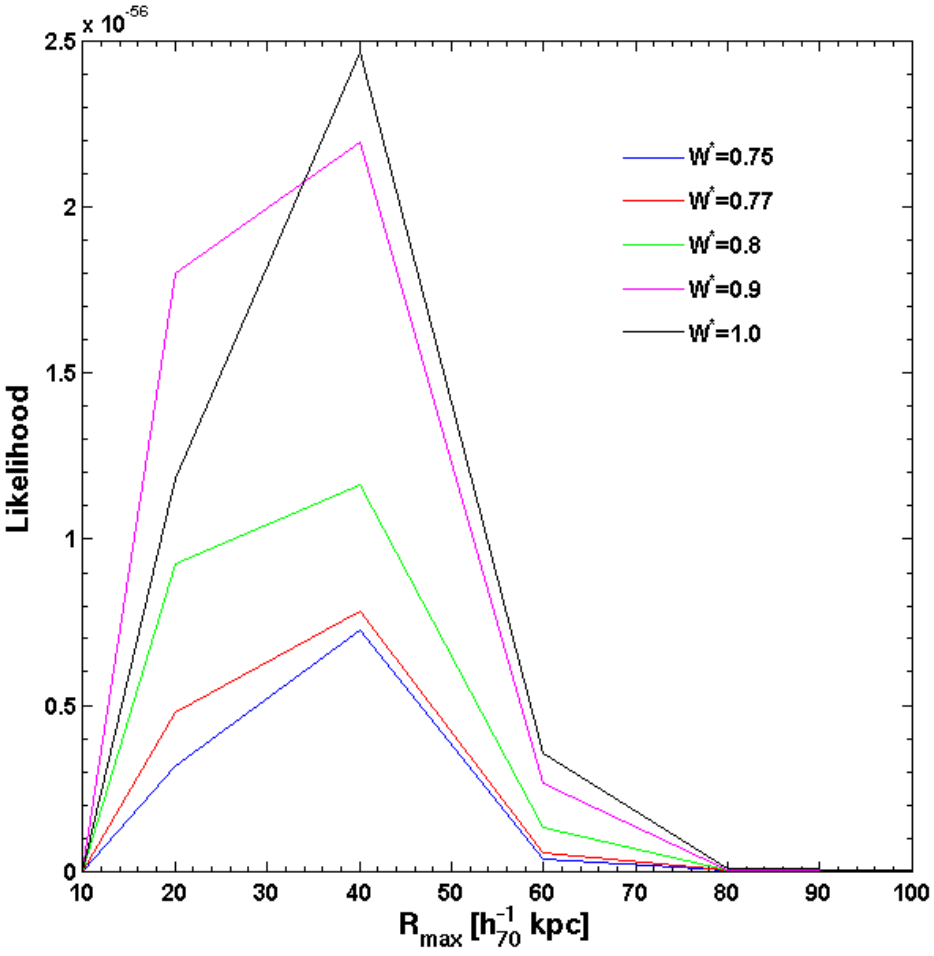

Figure 5.10: Likelihood function for the strong population, using the logarithmic function for different W^* close to $W^* = 0.77$ given by Nestor et al. (2005).

logarithmic function seems to be a better match agreement with the data: the random pairs tend to concentrate toward high W_r and low ΔW_r. Also, the distribution shows a larger area where the points can vary in ΔW_r, which contributes to account for the dispersion.

In the case of anticoincidences, both distributions match the observations. This is because both distribution present high probabilities near one (ΔW_r=1 in the model is an anti-coincidence). However, the logarithmic function could be a better model since the high probability zone is larger than for the power law. Also, there is a greater concentration of points at lower ΔW_r for all W_r (in case some lower limits were not real anticoincidences.)

Figure 5.12 is similar to 5.11 but for the strong sample. In the case of coincidences the model reproduces the observed trend of decreasing dispersion with increasing ΔW_r. The points with smaller W_r and high ΔW_r present a distinct characteristic in the data: one of the LOS shows a weak system. Figure 5.13 shows this special case. It uses the logarithmic function and pairs of sightlines restricted to be a coincidence and to show a weak and a strong absorption. The random transverse distances are selected from the same interval given by the data. The random points are in a restricted zone in the plot, the same zone traced by the data.

I conclude that for strong systems the coincidences that produce high ΔW_r are produced by LOS that present a weak absorption and a strong absorption. High ΔW_r seems to happen in data only for smaller W_r in agreement with the assumed smooth relation between W_r and impact parameter. As I mentioned in 4.4.3, if the gas was distributed with several holes we would expect to find high ΔW_r even for high W_r which is not the case. The figure to the right that shows anticoincidences has some points with high W_r and high ΔW_r but the mean transverse distance for those points is $\sim$ 45 h_{70}^{-1} kpc, while for the coincidences sample is only $\sim$ 5 h_{70}^{-1} kpc. Therefore, those anticoincidences are still in agreement with the model. Thus, holes are not likely to be inside a radius of less than $\sim$5 h_{70}^{-1} kpc centered in one line of sight (or $\sim$9 h_{70}^{-1} if we take the maximum transverse distance for the coincidences). This is equivalent to say that the covering factor in near unity below these radii.

For anticoincidences, as the triangles represent lower limits, the zone of high probability close is consistent with the data. This means that transverse distances corresponding $\sim$ 45 h_{70}^{-1} kpc, the strong sample is likely to show anticoincidences which is expected given that $R_{max} \approx 40\ h_{70}^{-1}$ kpc according to the likelihood function.

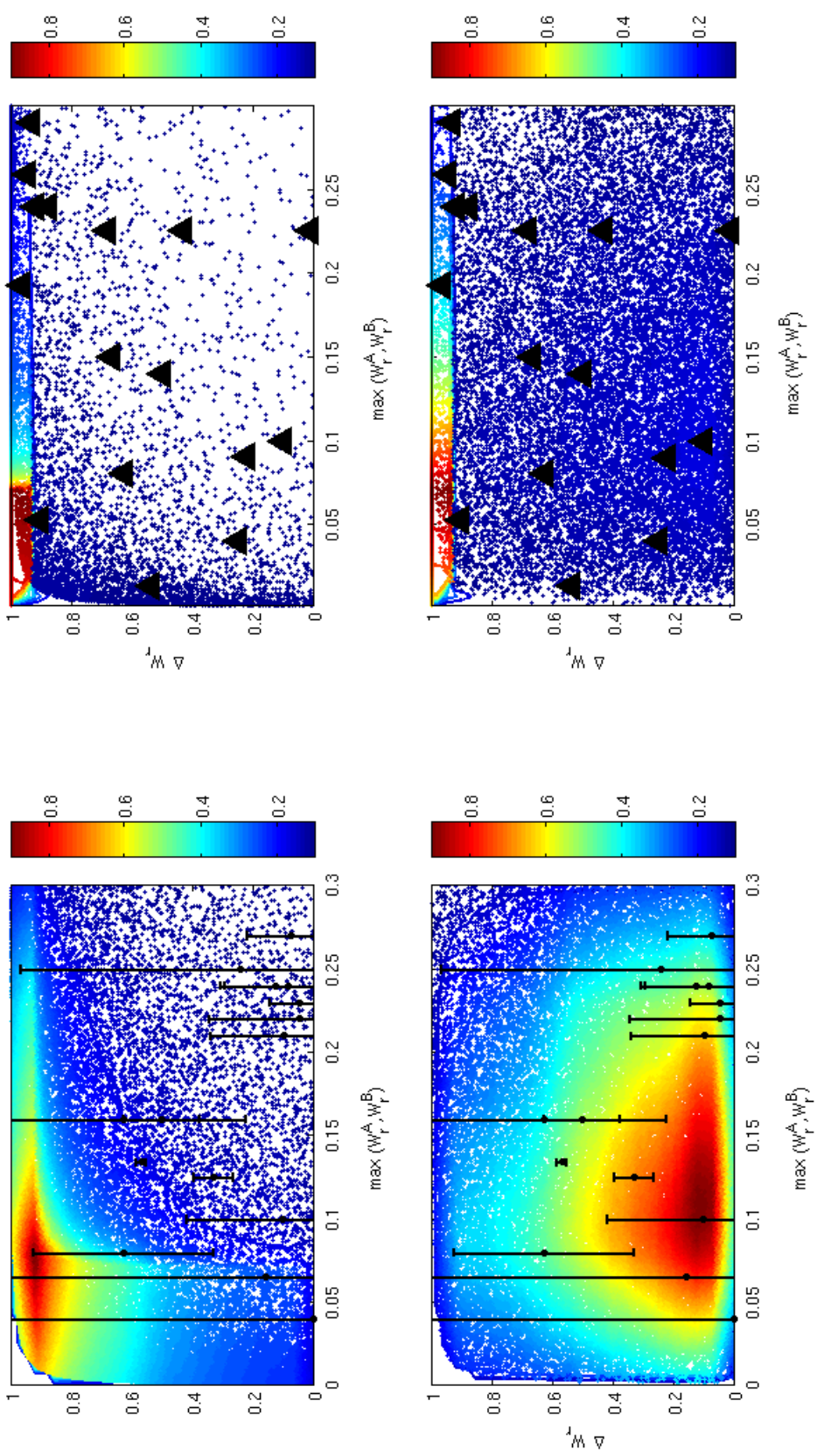

Figure 5.11: ΔW_r vs W_r of random LOS pairs generated using the same range of transverse distances of the weak sample. The equivalent width were calculated using the power law and the logarithmic function $W(r)$ with the parameters obtained from the likelihood method. The colors and contours indicate probability calculated as number of points in smaller squares over total number of points, then it is normalized to the higher value in order to compare. Top panels show the distribution of points using the power law. To the left, the random LOS pairs only are coincidences and the transverse distances selected are from the range given by the coincidences in the weak sample. To the right the random LOS pairs can be coincidences or anticoincidences and the transverse distances selected are from the range given by the anticoincidences in the weak sample. In black is the full sample, points with error bars are the coincidences and triangles represent lower limits for anticoincidences. Bottom panels are the same, but the equivalent widths are calculated using the logarithmic function.

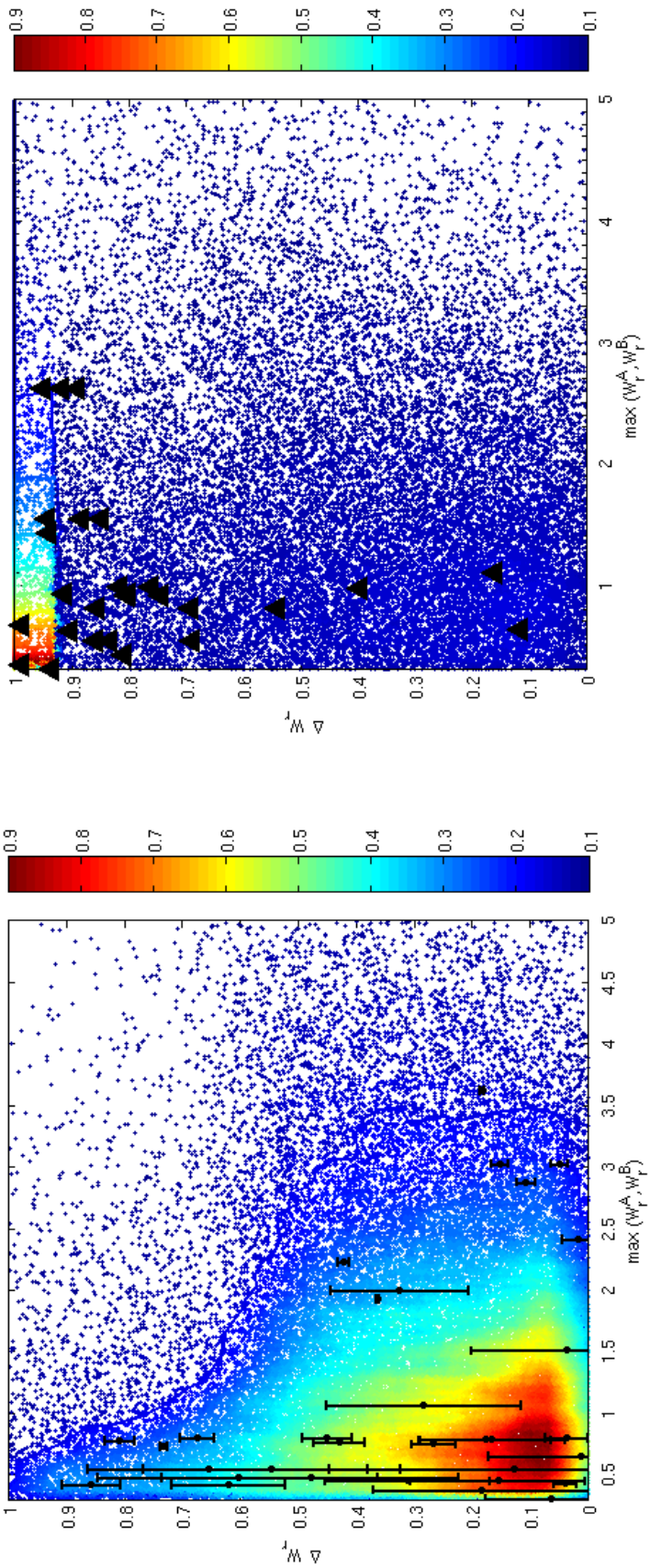

Figure 5.12: ΔW_r vs W_r of random LOS pairs generated using the same range of transverse distances of the strong sample. The equivalent width were calculated using the logarithmic function $W(r)$ with the parameters obtained from the likelihood method. The colors and contours indicate probability calculated as number of points in smaller squares over total number of points, then it is normalized to the higher value in order to compare. To the left, the random LOS pairs only are coincidences and the transverse distances selected are from the range given by the coincidences in the strong sample. To the right the random LOS pairs can be coincidences or anticoincidences and the transverse distances selected are from the range given by the anticoincidences in the strong sample. In black is the full sample, points with error bars are the coincidences and triangles represent lower limits for anticoincidences.

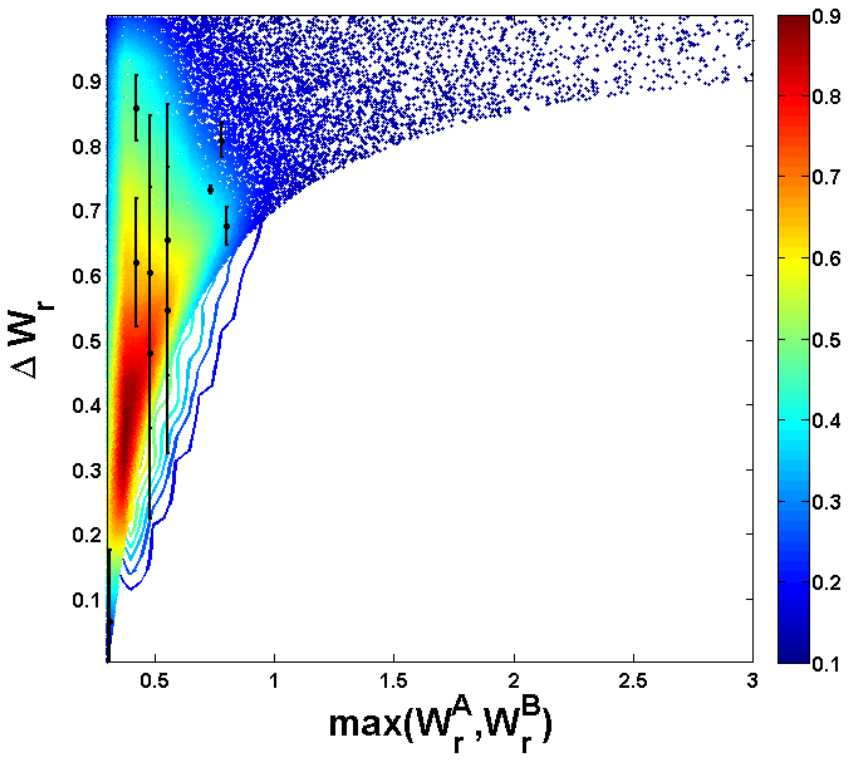

Figure 5.13: ΔW_r vs W_r of random LOS pairs generated using the same range of transverse distances of the strong coincidences sample, restricted to show one weak absorption and one strong absorption. The equivalent width were calculated using the logarithmic function $W(r)$ with the parameters obtained from the likelihood method. The colors and contours indicate probability calculated as number of points in smaller squares over total number of points, then it is normalized to the higher value in order to compare. Black points with error bars is the sample with the same restrictions mentioned above.

ΔW_r versus Transverse distance

Figures 5.14 and 5.15 are similar to 5.11 and 5.12 respectively but this time ΔW_r is presented against transverse distance.

For weak systems (figure 5.14), both functions $W_{log}(r)$ and $W_{pl}(r)$ seem to match observations. In the case of coincidences both models reproduce the data at transverse distances $d \lesssim 3 - 4\ h_{70}^{-1}$ kpc. After this limit, there is a decrease in the data that is not consistent with the models. It can be that this limit mark the transition from a smooth distribution of gas to a patchier distribution. Therefore, the size given by the likelihood analysis could be overestimated and these systems are more likely to have a radius between $3 - 4\ h_{70}^{-1}$ kpc.

For strong systems (figure 5.15), the model is consistent with the data at all the range of transverse distances.

Both comparison of ΔW_r, versus W_r and transverse distances are in agreement with the picture of weak systems smaller and patchier that strong systems. It could be that weak systems are smaller than the estimated size. The strong systems are in a good agreement with a smooth distribution of gas and they match the model with the estimated size $20-60$ h_{70}^{-1} kpc.

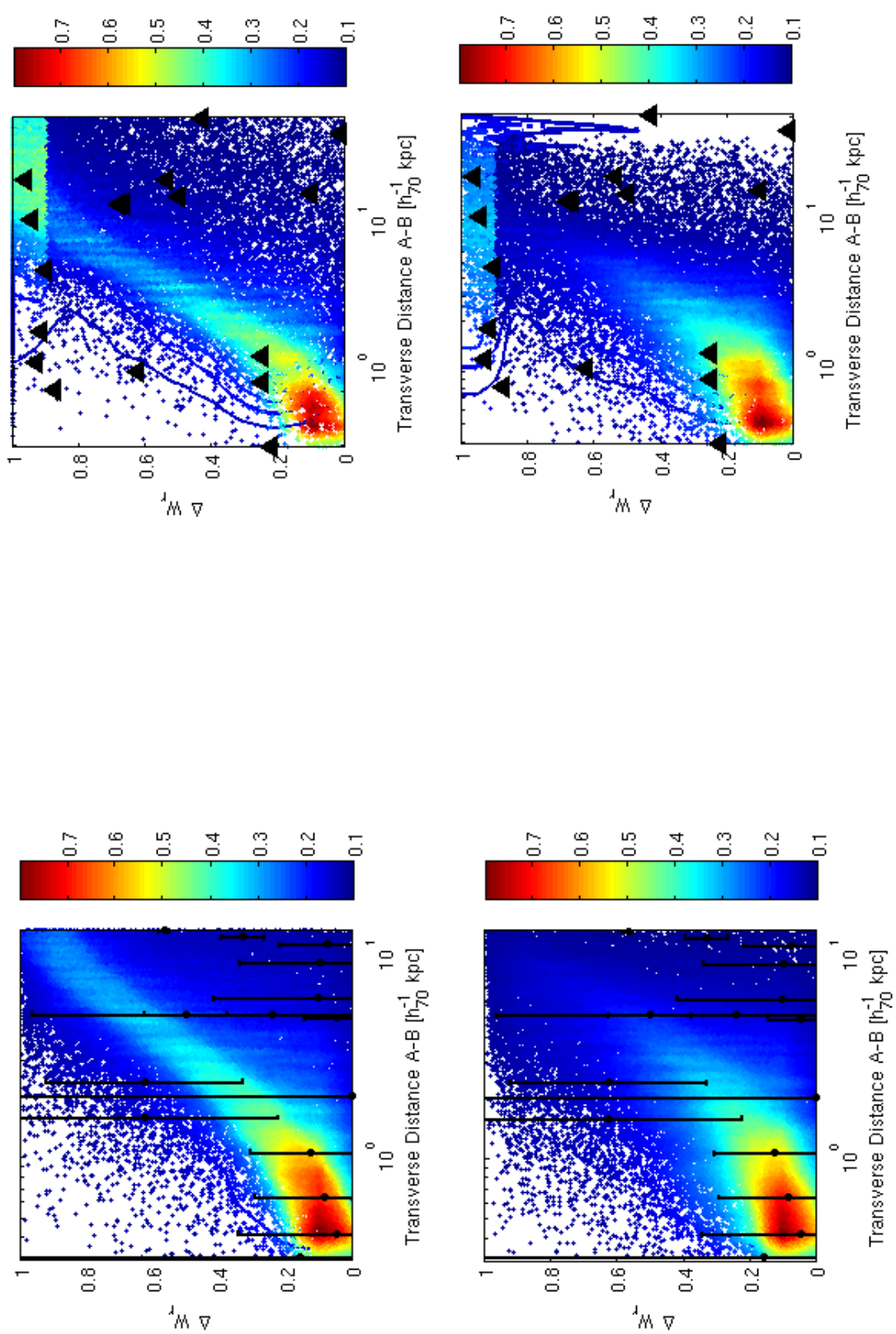

Figure 5.14: ΔW_r vs. transverse distances of random LOS pairs generated using the same range of transverse distances of the weak sample. The equivalent width were calculated using the power law and the logarithmic function $W(r)$ with the parameters obtained from the likelihood method. The colors and contours indicate probability calculated as number of points in smaller squares over total number of points, then it is normalized to the higher value in order to compare. Top panels show the distribution of points using the power law. To the left, the random LOS pairs only are coincidences and the transverse distances selected are from the range given by the coincidences in the weak sample. To the right the random LOS pairs can be coincidences or anticoincidences and the transverse distances selected are from the range given by the anticoincidences in the weak sample. In black is the full sample, points with error bars are the coincidences and triangles represent lower limits for anticoincidences. Bottom panels are the same, but the equivalent widths are calculated using the logarithmic function.

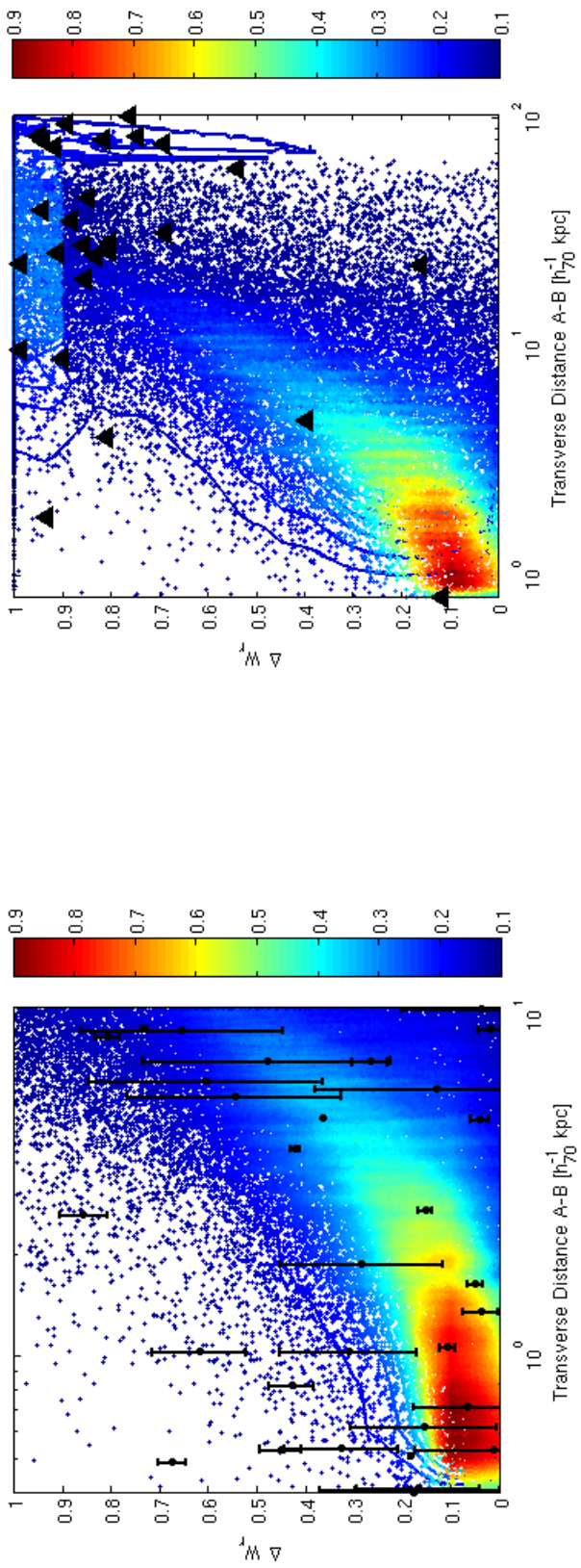

Figure 5.15: ΔW_r vs transverse separation of random LOS pairs generated using the same range of transverse distances of the strong sample and whose equivalent width were calculated using the logarithmic function $W_{log}(r)$ with the parameters obtained from the likelihood method. The colors and contours indicate probability calculated as number of points in smaller squares over total number of points, then it is normalized to the higher value in order to compare. To the left, the random LOS pairs are only coincidences and the transverse distances selected are from the range given by these points in the strong sample. To the right the random LOS pairs can be coincidences or anticoincidences and the transverse distances selected are from the range given by the anticoincidences in the strong sample. In black is the full sample, points with error bars are the coincidences and triangles represent lower limits for anticoincidences.

Chapter 6

Absorption systems at lens redshifts

The subsample of systems associated to the lens galaxies is interesting because the impact parameters are known.

In the Calan sample, I found a MgII absorption system at $z_{abs} \sim z_{lens}$ for all quasars, but SDSS J1335+0118 and HE0230-2139. For these systems I sought in the literature and CASTLES[1] webpage the distances in arcseconds between multiple images and lens. I then calculated the impact parameter of the LOS to the lens galaxy using equation 4.3. Table 6.1 summarizes these data, where Δv is the velocity difference between the system and the lens galaxy (z_{lens} restframe). I will call this sample the lens sample.

Chen et al. (2010) searched for galaxies responsible for the MgII absorptions in selected QSO spectra. They identified 71 isolated galaxies lying at less than 120 h_{70}^{-1} kpc from an absorber. Seven cases were identified as galaxies that are likely to reside in groups.

Figure 6.1 shows the rest frame equivalent width versus impact parameter for both the lens and Chen et al. (2010) samples. In red is the lens sample and in black the Chen et al. (2010) sample. It is observed that the lens sample present impact parameters which are smaller the Chen et al. (2010) sample.

It is expected that the lens sample be biased to small impact parameter due to the lens geometry. Einstein radius is in the order of $r_E \sim 3\ h_{70}^{-1}$ kpc for an individual lens with mass $\sim 10^{11}\ M_\odot$ considering $z_{lens} \approx 0.5$ and $z_{source} \approx 2$ (Wambsganss 2001). Also in the Chen sample it is expected not to find such smaller impact parameters because they preselected the galaxies in order to find the one responsible for the MgII absorption system

[1]CfA-Arizona Space Telescope LEns Survey of gravitational lenses (Kochanek et al. 1999)

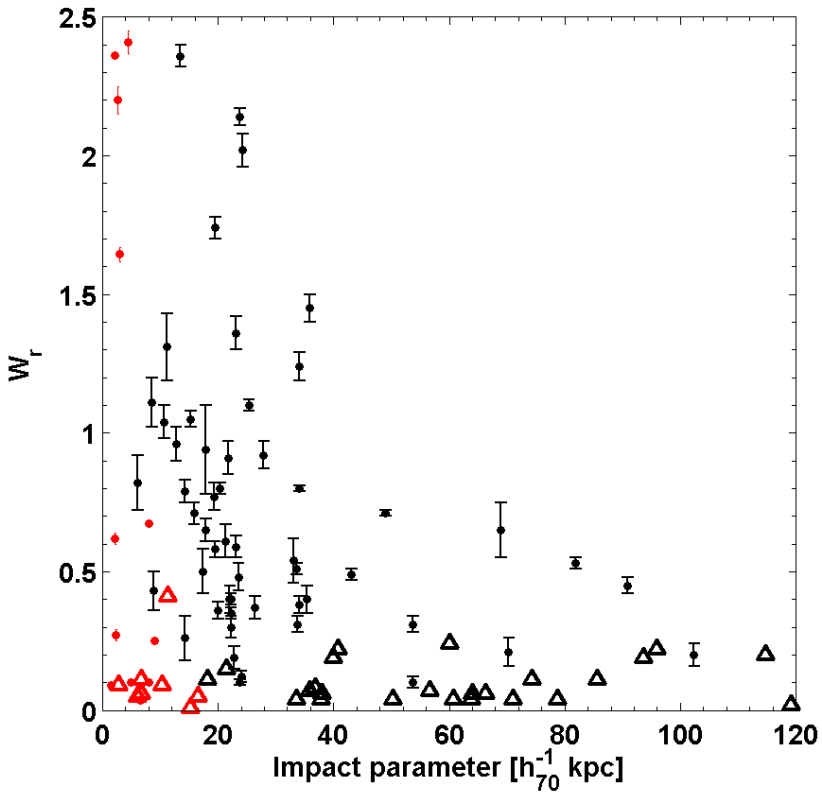

Figure 6.1: W_r versus impact parameter. In red is the lens sample. In black the Chen et al. (2010) sample. Triangles represent upper limits.

in a quasar spectrum. They preselected galaxies from the SDSS Data release 6 with the constrain of being as close as much to a QSO LOS. This explains why they could not select galaxies closer than 6.1 h_{70}^{-1} kpc to the QSO LOS, due to the bright QSO disc. The mean value of impact parameters in Chen et al. (2010) sample is ~ 40 h_{70}^{-1} kpc. For lenses, the situation is different as the lensing galaxies are found after the lensed QS0 is detected.

Other parameters that distinguish the two samples are redshift and galaxy type. The redshift constrain for galaxies in Chen et al. (2010) put the lens sample in a different redshift range: while the galaxies from the Chen et al. (2010) sample have $z_{spec} \leq 0.5$, the lens galaxies from the lens sample have $z_{spec} \geq 0.44$. Regarding galaxy type, as mentioned in chapter 2, all but one of the lens galaxy are elliptical. In the case of Q1017-207, Q1355-2257, SDSS J0806+2006, SDSS J1335+0118 and HE2149-2745 the lens configuration is: the two images in opposite sides to the lens galaxy, and the weaker closer to the lens. According to Blandford & Narayan (1992) this occur in case that of an off-axis source and then, the weaker image is inside the einstein ring and the brighter outside this ring. Then, given the impact parameters in Table 6.1 the mass of these systems range between $M \approx 10^{10} - 10^{11}$ $M_{\odot}$. Therefore, the lens sample is composed mostly for massive galaxies..

Note that detecting MgII in most of these lenses disproves the common belief that elliptical do not produce absorption systems. The Chen sample has a variety of types of galaxies (early and late type, irregular and start forming galaxies).

Considering that these two samples are not directly comparable, it is worthwhile to probe the match of the functions $W_r(r)$, tested in chapter 5 with both lens and Chen et al. (2010) sample.

Figure 6.2 shows the weak systems from both the lens (red) and Chen et al. (2010) (black) samples. It is observed that for the weak population the trend of decreasing W_r with impact parameter is not so clear considering both samples. This is expected if weak systems are, as the results of previous chapters suggest, smaller clouds and if the impact parameter calculated here (that is, the impact parameter to the galaxy) is not necessary the impact parameter to the center of these clouds. Thus, it is possible to observe weak systems at high impact parameter and that does not mean that the impact parameter is related to the size of the systems.

Weak systems from the lens sample agree with the model. However, as I mentioned before it can be that the size estimated for this model be overestimated and could be that in some cases given the small impact parameter this value also correspond to the size of these clouds. However, connection is not obvious.

Figure 6.3 is the same as Figure 6.2 but for the strong systems. In this case the trend of decreasing W_r with impact parameter is clear. Note that few points have impact parameters larger than $40 - 60\ h_{70}^{-1}$ kpc that is the estimation size that I obtained using the likelihood analysis with impact parameter. These points could correspond to galaxy-satellite pairs or groups. In fact, according to Chen et al. (2010) the points at $r \sim 70$ and $r \sim 80\ h_{70}^{-1}$ are not isolated galaxies.

In conclusion, both the lens and the Chen et al. (2010) samples are in agreement with my results: weak systems are likely to be smaller and more patchy than strong systems. The latter are in agreement with a smooth distribution and sizes in the range $40 - 60\ h_{70}^{-1}$ kpc.

Table 6.1: Absorption systems at $\sim z_{lens}$

QSO	z_{abs}^A	z_{abs}^B	z_{lens}	Δv^A [km/s]	Δv^B [km/s]	W_r^A [Å]	W_r^B [Å]	r^A [h_{70}^{-1} kpc]	r^B [h_{70}^{-1} kpc]
Q1017-207	0.7951	0.7953	0.78±0.07	2560(±11890)	2576.9(±11890)	0.10±0.01	0.09±0.01	4.90	1.40
Q1355-2257	...	0.7022	0.702±0.001	...	35.29(±176.15)	<0.06	0.62±0.02	6.64	2.139
SDSSJ0806+2006	0.5730	0.5736	0.573±0.001	0(±190.60)	114.35(±190.66)	2.41±0.04	2.37±0.06	4.46	2.68
SDSSJ1335+0118	...	...	0.44±0.001	...	...	<0.05	<0.09	6.14	2.78
WFI2033-4723	0.6586	...	0.661±0.001	-433.17(±180.23)	...	0.10±0.01	<0.09	8.10	10.27
HE0230-2130	...	...	0.523±0.001	...	...	<0.11	<0.41	6.64	11.38
HE2149-2745	0.6010	0.6011	0.603±0.001	-374.04(±186.79)	-355.34(±186.80)	0.25±0.01	0.27±0.02	9.08	2.31
HE1104-1805	0.7278	...	0.729±0.001	-208.07(±173.27)	...	0.673±0.003	<0.007	7.98	15.21
HE0512-3329	0.9311	0.9304	0.931±0.001	0(±155.25)	-93.151(±155.20)	2.362±0.004	1.644±0.008	2.09	3.01
RXJ0911+0551	0.7747	...	0.769±0.001	965.98(±170.02)	...	0.035±0.002	<0.05	6.59	16.61

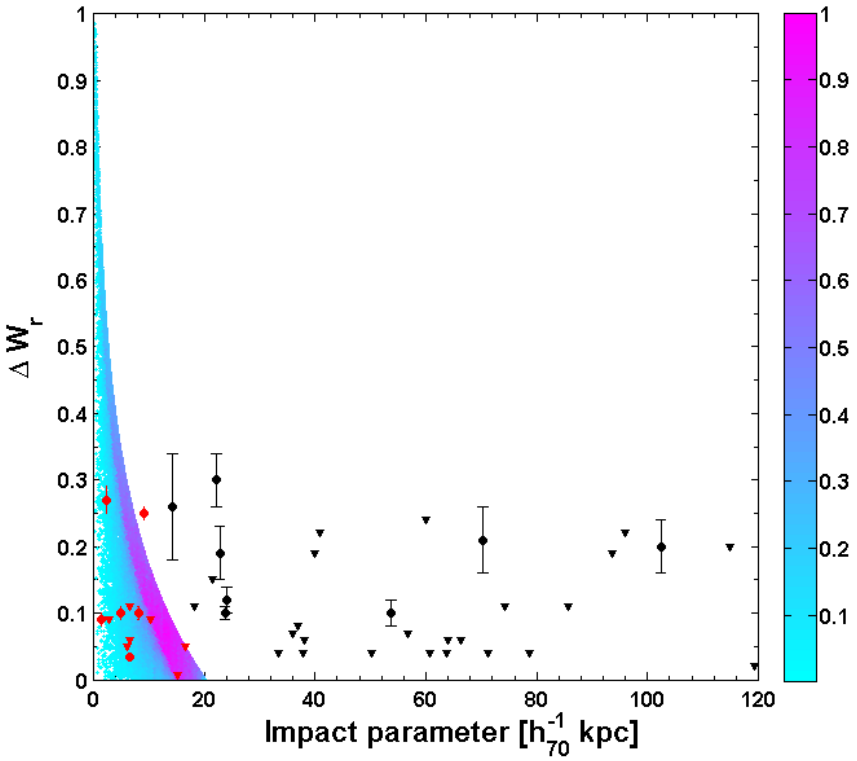

Figure 6.2: W_r versus impact parameter. In red is the lens sample and in black the Chen et al. (2010) sample. Triangles represent upper limits. Colored points represent probability from my model. Each probability point is a random LOS in a disk with random inclination and distributed according with $W_{log}(r)$ for weak systems.

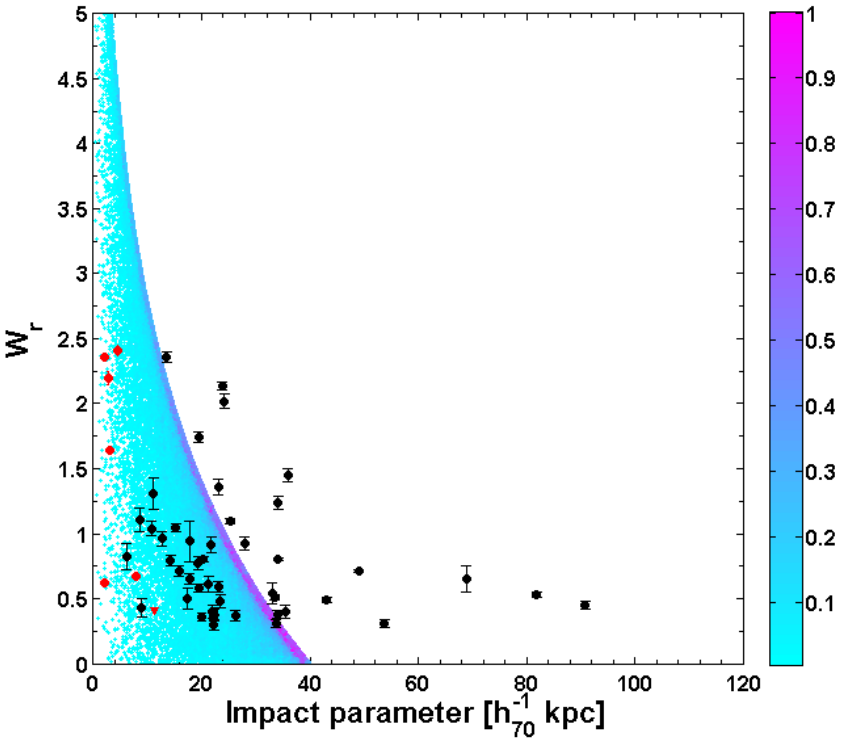

Figure 6.3: W_r versus impact parameter. In red is the lens sample and in black the Chen et al. (2010) sample. Triangles represent upper limits. Colored points represent probability from my model. Each probability point is a random LOS in a disk with a random inclination distributed according with $W_{log}(r)$.

Chapter 7

Summary and conclusions

In this thesis I have presented a search for MgII absorption systems in the resolved spectra of 10 gravitationally lensed quasars. These quasars were observed at resolutions $R \sim 4\,500$ and $R \sim 40\,000$. The search yielded a sample composed of 28 MgII absorption systems at $0.4 < z < 1.6$, and with transverse separations between lines of sight (LOS) in the range 0.29-23 h_{70}^{-1} kpc. Adding systems from the literature increased the number of systems to 92. The range of transverse separation of the full sample is 0.3-100 h_{70}^{-1} kpc. Using the full sample I studied the fractional equivalent width differences ΔW_r as function of equivalent width and transverse distances. I also studied MgII transverse sizes using two likelihood methods. The first one considered the absorption systems as spheres or disks with a uniform distribution of gas. The second likelihood method considered the individual equivalent widths and assumed that equivalent widths varies with impact parameter: $W_r(r)$. I tested a power law and logarithmic function for $W_r(r)$. I obtained following results:

- Strong systems show a decrease in ΔW_r with increasing equivalent width, except for anticoincidences. They have transverse separation over 35 h_{70}^{-1} kpc. No anticoincidences are found for large W_r and transverse separation less than ~ 10 h_{70}^{-1} kpc. This is in agreement with a smooth distribution of gas or covering factor near unity inside these radii. There is a trend of increasing ΔW_r with transverse separation. Also, most of the anticoincidences are found at distances greater than ~ 10 h_{70}^{-1} kpc.
- Weak systems show a large ΔW_r dispersion as a function of W_r, with a trend of decreasing ΔW_r at $W_r > 0.2$ Å. These systems also have a trend of increasing ΔW_r with increasing transverse separation up to $\sim 3 - 4$ h_{70}^{-1} kpc. After this limit, the trend reverses. This could be indicating that smooth gas is distributed in radii that are less than $\sim 3 - 4$ h_{70}^{-1} kpc. Beyond this scales, the gas distribution becomes

more patchy. Also, anticoincidences are found homogeneously distributed between $\sim 0.2 - 20$ kpc, which is another proof that the weak MgII gas is more patchy than strong systems.

- I obtained for the full, weak and strong samples R$\sim$12, 10, 14 h_{70}^{-1} kpc using a standard Likelihood method.

  The inferred size in the case of weak systems is greater than previous results using the same technique (2 h_{70}^{-1} kpc; Ellison et al. (2004)). This can be explained because in that work the transverse distances probed were smaller, only between 0.3 and 2.7 h_{70}^{-1} kpc. However, I showed that the size of weak systems increases if larger separations of coincidences are considered. Given the results of smaller sizes and patchy gas for this population, it might be possible that increasing the range of transverse distances would lead to larger sizes due to the LOS crosses different weak systems, and not because weak systems be larger.

  For the strong population the sizes obtained from the subsamples are similar. Therefore, I would said that in this case the sizes converged to a reliable size. However, this must be taken with caution since the method does not take into account the upper limits at which an anticoincidence is declared. This has implications because the method assumes that if a pair is an anticoincidence, then one LOS did not cross the absorber. However upper limits can vary along a spectrum and also between different spectra.

- I found R$\sim$20[15-25] and $\sim$40[20-60] h_{70}^{-1} kpc for the weak and strong population respectively using the Likelihood method that takes into account equivalent widths, and assuming a logarithmic function for the equivalent width as a function of impact parameter. Considering a power law instead of a logarithmic function for the weak population I obtained R$\sim$250[200-300] h_{70}^{-1} kpc. This sizes correspond to $W_r = 0.001$ Å.

  The fractional equivalent width differences ΔW_r as a function of maximum equivalent width between is best modeled by the logarithmic function in the case of weak and strong systems.

  ΔW_r as a function of transverse distance is well matched by both $W_{log}(r)$ and $W_{pl}(r)$ for the weak population only up to $\sim 3 - 4$ h_{70}^{-1} kpc. This suggest that the size inferred from both likelihood analysis are overestimated. At least, the size at which a smoothed distribution of gas matches the data. On the other hand, for the strong sample there is a better match with the logarithmic assumed function at all transverse distances. Then, the model of a smoothed distribution of gas on scales of ~ 40 h_{70}^{-1} kpc is in agreement with the observations.

The most probable radius for strong systems and the range of values in which it can vary also agree with estimates of the size of MgII systems based on the number of absorber per unit redshift, which are in the range $46 - 70\ h_{70}^{-1}$ kpc (Tytler et al. 1987, Lanzetta et al. 1987).

None on the two Likelihood methods agree with previous size estimates of $\sim 46\ h_{70}^{-1}$ kpc for weak systems by Churchill et al. (1999). In that case, since dN/dz for weak systems is larger than for strong ones it follows that the cross section (σ) would be greater for weak than for strong systems. However, this thesis results indicate that weak systems are *smaller* and more patchy.

Finally, I studied the sample of systems associated with the lensing galaxies. In this cases the impact parameter to the galaxy can be obtained from the literature.

- The impact parameters probed by the lens sample is smaller than those from the Chen et al. (2010) sample. This is expected since both samples have different selection bias.
- Weak systems do not show a clear trend of decreasing W_r with impact parameter, which is in agreement with the picture of weak systems being less homogenous and smaller clouds surrounding galaxy halos.
- Strong systems do show a clear trend of decreasing W_r with impact parameter. Also, the data is consistent with the function $W_{log}(r)$ probed for strong systems in the likelihood analysis. The size inferred from that likelihood analysis is also in agreement with the data, since few point are at impact parameters greater than the range $40 - 60\ h_{70}^{-1}$ kpc.

Notes on the likelihood methods

Regarding the likelihood methods used in this thesis:

- The advantage of the standard likelihood method is that it is not necessary to assume a function Wr = Wr(r). However, in order to use it properly a homogeneous sample is needed in terms of signal to noise and resolution. If this condition is not met sizes can be under-estimated.
- I performed the test proposed by Martin et al. (2010) to detect if the method is more likely to be probing different absorbers in each LOS when the transverse separation is greater than certain limit.

7.1 Outlook

- The equivalent-width likelihood method can be improved by considering the triply and quadruply lensed quasars as three or four independent LOS crossing the same absorber, i.e, creating random triplet or quadruplet LOS rather than pairs.
- It would be valuable to repeat this analysis for resolved components in a system. Most of the weak systems in the Calan sample are single cloud systems. But strong systems are composed by typically one strong component and a few weaker ones. Then, a better constrain on the size of strong systems could be reached by using those strong components separately.
- A likelihood method similar to the one used here could be implemented to test the kinematics. The analog of the function W(r) would be a model of velocity differences between LOS considering outflows/inflows or gas rotating in a disk.

Bibliography

Blandford, R. D., & Narayan, R. 1992, *ARA&A*, 30, 311

Bond, N. A., Churchill, C. W., Charlton, J. C., & Vogt, S. S. 2001, *ApJ*, 562, 641

Bouché, N., Murphy, M., Péroux, C., Csabai, I., & Wild, V. 2007, in IAU Symposium, Vol. 235, IAU Symposium, ed. F. Combes & J. Palous, 392–393

Burud, I., et al. 1998, *ApJ*, 501, L5+

Chaffee, Jr., F. H., & Schroeder, D. J. 1976, *ARA&A*, 14, 23

Charlton, J. C., & Churchill, C. W. 1998, *ApJ*, 499, 181

Chen, H.-W., Helsby, J. E., Gauthier, J.-R., Shectman, S. A., Thompson, I. B., & Tinker, J. L. 2010, *ApJ*, 714, 1521

Churchill, C. W., Rigby, J. R., Charlton, J. C., & Vogt, S. S. 1999, *ApJS*, 120, 51

Churchill, C. W., & Vogt, S. S. 2001, *AJ*, 122, 679

Courbin, F., Lidman, C., Meylan, G., Kneib, J.-P., & Magain, P. 2000, *A&A*, 360, 853

Dekker, H., D'Odorico, S., Kaufer, A., Delabre, B., & Kotzlowski, H. 2000, in Society of Photo-Optical Instrumentation Engineers (SPIE) Conference Series, Vol. 4008, Society of Photo-Optical Instrumentation Engineers (SPIE) Conference Series, ed. M. Iye & A. F. Moorwood, 534–545

Dinshaw, N., Weymann, R. J., Impey, C. D., Foltz, C. B., Morris, S. L., & Ake, T. 1997, *ApJ*, 491, 45

Eigenbrod, A., Courbin, F., & Meylan, G. 2007, *A&A*, 465, 51

Eigenbrod, A., Courbin, F., Meylan, G., Vuissoz, C., & Magain, P. 2006, *A&A*, 451, 759

Ellison, S. L., Ibata, R., Pettini, M., Lewis, G. F., Aracil, B., Petitjean, P., & Srianand, R. 2004, *A&A*, 414, 79

Gregg, M. D., Wisotzki, L., Becker, R. H., Maza, J., Schechter, P. L., White, R. L., Brotherton, M. S., & Winn, J. N. 2000, *AJ*, 119, 2535

Hogg, D. W. 1999, ArXiv Astrophysics e-prints

Inada, N., et al. 2006, *AJ*, 131, 1934

Kacprzak, G. G., Churchill, C. W., Evans, J. L., Murphy, M. T., & Steidel, C. C. 2011, ArXiv e-prints

Kneib, J.-P., Cohen, J. G., & Hjorth, J. 2000, *ApJ*, 544, L35

Kochanek, C. S., Falco, E. E., Impey, C. D., Lehár, J., McLeod, B. A., & Rix, H.-W. 1999, in American Institute of Physics Conference Series, Vol. 470, After the Dark Ages: When Galaxies were Young (the Universe at 2 Z 5), ed. S. Holt & E. Smith, 163–175

Kochanek, C. S., et al. 2000, *ApJ*, 543, 131

Lanzetta, K. M., Turnshek, D. A., & Wolfe, A. M. 1987, *ApJ*, 322, 739

Lehár, J., et al. 2000, *ApJ*, 536, 584

Lidman, C., Courbin, F., Kneib, J.-P., Golse, G., Castander, F., & Soucail, G. 2000, *A&A*, 364, L62

Lopez, S., Ellison, S., D'Odorico, S., & Kim, T.-S. 2007, *A&A*, 469, 61

Lopez, S., Hagen, H.-J., & Reimers, D. 2000, *A&A*, 357, 37

Lopez, S., Reimers, D., Gregg, M. D., Wisotzki, L., Wucknitz, O., & Guzman, A. 2005, *ApJ*, 626, 767

Lopez, S., Reimers, D., Rauch, M., Sargent, W. L. W., & Smette, A. 1999, *ApJ*, 513, 598

Marshall, J. L., et al. 2008, in Society of Photo-Optical Instrumentation Engineers (SPIE) Conference Series, Vol. 7014, Society of Photo-Optical Instrumentation Engineers (SPIE) Conference Series

Martin, C. L., Scannapieco, E., Ellison, S. L., Hennawi, J. F., Djorgovski, S. G., & Fournier, A. P. 2010, *ApJ*, 721, 174

McGill, C. 1990, *MNRAS*, 242, 544

Momcheva, I., Williams, K., Keeton, C., & Zabludoff, A. 2006, *ApJ*, 641, 169

Narayanan, A., Charlton, J. C., Misawa, T., Green, R. E., & Kim, T.-S. 2008, *ApJ*, 689, 782

Narayanan, A., Misawa, T., Charlton, J. C., & Kim, T.-S. 2007, *ApJ*, 660, 1093

Nestor, D. B., Johnson, B. D., Wild, V., Ménard, B., Turnshek, D. A., Rao, S., & Pettini, M. 2011, *MNRAS*, 412, 1559

Nestor, D. B., Turnshek, D. A., & Rao, S. M. 2005, *ApJ*, 628, 637

Ofek, E. O., Maoz, D., Rix, H.-W., Kochanek, C. S., & Falco, E. E. 2006, *ApJ*, 641, 70

Oguri, M., et al. 2004, *PASJ*, 56, 399

Rao, S. M., & Turnshek, D. A. 1998, *ApJ*, 500, L115+

Rauch, M., Sargent, W. L. W., Barlow, T. A., & Simcoe, R. A. 2002, *ApJ*, 576, 45

Rigby, J. R., Charlton, J. C., & steChurchill, C. W. 2002, *ApJ*, 565, 743

Rogerson, J. 2011, Master's thesis, York University (Canada

Smette, A., Robertson, J. G., Shaver, P. A., Reimers, D., Wisotzki, L., & Koehler, T. 1995, *A&AS*, 113, 199

Smette, A., Surdej, J., Shaver, P. A., Foltz, C. B., Chaffee, F. H., Weymann, R. J., Williams, R. E., & Magain, P. 1992, *ApJ*, 389, 39

Songaila, A., & Cowie, L. L. 1996, *AJ*, 112, 335

Steidel, C. C. 1995, in QSO Absorption Lines, ed. G. Meylan, 139–+

Steidel, C. C., & Sargent, W. L. W. 1992, *ApJS*, 80, 1

Storrie-Lombardi, L. J., & Wolfe, A. M. 2000, *ApJ*, 543, 552

Tytler, D., Boksenberg, A., Sargent, W. L. W., Young, P., & Kunth, D. 1987, *ApJS*, 64, 667

Wambsganss, J. 2001, Progress in Astronomy, 19, 10

Williams, K. A., Momcheva, I., Keeton, C. R., Zabludoff, A. I., & Lehár, J. 2006, *ApJ*, 646, 85